NASA Technical Paper 3592

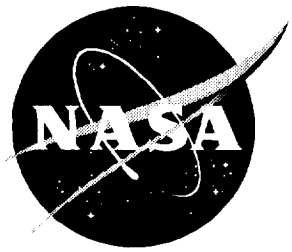

Comparison of Turbulence Models for Nozzle-Afterbody Flows With Propulsive Jets

William B. Compton III

September 1996

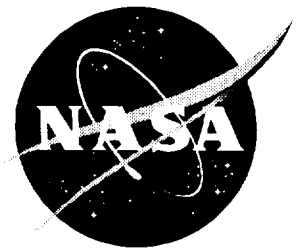

NASA Technical Paper 3592

Comparison of Turbulence Models for Nozzle-Afterbody Flows With Propulsive Jets

William B. Compton III
Langley Research Center • Hampton, Virginia

National Aeronautics and Space Administration
Langley Research Center • Hampton, Virginia 23681-0001

September 1996

Available electronically at the following URL address: http://techreports.larc.nasa.gov/ltrs/ltrs.html

Printed copies available from the following:

NASA Center for AeroSpace Information
800 Elkridge Landing Road
Linthicum Heights, MD 21090-2934
(301) 621-0390

National Technical Information Service (NTIS)
5285 Port Royal Road
Springfield, VA 22161-2171
(703) 487-4650

Abstract

A numerical investigation was conducted to assess the accuracy of two turbulence models when computing nonaxisymmetric nozzle-afterbody flows with propulsive jets. Navier-Stokes solutions were obtained for a convergent-divergent nonaxisymmetric nozzle-afterbody and its associated jet exhaust plume at free-stream Mach numbers of 0.600 and 0.938 at an angle of attack of 0°. The Reynolds number based on model length was approximately 20×10^6. Turbulent dissipation was modeled by the algebraic Baldwin-Lomax turbulence model with the Degani-Schiff modification and by the standard Jones-Launder k-ε turbulence model. At flow conditions without strong shocks and with little or no separation, both turbulence models predicted the pressures on the surfaces of the nozzle very well. When strong shocks and massive separation existed, both turbulence models were unable to predict the flow accurately. Mixing of the jet exhaust plume and the external flow was underpredicted. The differences in drag coefficients for the two turbulence models illustrate that substantial development is still required for computing very complex flows before nozzle performance can be predicted accurately for all external flow conditions.

Introduction

To obtain superior performance from both commercial and military aircraft, the propulsion system must be properly integrated with the airframe. Even if proper integration results in little interference between the two systems at subsonic speeds, the afterbody drag of a typical fighter airplane at high transonic speeds can still be as much as half of the total drag of the airplane. (See ref. 1.) Consequently, a great deal of effort has been expended in developing and using computational methods to predict nozzle-afterbody flows with propulsive jets. (See refs. 1–9.) Although some methods used panel techniques for this purpose, Navier-Stokes techniques are needed for adequate models of the physics of the highly complex viscous flow.

References 2–4 reported some of the earlier work in applying Navier-Stokes equations to the problem of nozzle-afterbody integration. References 6 and 7 extended the application by solving the three-dimensional, Navier-Stokes equations for transonic flow over a nonaxisymmetric nozzle typical of those advocated for advanced supersonic transports and fighters. References 8 and 9 further extended the application by solving for the complete problem by simultaneously including the external flow, the internal flow, and the jet exhaust plume and by investigating the flow prediction performance of several algebraic turbulence models.

The latter solutions generally agreed well with experimental data for attached flow. However, references 8 and 9 indicated some problem areas. When massive separation existed, the algebraic turbulence models failed to predict the separation point accurately. These turbulence models also gave pressure levels in the separated region that were much too high. In addition, some of the algebraic models yielded solutions that failed to converge to a steady state at transonic Mach numbers.

In 1992, the AGARD Working Group No. 17, Aerodynamics of Three-Dimensional Aircraft Afterbodies, formulated a plan to evaluate, compare, and validate existing computational methods for predicting nozzle-afterbody flows with propulsive jets. (See ref. 10.) The group selected several sets of benchmark experimental data for industry and government agencies participating in the AGARD working group.

Two of these test sets (at free-stream Mach numbers of 0.600 and 0.938) used the three-dimensional, nozzle-afterbody configuration that was investigated in references 6–9. This configuration consisted of an isolated (i.e., no wing or tails) superelliptic body with a nonaxisymmetric nozzle and a flowing jet. The nonaxisymmetric nozzle, which is convergent-divergent, was originally designed as a subsonic cruise setting of a variable-flap ejector nozzle for a supersonic transport. The geometry is deceptively simple. However, it yields nozzle flows that range from relatively simple attached flows at low subsonic Mach numbers to complex massively separated flows that challenge the predictive capabilities of state-of-the-art computational methods at transonic Mach numbers. The configuration is designed for subsonic speeds and, thus, is aerodynamically inefficient at transonic speeds, but it is excellent for assessing and validating computer codes and turbulence models over a wide range of flow conditions.

This investigation is based on NASA Langley's contribution to the two AGARD data sets. The paper also includes additional work. The investigation extend the work reported in references 2–9 by modeling the viscous dissipation with a two-equation turbulence model in all

regions aft of the model nose including the jet exhaust plume. This paper presents off-body results in the model boundary layer and in the jet plume. It compares the performance of the standard Jones-Launder k-ε turbulence model (i.e., the model in ref. 11 as modified in ref. 12) with the performance of the Baldwin-Lomax algebraic turbulence model (ref. 13) enhanced with the Degani-Schiff modification for strong vortical flow (ref. 14). The computations were done with the multiblock version of the PAB3D computer code (refs. 12 and 15), which solves the three-dimensional, thin-layer, Reynolds-averaged, Navier-Stokes equations and features a numerical algorithm based on upwind differencing.

The standard Jones-Launder k-ε turbulence model was chosen for the study because it had been implemented in PAB3D to provide a framework for more advanced turbulence models such as a nonlinear algebraic stress model or a full Reynolds stress model. At the time of the calculations, it was the most advanced turbulence model in PAB3D that would give a stable solution. The Baldwin-Lomax algebraic turbulence model was chosen as a baseline because it is very well known and established. An advantage of the standard Jones-Launder model is that its near-wall-damping function depends only on the flow parameters k, ε, and μ, and not on the configuration or grid (e.g., on the law-of-the-wall coordinate n^+). Because it is an eddy viscosity model and, thus, has an isotropic relationship between stress and strain, its disadvantage is that it cannot accommodate anisotropic normal stresses generated by massively separated and secondary flows. No effort was made to tune the Jones-Launder k-ε model to make it agree better with experimental data (such as was done in ref. 16 to increase mixing between the jet plume and surrounding atmosphere) because the objective of the paper was to evaluate the performance of the turbulence models without adjustment to any set of data.

This computational investigation was conducted at free-stream Mach numbers of 0.600 and 0.938 at an angle of attack of 0°. The Reynolds number based on the model length of 63.04 in. was nominally 20×10^6. The calculations are compared with experimental data.

Symbols

Unless otherwise noted, all variables are nondimensionalized by appropriate combinations of the free-stream parameters and the reference length L.

A^+, C_{cp}, C_{wk}	constants in the Baldwin-Lomax turbulence model
a,b	semimajor and semiminor axes of superellipse defining the cross section of model (eq. (B2))
C_f	skin-friction coefficient, $\frac{\tau_w}{q_\infty}$
C_p	pressure coefficient, $\frac{(p - p_\infty)}{q_\infty}$
C_μ	turbulence viscosity coefficient for k-ε model, $C_\mu = 0.09$
C_1, C_2	coefficients (eqs. (3) and (9))
c	local speed of sound
e	total energy per unit volume
$\mathbf{F}, \mathbf{G}, \mathbf{H}, \mathbf{F}_v, \mathbf{G}_v, \mathbf{H}_v$	Navier-Stokes flux vectors in Cartesian coordinate x, y, and z directions (eq. (A3))
$\hat{\mathbf{F}}, \hat{\mathbf{G}}, \hat{\mathbf{H}}, \hat{\mathbf{G}}_v, \hat{\mathbf{H}}_v$	Navier-Stokes flux vectors in transformed coordinate ξ, η, and ζ directions (eq. (A2))
$\mathbf{F}, \mathbf{G}, \mathbf{H}, \mathbf{F}_v, \mathbf{G}_v, \mathbf{H}_v$	turbulence flux vectors in Cartesian coordinate x, y, and z directions (eq. (3))
$\hat{\mathbf{F}}, \hat{\mathbf{G}}, \hat{\mathbf{H}}, \hat{\mathbf{G}}_v, \hat{\mathbf{H}}_v$	turbulence flux vectors in transformed coordinate ξ, η, and ζ directions (eq. (2))
F_{Kleb}	Klebanoff intermittency factor (eq. (19))
F_{max}	maximum value of $F(n)$
$F(n)$	function in Baldwin-Lomax turbulence model (eq. (18))
F_{wake}	function in Baldwin-Lomax turbulence model (eq. (17))
f_μ	Launder-Sharma damping function for k-ε turbulence models (eq. (11))
$H(x)$	Heaviside step function
J	Jacobian of transformation, $J = \frac{\partial(\xi, \eta, \zeta)}{\partial(x, y, z)}$
K	Clauser constant
k	turbulent kinetic energy
L	= 63.04 in., length of model from nose to jet exit; reference length
L_k	near-wall term for k equation
L_ε	near-wall term for ε equation
l	mixing length for turbulence viscosity
MS	model station, in.
M_t	local turbulent Mach number $\frac{\sqrt{k}}{c}$

$M_{t,0}$ = 0.25, cutoff turbulent Mach number

M_∞ free-stream Mach number

NPR nozzle pressure ratio, $\frac{p_{t,j}}{p_\infty}$

n normal distance from wall

n^+ law-of-the-wall coordinate, $\frac{n\sqrt{\rho\tau_w}}{\mu}$

$\bar{P}$ production term for k-ε equations

Pr Prandtl number

p pressure

p_{pitot} pitot pressure

p_s^+ nondimensional pressure gradient, $\frac{\mu_w}{\rho_w^2 u_*^3}\frac{\partial p}{\partial s}$

$p_{t,j}$ jet total pressure

$p_{t,\infty}$ free-stream total pressure

p_∞ free-stream static pressure

$\mathbf{Q}$ vector of dependent flow variables for two Navier-Stokes equations in Cartesian coordinate system (x, y, z) (eq. (A3))

$\hat{\mathbf{Q}}$ vector of dependent flow variables for Navier-Stokes equations in transformed coordinate system (ξ, η, ζ) (eq. (A2))

$\mathbf{Q}$ vector of k-ε dependent flow variables in Cartesian coordinate system (x, y, z) (eq. (3))

$\hat{\mathbf{Q}}$ vector of k-ε dependent flow variables in Cartesian coordinate system (ξ, η, ζ) (eq. (2))

q heat flux

q_∞ free-stream dynamic pressure, $\frac{\rho_\infty(u_\infty^2 + v_\infty^2 + w_\infty^2)}{2}$

R Reynolds number based on length of model from nose to nozzle exit

r radial distance from model axis

r' radial dimension of superellipse defining cross section of model

$\mathbf{S}$ source term for k-ε equations

S_k, S_ε source terms for equation

s distance along ξ coordinate, $ds = \sqrt{dx^2 + dy^2 + dz^2}$

TS tunnel station, ft

u, v, w velocities in physical coordinate x, y, and z directions, respectively

u_* friction velocity, $\sqrt{\frac{\tau_w}{\rho}}$

$\bar{u}$ local velocity, $\sqrt{u^2 + v^2 + w^2}$

u^+ law-of-the-wall velocity, $\frac{\bar{u}}{u_*}$

x, y, z physical (Cartesian) coordinates in axial, horizontal, and vertical directions, respectively (origin at nose of model)

y_0, z_0 offset dimensions for superelliptical corner of nozzle (eq. (B5))

β exponent of superellipse defining model cross section

Γ compressibility correction in k-ε turbulence model (eq. (10))

γ ratio of specific heats

ε dissipation rate of turbulent kinetic energy

μ viscosity

ξ, η, ζ generalized coordinates in transformed coordinate system (approximate axial, circumferential, and radial directions, respectively)

ρ density

τ viscous stress

τ_w local shear stress at wall

ϕ circumferential angle measured around model axis, deg (0° coincides with positive Z-axis in fig. 1(a))

ω vorticity

Superscripts:

$\hat{}$ denotes quantities in transformed coordinate system (ξ, η, ζ)

L laminar

T turbulent

Subscripts:		max	maximum
cross	indicates inner-outer transition point in Baldwin-Lomax turbulence model	o	outer
		t	turbulent; time (eqs. (1) and (A1))
		v	viscous
i	inner	w	wall
i, j, k	x, y, z components	∞	free-stream conditions

Theoretical Formulation

Governing Equations

The Navier-Stokes equations mathematically model the physical laws governing the motion of a compressible fluid with viscous dissipation. In PAB3D, the three-dimensional, time-dependent, Reynolds-averaged, Navier-Stokes equations are written in strong conservation form for a Cartesian coordinate system (x, y, z). Body forces are assumed to play an insignificant role in the afterbody flow problem and are neglected. The resulting time-dependent equations for conservation of mass, linear momentum, and energy are then expressed in terms of a fixed generalized coordinate system (ξ, η, ζ). The relations between the energy, pressure, and enthalpy for an ideal gas complete the system of equations. Because the dominant dissipative effects for most aerodynamic problems arise mainly from diffusion normal to the main flow direction, only those diffusion terms normal to the generalized coordinate most nearly aligned with the free stream are retained. For completeness, the Navier-Stokes equations, as they were implemented for this investigation, are given in appendix A.

Turbulence Models

In the implementation of the Navier-Stokes equations for this paper, the viscous stresses are assumed to be composed of a laminar component and a turbulent component (i.e., $\tau_{ij} = \tau_{ij}^{L} + \tau_{ij}^{T}$).The turbulent viscous dissipation, τ_{ij}^{T}, is modeled by several formulations in the PAB3D computer code. The solutions in this paper were obtained with the standard Jones-Launder k-ε turbulence model (ref. 11) as modified by Abdol-Hamid, Lakshmanan, and Carlson (ref. 12). The modifications extended the turbulence model to its full three-dimensional form and included generalized coordinates and a conservative form similar to the governing equations. For comparison, calculations were also made with the Baldwin-Lomax model (ref. 13) with the Degani-Schiff modification for strong vortical flow (ref. 14).

Jones-Launder k-ε Turbulence Model

The Jones and Launder (ref. 11) formulation for the two-equation turbulence model uses the turbulent kinetic energy k and the dissipation rate ε as the principal dependent variables. A modified form (ref. 12) of the original Jones-Launder model is used in this study. This modified formulation is fully three-dimensional, and the equations that govern the turbulent viscosity are written in a conservative form in terms of generalized coordinates as

$$\hat{\mathbf{Q}}_t + \hat{\mathbf{F}}_\xi + (\hat{\mathbf{G}} - \hat{\mathbf{G}}_v)_\eta + (\hat{\mathbf{H}} - \hat{\mathbf{H}}_v)_\zeta = \mathbf{S} \tag{1}$$

where

$$\left.\begin{aligned} \hat{\mathbf{Q}} &= \frac{\mathbf{Q}}{J} \qquad \mathbf{S} = \begin{Bmatrix} S_\varepsilon \\ S_k \end{Bmatrix} \qquad \hat{\mathbf{F}} = \frac{1}{J}(\xi_x\mathbf{F} + \xi_y\mathbf{G} + \xi_z\mathbf{H}) \\ \hat{\mathbf{G}} &= \frac{1}{J}(\eta_x\mathbf{F} + \eta_y\mathbf{G} + \eta_z\mathbf{H}) \qquad \hat{\mathbf{H}} = \frac{1}{J}(\zeta_x\mathbf{F} + \zeta_y\mathbf{G} + \zeta_z\mathbf{H}) \\ \hat{\mathbf{G}}_v &= \frac{1}{J}(\eta_x\mathbf{F}_v + \eta_y\mathbf{G}_v + \eta_z\mathbf{H}_v) \qquad \hat{\mathbf{H}}_v = \frac{1}{J}(\zeta_x\mathbf{F}_v + \zeta_y\mathbf{G}_v + \zeta_z\mathbf{H}_v) \end{aligned}\right\} \tag{2}$$

and J is the Jacobian of the transformation $J = \partial(\xi, \eta, \zeta)/\partial(x, y, z)$ from the physical coordinates (x, y, z) to the transformed coordinates (ξ, η, ζ).

The vectors in the physical coordinate system are defined as

$$\left.\begin{aligned} \mathbf{Q} &= \begin{Bmatrix} \rho\varepsilon \\ \rho k \end{Bmatrix} \\ \mathbf{F} = \begin{Bmatrix} \rho u\varepsilon \\ \rho uk \end{Bmatrix} \qquad \mathbf{G} &= \begin{Bmatrix} \rho v\varepsilon \\ \rho vk \end{Bmatrix} \qquad \mathbf{H} = \begin{Bmatrix} \rho w\varepsilon \\ \rho wk \end{Bmatrix} \\ \mathbf{F}_v = \begin{Bmatrix} \mu_\varepsilon \dfrac{\partial\varepsilon}{\partial x} \\ \mu_k \dfrac{\partial k}{\partial x} \end{Bmatrix} \qquad \mathbf{G}_v &= \begin{Bmatrix} \mu_\varepsilon \dfrac{\partial\varepsilon}{\partial y} \\ \mu_k \dfrac{\partial k}{\partial y} \end{Bmatrix} \qquad \mathbf{H}_v = \begin{Bmatrix} \mu_\varepsilon \dfrac{\partial\varepsilon}{\partial z} \\ \mu_k \dfrac{\partial k}{\partial z} \end{Bmatrix} \\ S_\varepsilon = C_1 \bar{P}\frac{\varepsilon}{k} - C_2\rho\frac{\varepsilon^2}{k} + L_\varepsilon \qquad S_k &= \bar{P} - \rho(1+\Gamma)\varepsilon + L_k \end{aligned}\right\} \tag{3}$$

where

$$\begin{aligned} L_\varepsilon = \frac{2\mu^L\mu^L}{\rho}\Bigg\{ &\left(\frac{\partial^2 u}{\partial x^2}\right)^2 + \left(\frac{\partial^2 u}{\partial y^2}\right)^2 + \left(\frac{\partial^2 u}{\partial z^2}\right)^2 + \left(\frac{\partial^2 v}{\partial x^2}\right)^2 + \left(\frac{\partial^2 v}{\partial y^2}\right)^2 + \left(\frac{\partial^2 v}{\partial z^2}\right)^2 \\ &+ \left(\frac{\partial^2 w}{\partial x^2}\right)^2 + \left(\frac{\partial^2 w}{\partial y^2}\right)^2 + \left(\frac{\partial^2 w}{\partial z^2}\right)^2 + 2\Bigg[\left(\frac{\partial^2 u}{\partial x\partial y}\right)^2 + \left(\frac{\partial^2 u}{\partial x\partial y}\right)^2 + \left(\frac{\partial^2 u}{\partial x\partial y}\right)^2 \\ &+ \left(\frac{\partial^2 v}{\partial x\partial y}\right)^2 + \left(\frac{\partial^2 v}{\partial x\partial z}\right)^2 + \left(\frac{\partial^2 v}{\partial y\partial z}\right)^2 + \left(\frac{\partial^2 w}{\partial x\partial y}\right)^2 + \left(\frac{\partial^2 w}{\partial x\partial z}\right)^2 + \left(\frac{\partial^2 w}{\partial y\partial z}\right)^2\Bigg]\Bigg\} \end{aligned} \tag{4}$$

$$L_k = 2\mu^L\left[\left(\frac{\partial\sqrt{k}}{\partial x}\right)^2 + \left(\frac{\partial\sqrt{k}}{\partial y}\right)^2 + \left(\frac{\partial\sqrt{k}}{\partial z}\right)^2\right] \tag{5}$$

and L_ε and L_k are corrections used by Jones and Launder to account for low Reynolds number flow near solid surfaces (i.e., their near-wall model in ref. 11). In S_ε and S_k, $\bar{P}$ is the full three-dimensional production term defined as

$$\bar{P} = \tau_{xx}^T\frac{\partial u}{\partial x} + \tau_{yy}^T\frac{\partial v}{\partial y} + \tau_{zz}^T\frac{\partial w}{\partial z} + \tau_{xy}^T\left(\frac{\partial u}{\partial y} + \frac{\partial v}{\partial x}\right) + \tau_{yz}^T\left(\frac{\partial v}{\partial z} + \frac{\partial w}{\partial y}\right) + \tau_{xz}^T\left(\frac{\partial u}{\partial z} + \frac{\partial w}{\partial x}\right)$$

or, because

$$\tau_{ij}^T = \mu^T\left[\left(\frac{\partial u_i}{\partial x_j} + \frac{\partial u_j}{\partial x_i}\right) - \frac{2}{3}\frac{\partial u_k}{\partial x_k}\delta_{ij}\right] - \frac{2}{3}\rho k\delta_{ij} \tag{6}$$

(where i, j, and k represent the x, y, and z components, respectively), $\bar{P}$ can be expanded to

$$\bar{P} = \mu^T\left\{\left(\frac{\partial u}{\partial y}+\frac{\partial v}{\partial x}\right)^2+\left(\frac{\partial v}{\partial z}+\frac{\partial w}{\partial y}\right)^2+\left(\frac{\partial w}{\partial x}+\frac{\partial u}{\partial z}\right)^2+2\left[\left(\frac{\partial u}{\partial x}\right)^2+\left(\frac{\partial v}{\partial y}\right)^2+\left(\frac{\partial w}{\partial z}\right)^2\right]\right.$$
$$\left.-\frac{2}{3}\left(\frac{\partial u}{\partial x}+\frac{\partial v}{\partial y}+\frac{\partial w}{\partial z}\right)^2\right\}-\frac{2}{3}\rho k\left(\frac{\partial u}{\partial x}+\frac{\partial v}{\partial y}+\frac{\partial w}{\partial z}\right) \tag{7}$$

where

$$\mu^T = C_\mu \rho\frac{k^2}{\varepsilon} \qquad \mu_\varepsilon = \mu^L+\frac{\mu^T}{\sigma_\varepsilon} \qquad \mu_k = \mu^L+\frac{\mu^T}{\sigma_k} \qquad C_\mu = 0.09 f_\mu \tag{8}$$

$$C_1 = 1.44 \qquad C_2 = 1.92[1-0.3\exp(-R_t^2)] \qquad \sigma_\varepsilon = 1.3 \qquad \sigma_k = 1.0 \qquad R_t = \frac{\rho k^2}{\mu_l \varepsilon} \tag{9}$$

Note that the source term **S** in equation (1) has not been written in terms of generalized coordinates because it is treated explicitly and because the generalized notations become very complex. However, the transformation is accounted for during computer coding of the equations. For an arbitrary function such as g,

$$\frac{\partial g}{\partial x_i} = \frac{\partial g}{\partial \xi_j}\frac{\partial \xi_j}{\partial x_i} \qquad \xi_x = J(y_\eta z_\zeta - y_\zeta z_\eta)$$

where i represents x, y, or z, and j represents ξ, η, and ζ. The compressibility correction Γ and the damping function f_μ are described next.

Compressibility correction for Jones-Launder k-ε model. The rate of spread of the shear layer in compressible flows is much lower than in incompressible flows. Several corrections for this effect have been developed in the last few years. Wilcox's model (ref. 17), which is one of the most widely used compressibility corrections and was used in this study, is

$$\Gamma = (M_t^2 - M_{t,0}^2)H(M_t - M_{t,0}) \tag{10}$$

where $H(x)$ is the Heaviside step function. Here, M_t is the local turbulent Mach number defined as $(\sqrt{k}/c)$, c is the local speed of sound, and $M_{t,0}$ is the cutoff turbulent Mach number specified in reference 17 as 0.25. Here, Γ is taken as zero for no compressibility correction. For this investigation, M_t was less than 0.2 in the region of the model. The value got as high as 0.53 in the shear layer between the jet exhaust plume and the external flow. Hence, the compressibility correction only took effect in the exhaust plume shear layer.

Damping function for Jones-Launder k-ε model. Wall-bounded flow solutions with the Jones-Launder k-ε turbulence model require damping or wall functions that adjust the turbulence viscosity near solid surfaces. The damping function f_μ adjusts the turbulent viscosity through the C_μ term. Far from the wall, $f_\mu = 1$, whereas at the wall, it is very small. The Launder-Sharma damping function (ref. 18) used by Jones and Launder in reference 11 was also used in this study. It has the form

$$f_\mu = \exp+\left[-\frac{3.41}{1+(R_t/50)}\right] \tag{11}$$

Baldwin-Lomax Turbulence Model

The Baldwin-Lomax turbulence (ref. 13) model is a two-layer algebraic model, which follows the pattern of Cebeci (ref. 19) but avoids the necessity of determining the boundary layer thickness. The turbulence viscosity is evaluated as follows:

$$\mu^T = (\mu^T)_i \qquad (n \le n_{cross})$$

$$\mu^T = (\mu^T)_o \qquad (n > n_{cross})$$

where n is the normal distance from the wall and n_{cross} is the smallest value of n at which magnitudes of $(\mu^T)_i$ and $(\mu^T)_o$ are equal. The turbulent stress is determined from

$$\tau_{ij}^T = \mu^T\left[\left(\frac{\partial u_i}{\partial x_j} + \frac{\partial u_j}{\partial x_i}\right) - \frac{2}{3}\frac{\partial u_k}{\partial x_k}\delta_{ij}\right] \tag{12}$$

For the inner layer

$$(\mu^T)_i = \rho l^2 |\omega| \tag{13}$$

where

$$l = 0.4n[1 - \exp(-n^+/A^+)] \tag{14}$$

and n^+ has the special definition

$$n^+ = n(\sqrt{\rho_w \tau_w}/\mu_w) \tag{15}$$

and

$$\omega = \sqrt{(u_y - v_x)^2 + (v_z - w_y)^2 + (w_x - u_z)^2} \tag{16}$$

For the outer layer

$$(\mu^T)_o = KC_{cp}\rho F_{wake} F_{Kleb}(n) \tag{17}$$

where F_{wake} is the smallest of $n_{max}F_{max}$ and $C_{wk}n_{max}(u^2 + v^2 + w^2)_{max}/F_{max}$.

The term n_{max} is the value of n corresponding to the maximum value of F (i.e., F_{max}), where

$$F(n) = n|\omega|[1 - \exp(-n^+/A^+)] \tag{18}$$

and F_{Kleb} is calculated by

$$F_{Kleb} = [1 + 5.5(nC_{Kleb}/n_{max})^6]^{-1} \tag{19}$$

The values of the constants appearing in equations (2)–(7) are listed in reference 13 as

$$A^+ = 26 \qquad C_{wk} = 0.25 \qquad C_{cp} = 1.6 \qquad C_{Kleb} = 0.3 \qquad K = 0.0168$$

Degani and Schiff (ref. 14) modified the Baldwin-Lomax turbulence model to determine more accurately the outer length scale when a strong vortical flow structure or a massive separation exists. For these flows at a given streamwise model station, they discovered that the quantity $F(n)$ (eq. (18)) has more than one local maximum or peak. Furthermore, the largest peak is always associated with the radial distance from the body to the edge of the backflow region, and its use can result in an outer eddy viscosity as much as two orders of magnitude too high.

Hence, Degani and Schiff recommend using the local maximum of $F(n)$ near the wall in the underlying backflow within the separated region. To avoid selecting extraneous fluctuations, they chose the first well-defined peak away from the wall; here, a well-defined peak in $F(n)$ is defined as a peak where $F(n)$ drops to less than 90 percent of its local maximum value. To avoid spurious oscillations very close to the wall, the first nine grid points off the wall were skipped during the search for the maximum value of $F(n)$.

Numerical Procedure

Computational Domain and Grid

Figure 1 illustrates the computational model and presents a photograph of the experimental model installed in the Langley 16-Foot Transonic Tunnel. The figure defines the nozzle-afterbody region that, along with the jet exhaust plume, is the primary region of interest in this investigation. The nozzle is nonaxisymmetric with a convergent-divergent internal geometry. A more detailed description of the configuration is given subsequently.

Figure 2 shows details of the computational domain, the grid, and the coordinate system. The domain and grid were cylindrical. (See fig. 2(a).) For maximum computation efficiency, symmetry was assumed about the vertical plane containing the model axis. Hence, the computational domain consisted of only half of the cylinder. The domain extended ≈20 model radii (1 model length) upstream from the model nose, ≈30 model radii downstream from the nozzle exit, and ≈30 model radii from the model surface to the far-field boundaries ($\zeta = \zeta_{max}$).

The grid was body fitted (i.e., grid lines coincided with the model surface and other boundaries) to facilitate implementation of the boundary conditions. The grid was composed of four blocks with point-to-point connectivity between the blocks. (See fig. 2.) The mesh density for each block is given in table I. Block 3(a) in table I was used in an attempt to improve the agreement between the computations and test data in the downstream part of the jet plume. Although its effect was negligible, the results presented at $M_\infty = 0.600$ were computed with block 3(a) substituted for block 3. For the grid spacing to vary smoothly at the block interfaces, the cell dimensions normal to the block interfaces were equal for opposing cells on each side of the interface.

Grid lines were clustered near the body surface, on the afterbody, near the nozzle exit, and at the nozzle throat. They were also clustered in the circumferential direction near the corners of the afterbody. Figure 2(a) shows details of the surface meshes in the vicinity of the nozzle-afterbody. The surface meshes illustrate the external and internal shape of the nozzle. Figure 2(c) shows details of the mesh in the vertical plane of symmetry at the nozzle. The small base at the nozzle exit is modeled with 29 grid points distributed along its height. The axial spacing of the grid at the nozzle exit was 20 percent of the base height. Grid cells next to the model surface had a dimension normal to the surface of 0.000300 in. on the external surface and 0.000225 in. on the internal nozzle surface. These dimensions gave values of n^+ for the first grid point off the wall of 1.5 or less for the exterior of the nozzle and 4.5 or less for the interior.

Numerical Algorithm

The solutions were obtained with the multiblock version of the Navier-Stokes computer code PAB3D. (See refs. 12 and 15.) The PAB3D solves the three-dimensional, time-dependent, Reynolds-averaged, Navier-Stokes equations written in strong conservation form for a Cartesian coordinate system (x, y, z). The computer code allows for laminar viscous dissipation in all three directions. Turbulent viscous dissipation can be modeled in only two directions.

The PAB3D solves the equations by the finite volume principle with the spatial derivatives in the equations evaluated as conservative flux balances across the grid cells. The fluxes at the cell interfaces are determined with Roe's upwind-biased, flux-difference splitting combined with the min-mod gradient-limiting procedure to ensure monotonicity across discontinuities such as shock waves. The scheme is spatially third-order accurate on a uniform grid but globally second-order accurate on a stretched grid.

The time-differencing algorithm used in the computational procedure is an approximately factored, alternating direction, implicit scheme in delta form. The approximate factorization is applied in the two cross-flow directions, while the terms in the axial, or main flow, direction are split and added to the two resulting factors.

Boundary Conditions

Navier-Stokes Equations

Because the free stream is subsonic, Riemann invariants for a one-dimensional flow were used to calculate the primitive flow variables ρ, u, v, w, and p at the computational domain inflow ($\xi = 1$) and far-field ($\zeta = \zeta_{max}$) boundaries. (See fig. 2(a).)

Reflection boundary conditions were imposed at the vertical plane of symmetry ($\eta = 1$) and ($\eta = \eta_{max}$) of the computational domain and on its centerline ($\zeta = 1$ ahead of the model and in the nozzle and plume). At the

outflow boundary ($\xi = \xi_{max}$), where the flow is a mixture of the jet exhaust and the free stream, all gradients were set to zero regardless of the free-stream conditions.

At the jet inflow boundary, which is subsonic, jet total pressure, jet total temperature, and flow angle were specified. Static pressure was extrapolated to the boundary from the interior of the computational domain. Finally, no-slip and adiabatic wall boundary conditions were imposed on the body surface.

Turbulence Equations

Boundary conditions for the Jones-Launder k-ε turbulence model consisted of the turbulent kinetic energy k and turbulent dissipation ε set equal to zero at the wall boundaries. At the symmetry and outflow boundaries, the gradients of these two terms were set equal to zero.

At the far-field boundary, a characteristic boundary condition for k and ε, which is similar to the Riemann-invariant boundary condition for the Navier-Stokes equations, was used. However, the turbulent characteristic condition contains only one eigenvector.

Transition from laminar to turbulent flow for the computations was fixed at the third grid plane downstream of the model nose in block 2 and the nozzle inflow station for the internal flow in block 4. In the experimental investigation, transition was fixed at 1 in. behind the nose of the model. Although not known for sure, the internal flow in the experimental model is thought to be turbulent. The boundary conditions for the turbulent quantities at this transition plane were obtained in the following manner. First, the vorticity was computed in the two preceding laminar planes, and the turbulent kinetic energy k was scaled to the shape of the vorticity profiles. The maximum value of k was set to 1 percent of the square of the maximum velocity in the plane. The turbulent dissipation was then computed from the relation $\varepsilon = f(k, \varepsilon, u, v, w)$.

Numerical Solution Strategy

Although Roe's flux-differencing scheme is used to compute the fluxes for the explicit side of the equations, van Leer's flux-splitting scheme is used for the implicit side. This procedure enhances the robustness of the computer code and maintains the desirable characteristic of Roe's scheme of accurately capturing discontinuities with one or two grid points.

The inflow grid block 1 was run as a laminar block with the viscous dissipation imposed in only the radial direction. Blocks 2–4 were run as turbulent blocks. Turbulent dissipation was modeled by the modified Jones-Launder k-ε and the Baldwin-Lomax turbulence models for block 2 external to the model and for block 4 internal to the nozzle. For these blocks, the thin-layer assumption, which only retains the viscous terms normal to the surface of the model (the η direction), was made. In the plume block 3, only the Jones-Launder k-ε turbulence model was utilized because the turbulent viscosity in the Jones-Launder k-ε model depends only on the flow and not on the distance from some surface as with the algebraic Baldwin-Lomax model. In this block, viscous terms were imposed only in the radial direction, and the computation included the calculation of the viscosity in both the radial and circumferential directions (i.e., the ζ and η directions). The two computations gave essentially the same results.

In these computations, a grid-sequencing strategy was followed to further enhance the convergence. The strategy, which has been used in many computer codes, consisted of starting the solution on a coarse mesh and then transferring the solution to successively finer meshes. To conserve computer resources with the Jones-Launder k-ε solutions, the turbulence should be developed fully on the coarser grid before switching to the next finer grid. The solutions were first run on the coarsest grids for almost 8000 time steps. This strategy was especially important at the free-stream Mach number of 0.600 because the turbulence developed more slowly than it did at the free-stream Mach number of 0.938.

To alleviate numerical stiffness, the Jones-Launder k-ε equations are implemented in PAB3D uncoupled from the Navier-Stokes equations and from each other. They are also solved with a much smaller Courant-Friedrichs-Lewy (CFL) number than the Navier-Stokes equations (approximately 0.25 percent of the CFL number of the Navier-Stokes equations). This strategy has not noticeably affected the convergence rate or the quality of the solutions. (See ref. 12.)

For the solution to converge quickly to a steady state while remaining stable, the CFL number was allowed to adjust from one iteration to the next. Usually, the CFL number quickly adjusted to a value of approximately nine. At each iteration, the CFL number was the same for each grid cell. The complete solution at $M_\infty = 0.938$ took a total of 37 hr on the Langley Cray Y-MP supercomputer.

Computer Resource Requirements

The computations for this study were run on the Langley Cray Y-MP supercomputer. On this machine, PAB3D required the following resources:

Mode	Words of memory, per grid point	Computational time, μsec/grid point/time step
Laminar	15	33
Baldwin-Lomax turbulence model	15	33
k-ε turbulence model	20	44

Experimental Apparatus and Data

The experimental databases for this report were obtained in the Langley 16-Foot Transonic Tunnel, which is a continuous atmospheric single-return wind tunnel with an octagonal slotted test section. Reference 20 gives a thorough description of the wind tunnel. Figure 1(b) is a photograph of the model mounted in the wind tunnel; figure 3 shows the general arrangement of the wind tunnel model and support system. The centerline of the model was aligned with the centerline of the wind tunnel. High-pressure air was used to simulate the jet exhaust. The model blockage was 0.14 percent of the cross-sectional area of the wind tunnel test section. The maximum combined blockage of the model and support system was 0.19 percent.

Experimental Model

The experimental model, which was 63.04 in. long, consisted of an isolated (i.e., no wing or tails) superelliptic body with a nonaxisymmetric convergent-divergent nozzle attached. The model had a conical nose that blended smoothly into a superelliptical cross section at fuselage station 26.50 in. The cross section at that station was nearly rectangular with rounded corners. The external geometry then remained constant to fuselage station 55.05 in. where the nozzle connected to the body.

The specific nozzle configuration considered in this investigation represented a transonic cruise dry-power setting of a variable-geometry nozzle. The nozzle is typical of those advocated for supersonic transports and advanced fighter airplanes. Geometric details of the nonaxisymmetric convergent-divergent nozzle are given in figure 4. Figure 5 depicts the pressure orifice locations on the external and internal surfaces of the nozzle.

Internally, the sidewalls of the nozzle are flat and parallel. The aspect ratio of the nozzle throat (i.e., the ratio of the width to height of the nozzle throat) was 2.380, and the aspect ratio of the nozzle exit was 1.9. The ratio of the exit area to throat area was 1.250. This ratio gives a design nozzle pressure ratio (the ratio of jet total pressure to free-stream static pressure) of 4.25 and a design exit Mach number of 1.6.

The external cross-sectional geometry varied from the superellipse at the nozzle connect station to essentially a rectangle with superelliptical corners at the nozzle exit. The flap boattail angle was 17.56°, and the sidewall boattail angle was 6.93°. The equation defining the external cross-sectional geometry of the nozzle is

$$\left(\frac{y - y_0}{a}\right)^{\beta} + \left(\frac{z - z_0}{b}\right)^{\beta} = 1.0 \qquad (20)$$

where y_0, z_0, a, b, and β are given in figure 4(b) as functions of x. A mathematical description of the complete model (external and internal geometries) is given in appendix B.

Experimental Data

The experimental data that were used in this investigation are part of a broad database for the nonaxisymmetric nozzle. Except for the plume surveys published in reference 21 and parts of the surface pressure data in references 6–9, most of the experimental data have not been reported. This paper contains some of the surface pressure data not previously published by NASA; however, the data were furnished to the AGARD working group mentioned in the introduction.

The data were taken with the jet exhaust simulated with high-pressure air at a total temperature nominally equal to 544°R. For comparison, the free-stream total temperature was approximately 581°R at $M_\infty = 0.600$ and 620°R at $M_\infty = 0.938$. The jet total pressure ratio (i.e., ratio of jet total pressure to free-stream static pressure) was 4.0, which is a value close to the design pressure ratio of 4.25. During the experiments to obtain the sample test data, boundary layer transition from laminar to turbulent flow was fixed at 1 in. from the nose of the model (at $x/L = 0.016$) with a 0.1-in-wide strip of No. 90 grit. The absolute error in the free-stream Mach number is no greater than ±0.004. (See ref. 20.) All pressures were measured with electronic pressure-scanning modules. The accuracies of the afterbody pressure coefficients are ±0.0171 and ±0.0097 at the free-stream Mach numbers of 0.600 and 0.938, respectively.

For completeness, the experimental data used in this paper are tabulated in tables II and III. Figure 5 provides the locations of the external and internal pressure orifices, which were approximately 0.040 in. in diameter. The radii and circumferential angles of the pitot rake locations given in table III (excerpted from ref. 21) are given in the model coordinate system. The locations in

this paper are identical to the ones given in reference 21; however, in reference 21, the radii and circumferential angles are given in the rake coordinate system whose center was offset from the model axis.

Results

This section presents a discussion of the computational performance of the standard Jones-Launder k-ε turbulence model and the Baldwin-Lomax algebraic turbulence model for the following classes of flows that were encountered during this investigation:

1. Subsonic flow with both favorable and adverse pressure gradients and little or no separation (This type of flow developed on the external surface of the afterbody at $M_\infty = 0.600$.)
2. Subsonic and supersonic attached flow with both strong favorable and adverse pressure gradients and a very thin boundary layer (This type of flow developed on the internal surface of the nozzle at NPR = 4.0.)
3. Transonic flow with both favorable and strong adverse pressure gradients and massive separation (This type of flow developed on the external surface of the afterbody at $M_\infty = 0.938$.)
4. Jet mixing between the exhaust plume and the external flow

The ability of the turbulence models to predict surface pressures, skin friction, boundary layer profiles, and total pressure profiles in the jet exhaust plume is examined for each of these classes of flows. In addition, details of the flow in the region of the nozzle throat are discussed as well as convergence properties of the solutions. Finally, the culmination of these details into afterbody drag is discussed for each turbulence model.

Numerical Convergence

Numerical convergence for this investigation was based on the residual and the computed pressures. The convergence history at $M_\infty = 0.938$ with the Jones-Launder k-ε turbulence model is presented in figure 6 and is typical for all test computations. As explained in the previous section on the numerical solution strategy, the solution was started on a coarse mesh and was transferred to successively finer meshes to enhance convergence. The spikes in the residual at approximately 3400, 7600, and 8400 iterations indicate when the solution was transferred to the next finer mesh. The solution has converged by four orders of magnitude in 10 000 iterations.

A brief grid study for this basic configuration has been reported for a baseline configuration composed of this experimental model with a sting (i.e., solid plume simulator) attached. (See refs. 6 and 7.) The grid for the baseline configuration consisted of a single block. This study investigated mesh densities of $64 \times 10 \times 32$, $129 \times 33 \times 65$, and $257 \times 65 \times 129$; the three numbers in each mesh pertain to the densities in the axial, circumferential, and radial (i, j, and k) directions, respectively. The results, which were obtained at free-stream Mach numbers of 0.8 and 1.2, indicated that the solutions were essentially grid converged for the $129 \times 33 \times 65$ mesh. That particular mesh contained 129 grid planes in the axial direction for the combined length of the model and sting plume simulator but only 29 axial grid planes in the nozzle-afterbody region.

The effect of mesh density was investigated further. The primary multiblock grid for this investigation contained $113 \times 53 \times 77$ planes in the external model block. (See fig. 2 and table I.) Of the 113 axial planes, 57 were in the nozzle-afterbody region, which resulted in a mesh density on the external surface of the nozzle of 57×53. (See fig. 2(b).) The internal nozzle block had a mesh density on the surface of 89×53. Numerical experiments were conducted with this grid and with one created by deletion of every other grid plane in the axial and circumferential directions.

When very little or no separation occurred, such as at $M_\infty = 0.600$, or when the viscous dissipation was modeled with the Jones-Launder k-ε turbulence model, very little difference was noted between the results for the two meshes other than slightly better resolution for the finer mesh. However, at $M_\infty = 0.938$, strong shocks and massive separation exist, and the two grids yielded different results with the Baldwin-Lomax turbulence model.

Figure 7 presents the results on the external surface of the nozzle in the vertical plane of symmetry at $M_\infty = 0.938$ for the Baldwin-Lomax turbulence model. The pressures presented in figure 7(a) show only slightly better resolution for the finer mesh (i.e., the external shock is defined slightly better, and the internal expansion-contraction pattern is defined better). However, the finer grid results in an underlying very thin secondary separation bubble within the primary separated region as shown by the velocity vectors near the surface in the separated region. (See figs. 7(b) and 7(c).) The flow direction in the secondary bubble is toward the nozzle exit counter to the direction of the primary separated flow. The secondary bubble velocity vector plots at two different iterations (fig. 7(b)) show that the solution has not converged to a truly steady state. The underlying secondary separated region was far less evident for the coarser mesh, possibly, as a result of the coarse-mesh solution having converged better. The fine-grid solution was run for approximately 30 000 iterations without converging to a steady state. Unconverged numerical solutions had been

obtained previously with some algebraic turbulence models. (See ref. 8.) Whether or not this solution would eventually converge to a steady state was never determined, but further investigation was not deemed prudent due to the extensive computer resources required.

The spacing of the grid cells normal to the surface of the model was 0.000300 in. for the external surface and 0.000225 in. for the internal surface. As figure 8 shows, these dimensions give values of n^+ for the first grid point off the wall of 1.5 or less for the exterior of the nozzle and 4.5 or less for the interior. For the Reynolds numbers of this investigation, placement of the first grid plane closer to the surface should not substantially improve the accuracy of the pressure. Skin friction, as a function of n^+ for the first grid point off the wall, was investigated for a flat plate in reference 12. These results suggest that the computed skin friction should be within ±1.5 percent of the grid-converged (for the normal coordinate) value for the external surface. They also indicate that, for the internal surface, the computed skin friction should be within ±5 percent for the Jones-Launder k-ε turbulence model and within ±10 percent for the Baldwin-Lomax turbulence model.

Free-Stream Mach Number of 0.600

The qualitative character of the overall flow field at $M_\infty = 0.600$ is given in figures 9–11. Figure 9 presents Mach number contours in the vertical and horizontal planes of symmetry for the Jones-Launder k-ε and Baldwin-Lomax turbulence models. Figure 10 presents the corresponding velocity vectors near the nozzle exit. Figure 11 presents the corresponding computed oil flows on the external and internal surfaces of the nozzle.

Both Mach number contours and velocity vectors indicate that the flow is well behaved (except for the distortion of the sonic line at the nozzle throat) at this free-stream Mach number. By themselves, they give little or no indication that the flow separates on either the external or internal surface of the nozzle. The contours also illustrate the initial thinning of the boundary layer as the flow accelerates around the shoulder of the external surface of the nozzle and its subsequent thickening as the flow decelerates on the aft part of the nozzle.

Although the Mach number contours and the velocity vectors do not suggest separation, the simulated oil flows shown in figure 11 indicate that both turbulence models predict that the flow separates along a line at the corners of the external surface of the nozzle. (See fig. 11(a).) For the Baldwin-Lomax model, the flow also separates on the top and bottom of the external surface near the exit. However, this separated region is extremely thin as indicated by the velocity vectors. The flow does not appear to separate on the internal surface for either turbulence model.

Figures 12–16 present quantitative details of the solution at $M_\infty = 0.600$. Figure 12 presents the computed and measured pressure coefficients on the external surface of the nozzle. A sketch in each of the figures indicates which row of pressures is plotted. The base pressure data are plotted at $x/L = 1.00$. A comparison of the computed pressures and data shows that both turbulence models predicted the pressures on the external surface of the nozzle very well. The only discrepancy between the computations and experimental data is at the base for the top row. (See fig. 12(a).) The computed base pressures for the other rows agree very well with the experimental data (i.e., the data points at $x/L = 1.0$). They agree particularly well for the side row (fig. 12(e)) where the sidewall boattail angle is smaller and the base is thicker than they are on the top flap. (See the sketch of the nozzle in fig. 4.)

The distribution of the ratio of the internal nozzle wall pressures to the jet total pressure is shown in figure 13 as a function of x/L. The geometric throat of the nozzle is at $x/L = 0.9077$. A strong favorable pressure gradient exists in the convergent section of the nozzle. Downstream of the throat, the pressure gradient oscillates between adverse and favorable.

Again, both turbulence models do an excellent job of predicting the pressures. The spikes in the pressures at $x/L \approx 0.89$ are a result of the sharp break in the internal nozzle contour at the point where the nozzle starts to contract. The solution is probably invalid at that point. The oscillations downstream of the throat reflect the pattern of compression and expansion waves of the flow inside the nozzle. As the boundary layer profiles show, the boundary layer is extremely thin inside the nozzle. Hence, the flow is dominated by inertial and compressible effects, and viscous effects are relatively unimportant in computing the pressures.

Figure 14 presents the computed skin-friction coefficients. No experimental data were available for skin friction. The Jones-Launder k-ε turbulence model predicts a value of the skin-friction coefficient approximately 20 percent higher than that of the Baldwin-Lomax model on the external surface of the nozzle-afterbody and downstream of the throat on the internal surface. Upstream of the throat, where the flow is subsonic and strongly accelerating and the boundary layer is very thin, both turbulence models give essentially the same results except for the spikes at $x/L \approx 0.89$ where the sharp break in the internal nozzle contour occurs. Because the turbulence level should be very low in this region of strongly accelerating flow, the choice of the turbulence model should have minimal effect.

Figure 15 shows computed universal law-of-the-wall boundary layer profiles for the flow over the constant cross section of the model leading up to the nozzle-afterbody. Unfortunately, no experimental boundary layer data were available for this investigation. The profiles are presented at axial model stations starting about midway along the constant cross section and ending at the nozzle connect station. By a technique similar to that employed in reference 23, the streamwise pressure gradients at the boundary layer stations are normalized by an appropriate combination of ρ_w, μ_w, and u_* to give a law-of-the-wall pressure gradient $p_s^+ = \frac{\mu_w}{\rho_w^2 u_*^3}\frac{\partial p}{\partial s}$. The pressure gradients are relatively mild at the forward stations and become increasingly more severe as the nozzle connect station is approached.

The profiles for both turbulence models agree well with theory in the inner part of the viscous sublayer. Although they both show a law-of-the-wall characteristic in the logarithmic region, the Jones-Launder k-ε turbulence model generally agrees with theory in this region better than the Baldwin-Lomax model does. This agreement with theory is consistent with references 23 and 24, which indicate that the universal logarithmic (law-of-the-wall) relationship holds for mild pressure gradients. The Jones-Launder k-ε turbulence model predicts that the slope in the outer portion of the logarithmic region decreases as the pressure gradient becomes more severe. The Baldwin-Lomax model also seems to predict this trend but not as clearly as the Jones-Launder k-ε turbulence model does. This decrease in slope also seems to be consistent with the pressure-drop data of reference 24.

Figure 16 shows velocity and pitot-pressure boundary layer profiles for the external and internal surfaces of the nozzle-afterbody. Profiles of the ratio of the pitot pressure to free-stream total pressure are presented to correspond with the data in the jet plume. The jet plume data are presented and discussed subsequently.

The external and internal boundary layer profiles are plotted to the same scale to show clearly the relative thickness of the two boundary layers. Inside the nozzle, the boundary layer is extremely thin. As a consequence, very little difference can be seen between the profiles for the two turbulence models. The external profiles for the Jones-Launder k-ε turbulence model have a flatter, more turbulent characteristic near the wall, which results in higher skin friction as indicated in figure 14. The external profiles illustrate that the boundary layer gets thicker as the flow decelerates in its approach to the nozzle exit. This effect is more evident for the top of the nozzle ($\phi = 0°$) than for the side ($\phi = 90°$) because the deceleration is much stronger on the top.

Details of Throat Region

Although the primary subject of this paper is the comparison of turbulence models, the flow phenomena in the throat region are essentially the same for both turbulence models, and the physics of the flow in the throat region is discussed briefly in this section. Figures 17–19 show details of the internal flow in the region of the nozzle throat. The Mach number contours in the vertical plane of symmetry (fig. 17) are nearly the same for both turbulence models.

The Mach number contours illustrate the distortion of the flow, including the sonic line, in the region of the throat. While the sonic line is upstream of the geometric throat on the upper and lower walls, it is downstream of the geometric throat on the centerline of the nozzle. (See fig. 17.) The Mach number contours also illustrate that, near the nozzle wall, the flow reaches sonic speed upstream of the geometric throat ($x/L = 0.9077$), continues to accelerates until it is into the divergent section of the nozzle, then decelerates ($x/L \approx 0.909$), and finally accelerates again ($x/L \approx 0.920$). This latter characteristic of the flow reflects the internal pressure distributions shown in figure 13 and is typical of nozzles with small throat radii, as was mentioned briefly in reference 8.

Here, the distortion of the flow at the throat appears to be the result of the inertial properties of the fluid and of wave propagation as it occurs in supersonic flow. The flow distortion does not appear to be caused by viscous effects because the boundary layer is extremely thin, and the flow is not separated. (See the details of the velocity vectors for the Jones-Launder k-ε turbulence model in fig. 18.) The details of the simulated particle traces (fig. 19) show that the minimum area of each successive stream tube progresses downstream as the centerline of the nozzle is approached from the wall. This result is consistent with the Mach number contours shown in figure 17. The result further supports the contention that the distortion is due to the inertial properties of the fluid because inertia would keep the flow from reacting instantaneously to the curvature of the wall or to the previous stream tube. In other words, as the centerline is approached from the wall, the turning of the flow in each successive stream tube would be slightly delayed and, hence, occur farther downstream. The particle traces also illustrate the contraction and expansion of the stream tubes as the flow negotiates the shocks and expansions inside the nozzle.

Free-Stream Mach Number of 0.938

Figures 20–22 show the overall qualitative characteristics of the flow field at $M_\infty = 0.938$. The Mach number contours (fig. 20) are basically the same for both turbulence models. They illustrate, even more

dramatically at this Mach number than they did at M_∞ = 0.600, the thinning of the boundary layer as the flow accelerates around the shoulder of the boattail on the external surface. The contours show that the external flow at this Mach number is very complex. The flow accelerates to supersonic speeds and develops strong shocks on the top, bottom, and sides of the nozzle. Massive separation exists on the top and bottom of the nozzle. Internally, the flow is essentially the same as it was at M_∞ = 0.600 because, at this nozzle pressure ratio, the internal flow is basically independent of the free-stream Mach number.

Figure 21 presents the velocity vectors in the vicinity of the nozzle exit. The figure shows that the separation bubble for the Jones-Launder k-ε turbulence model is almost as extensive in the wetted area as for the Baldwin-Lomax model but is approximately half as thick.

The computed oil flows (fig. 22) illustrate the complex recirculation patterns in the separated region. They also show that, although the separation is confined to the top and bottom of the nozzle for the Jones-Launder k-ε turbulence model, it extends partway down the sides of the nozzle for the Baldwin-Lomax turbulence model. The traces for the Baldwin-Lomax model illustrate the underlying secondary separation bubble within the main separation bubble. As discussed previously in the section on convergence, the secondary bubble tended to move downstream, which indicated that the Baldwin-Lomax solution at this Mach number was not fully converged. The solution was run for approximately 30 000 iterations, and further investigation of this particular aspect was not deemed prudent due to the extensive computer resources required. Numerical solutions, which continue to change, have been encountered previously with this and another computer code for this particular problem. (See refs. 8 and 9.)

Figures 23–27 present the quantitative details of the solutions at M_∞ = 0.938. They illustrate that neither turbulence model provided entirely satisfactory results for this separated flow condition. Figure 23 presents the pressure coefficient distributions for the external surface. The distributions show that, up to the separation point, little difference exists between the pressures for the two turbulence models and that the computations agree with the experimental data very well. The ability of the two turbulence models to predict the shock-induced separation point and the pressure level in the separated region is less encouraging. The Baldwin-Lomax algebraic model predicts the shock location farther upstream than the Jones-Launder, two-equation, k-ε model and seems to agree slightly better with the experimental data in this respect. In return, the Jones-Launder k-ε turbulence model generally predicts the pressure level in the separated region and the base pressures (i.e., the data points at x/L = 1.0) better than the Baldwin-Lomax model does. It also yielded a steady solution at this Mach number, unlike the Baldwin-Lomax model.

Figure 24 presents distributions of the ratio of the internal pressures to the jet total pressure for M_∞ = 0.938. As at M_∞ = 0.600, both turbulence models give results that agree extremely well with the experimental data. Other than a very slight difference in the predicted pressures where the internal shock cells compress the flow, no significant difference is noted between the results of the two models. Because there is no separation inside the nozzle and the boundary layer is extremely thin, these results would be expected.

The distributions of the skin-friction coefficients (fig. 25) are similar to the ones at M_∞ = 0.600 except for the separated regions. Up to the point of separation, the Jones-Launder k-ε turbulence model gives values of skin-friction coefficients that are approximately 20 to 25 percent higher than values predicted by the Baldwin-Lomax turbulence model; no experimental data were available for skin friction. Because the two models predict different types of flow and recirculation patterns in the separated regions, the corresponding skin-friction coefficients are also different. For instance, although the major part of the upper and lower flaps are separated for the Baldwin-Lomax solution, the underlying secondary separated region, where the flow direction is toward the nozzle exit (figs. 7(c) and 22(a)), gives positive values of skin friction. Keep in mind that the precise surface flow pattern and skin-friction distributions in this Baldwin-Lomax computation are artifacts of the unconverged solution.

Figure 26 shows the computed universal law-of-the-wall boundary layer profiles at M_∞ = 0.938. The profiles are at stations along the constant cross section of the model leading up to the nozzle-afterbody. Although the axial pressure gradients are stronger at this Mach number than they are at M_∞ = 0.600, the trends and characteristics of the law-of-the-wall boundary layer profiles are similar. Basically, both turbulence models predict a law-of-the-wall characteristic of the boundary layer, with the Jones-Launder k-ε model agreeing better with theory than the Baldwin-Lomax algebraic model does.

The velocity and pitot-pressure boundary layer profiles for the external and internal surfaces of the nozzle-afterbody are presented in figure 27. They are also similar to the profiles at M_∞ = 0.600 for the internal surface at all stations and for the first station on the external surface where the flow is still attached. However, at the last two stations (x/L = 0.9426 and 0.9999) behind the strong shock, a noticeable loss occurs in the maximum velocity throughout the boundary layer. The loss is much greater

for the Jones-Launder k-ε turbulence model than it is for the Baldwin-Lomax model.

The profiles on the top of the nozzle also show the extent of the separated region and the strength of the backflow in it. The Jones-Launder k-ε model predicts a separated region that is approximately half as thick as that predicted by the Baldwin-Lomax model. For the Jones-Launder k-ε model, the predicted speed of the backflow in the separated region near the nozzle exit (x/L = 0.9999) is approximately one-third of the speed of the backflow predicted by the Baldwin-Lomax model. One possible explanation for this effect is that the Baldwin-Lomax model only takes into account the local vorticity in computing the viscosity, whereas the Jones-Launder k-ε turbulence model takes into account a more three-dimensional picture of the vorticity and other mean flow variables. Another explanation, which may be more plausible, is that the Baldwin-Lomax model is a two-layer algebraic turbulence model. Once the eddy viscosity shifts from the inner-layer formulation to the outer-shear-layer formulation, the viscosity is substantially reduced and cannot revert to the inner-layer formulation. In contrast, the Jones-Launder k-ε turbulence model can continually adjust the viscosity. Hence, the reduced viscosity of the outer layer of the Baldwin-Lomax algebraic model would probably give a thicker separated region.

Jet Exhaust Plume

Computational results in the jet exhaust plume for the free-stream Mach number of 0.600 are presented in figures 28 and 29. These results are compared with extensive pitot-pressure data from reference 21. Although results for both the Jones-Launder k-ε and Baldwin-Lomax turbulence models are given, the turbulent dissipation downstream of the nozzle exit (grid block 3(a)) was calculated only with the Jones-Launder k-ε turbulence model. Only the flow in the vicinity of the model (grid blocks 2 and 4) was calculated with both turbulence models. Therefore, differences in the pitot-pressure profiles in the plume for the two turbulence models are the result of differences in the initial profiles at the jet exit station (x/L = 1.00).

This procedure was followed because, in the Jones-Launder k-ε turbulence model, the turbulent viscosity depends only on the flow, and, thus, the model is a logical choice to use in free-shear layers. In contrast, the turbulent viscosity in the Baldwin-Lomax model is a function of the nondimensional distance from a wall or, for free-shear flow, possibly from an imaginary surface. For a jet plume interacting with the external flow, the choice and definition of the surface becomes nebulous.

Mach number contours for the jet exhaust plume are presented in figure 28 for the vertical and horizontal planes of symmetry. Portions of the afterbody flow, internal flow, and jet exhaust plume (grid blocks 2, 4, and 3, respectively) are visible. The contours are given only for the Jones-Launder k-ε turbulence model. The Mach number contours illustrate the pattern of the expansion and compression cells in the aft section of the nozzle and the forward part of the exhaust plume. They also illustrate the accompanying local expansions and contractions of the plume itself. In addition, the overall spreading of the shear layer between the plume and the external flow clearly can be seen.

Figure 29 presents profiles of the ratio of the pitot pressure to the free-stream total pressure at four circumferential angles and three axial stations in the jet exhaust plume. The profiles at $\phi = 0°$ are in the vertical plane of symmetry, those at $\phi \approx 25°$ are in a plane that cuts through the top surface of the nozzle, those at $\phi \approx 65°$ are in a plane that intersects the nozzle at approximately the corner, and those at $\phi = 90°$ are in the horizontal plane of symmetry. The radial location of the nozzle exit (i.e., nozzle lip line) is indicated in figure 29. Available corresponding experimental data are included.

At the jet exit (x/L = 1.000), there are relatively minor differences between the profiles of the two turbulence models. The profiles are identical to the boundary layer profiles at the jet exit. Except for an apparent shift in the radial location of the profiles at the nozzle exit (i.e., the computed jet core extends farther out than the experimental core), they match the experimental data extremely well. Lack of modeling the nozzle base model possibly could cause the apparent shift. However, the nozzle base was modeled. Therefore, the shift was probably due to an error in the measurement of the location of the experimental rake. Except for the shift, both turbulence models predict the total pressure losses near the surface of the model well. The effect of the relatively large base of the nozzle at $\phi = 90°$ clearly appears in the profile.

At the downstream stations ($x/L \approx$ 1.081 and 1.162), the profiles indicate that the mixing between the exhaust plume and the external flow was underpredicted. Besides producing a plume that is not exactly correct, the deficiency in mixing may alter the influence of the jet plume on the afterbody flow.

The discrepancy between the computed profiles and experimental data seems to be significantly greater at $\phi \approx 65°$ than at other circumferential angles. At this angle, the discrepancy also seems to be growing as the distance downstream of the jet exit increases. As mentioned previously, a plane in this circumferential angle intersects the rectangularly shaped nozzle close to its corner. The relatively poor agreement at $\phi \approx 65°$ could be due to the grid topology, which is an O type in the

cross-flow plane but is generally a rectangular shape in the vicinity of the plume from the nozzle lip to the outflow boundary. This topology may not allow accurate resolution of the viscous terms in the corners.

Also, the poor agreement could be due to the turbulence model. The standard Jones-Launder k-ε turbulence model used in this investigation is linear. Reference 22 indicates that, although cross-flow vortices in the corners of internal ducts develop as they should when a nonlinear k-ε turbulence model is utilized, they do not develop at all for a linear k-ε model. Therefore, the linear model used in this investigation failed to develop any of the cross-flow vortices that would be present. Because cross-flow vortices would enhance mixing between the jet plume and external flow, the linear model should underpredict the mixing, as it does. Although this effect would be most noticeable at $\phi \approx 65°$, a secondary effect on the mixing could occur at other circumferential angles.[1]

Solutions, which predicted a higher mixing rate and agree much better with experimental data, have been obtained. (See ref. 16, for example.) In reference 16, these improved results were obtained by a standard Jones-Launder k-ε turbulence model with vortex-stretching and compressible-dissipation extensions. In this paper, no effort was made to tune the standard Jones-Launder k-ε turbulence model to increase mixing because the objective of the investigation was to evaluate the performance of the turbulence models without adjustment to any set of data.

Nozzle-Afterbody Drag

Often, the goal of computational fluid dynamics is to predict the performance characteristics of a new airplane or component. Figure 30 presents the buildup of the computed afterbody-drag coefficient for the external surface of the nozzle. Here, drag buildup is defined as the accumulated drag integrated with respect to axial distance from model station $x/L = 0.88$. Figure 30 presents the pressure drag, the skin-friction drag, and the total-drag coefficients for both turbulence models. The total drag is the combined skin-friction and pressure drags. The reference area used for computing the drag coefficient was the maximum cross-sectional area of the model. Unfortunately, no experimental drag data are available that could be used to validate the current computational predictions.

As expected, the pressure-drag coefficient builds up when the afterbody pressure coefficient is negative and decreases when the pressure coefficient is positive. (Compare the drag coefficient buildup with the pressure coefficient distributions in figs. 12 and 23.) Conversely, the skin-friction drag increases when the skin-friction coefficient is positive and decreases when it is negative.

At $M_\infty = 0.600$ (fig. 30(a)), the external flow is essentially attached, and the major difference in the drag between the two turbulence models stems from the differences in skin friction. At this condition, the Jones-Launder k-ε turbulence model gives approximately 50 percent higher friction drag, which also results in higher total drag.

At $M_\infty = 0.600$, the pressure-drag coefficient buildup for the two turbulence models are virtually the same over the initial part of the boattail. However, as the drag builds up, the Baldwin-Lomax model does result in slightly more drag than the Jones-Launder k-ε model. The pressure distributions for the external surface, as discussed previously (fig. 12), show a very slight difference in the pressures for the two turbulence models on the initial part of the boattail where the flow is accelerating and show a seemingly insignificant difference on the aft part of the boattail where the flow is compressing. The difference between drag results of the two turbulence models, although small, illustrates that seemingly insignificant differences in the predicted pressures can result in significant differences in the integrated drag.

At $M_\infty = 0.938$ (fig. 30(b)), the results for the skin-friction-drag coefficient buildup are similar to the results at $M_\infty = 0.600$. However, the differences between the pressure drag buildup of the two turbulence models reflect the substantial differences between the model shock location and pressure level predictions in the separated region. For transonic massively separated flow, the difference in the pressure-drag coefficient predictions overwhelms any difference due to skin-friction-drag coefficient predictions. The Jones-Launder k-ε turbulence model results in a higher drag than that of the Baldwin-Lomax model.

Although the buildups of the drag coefficient are different for the two turbulence models, the integrated drag coefficients predicted by each turbulence model for the entire nozzle are close to the same value. However, this result is just a coincidence. The potential for a large difference between predicted drag coefficients of the two

[1]Several different grids (table I) in the plume were investigated to determine any grid effect on the mixing between the plume and the external flow. Initially, block 3 ($57 \times 53 \times 153$) was tested downstream of the nozzle exit. While the number of radial grid planes was held constant, the radial spacing of the grid in the vicinity of the plume was adjusted in several steps. Finally, more axial grid planes were added, and the axial spacing was changed, which resulted in block 3(a) ($81 \times 53 \times 153$) downstream of the exit. New solutions were obtained at each intermediate step. These modifications to the grid produced a negligible effect on the solution. Although no noticeable improvement was obtained by the change in the grid, all the results presented at $M_\infty = 0.600$ were computed with block 3(a) downstream of the exit.

turbulence models exists (e.g., if the configuration happened to be truncated at $x/L = 0.97$).

Good performance predictions have been obtained for nozzles with relatively mild surface curvature and mildly accelerating attached flow. (See ref. 25.) However, the differences between the drag coefficient build-ups of the two turbulence models illustrate that substantial development is still required for computing very complex flows before nozzle performance can be accurately predicted for all flow conditions.

Current research efforts include implementation and evaluation of more advanced turbulence models such as explicit algebraic Reynolds stress models. Preliminary results show that the algebraic Reynolds stress model substantially improves the prediction of the pressure level in the separated region behind the shock at $M_\infty = 0.938$. However, the algebraic stress model fails to improve the overall prediction of the shock location for this test configuration. These preliminary results imply that further improvements in the algebraic stress models, or even more advanced turbulence models such as full Reynolds stress models, may be necessary to adequately predict performance.

Concluding Remarks

A numerical investigation was conducted to assess the accuracy of turbulence models for computing nonaxisymmetric nozzle-afterbody flows with propulsive jets. Navier-Stokes solutions were obtained for a convergent-divergent nonaxisymmetric nozzle-afterbody and its associated jet exhaust plume at free-stream Mach numbers of 0.600 and 0.938 at an angle of attack of 0°. The Reynolds number based on model length was approximately 20×10^6. The nozzle pressure ratio was 4.0, which is close to the design value of 4.25. Turbulent dissipation was modeled by the standard Jones-Launder k-ε turbulence model and by the Baldwin-Lomax algebraic turbulence model with the Degani-Schiff modification. The results were compared with experimental data.

At flow conditions with little or no flow separation and no strong shocks (e.g., external flow at low subsonic speeds or internal nozzle flow at a nozzle pressure ratio close to design), both turbulence models predicted the pressures on the surfaces of the nozzle very well, as was expected. The computed nozzle base pressures also agreed very well with the experimental data, particularly, where the base was thick and the nozzle boattail angle was small. When the flow was attached, the Jones-Launder k-ε turbulence model usually predicted a value of skin friction approximately 20 percent higher than the Baldwin-Lomax model predicted.

At transonic speeds, strong shocks and massive separation existed on the external surface. Downstream of the shock-induced separation point, both turbulence models were unable to predict the flow reliably. The Jones-Launder, two-equation, k-ε turbulence model generally predicted the pressure level in the separated region better than the Baldwin-Lomax algebraic turbulence model did. The Baldwin-Lomax model predicted the shock location farther upstream than the Jones-Launder k-ε model did and seemed to agree slightly better with the experimental data in this respect. Although neither turbulence model provided entirely satisfactory results for this separated flow, the Jones-Launder k-ε turbulence model predicted the base pressures better and seemed to predict the overall trends of the pressure distributions better.

The Jones-Launder k-ε turbulence model predicted a less extensive separated region than the Baldwin-Lomax model did for transonic flow. Separation was confined to the top and bottom of the nozzle for the Jones-Launder k-ε turbulence model. With the Baldwin-Lomax turbulence model, the separation extended partway down the sides of the nozzle, was approximately twice as thick at the trailing edge, and had a backflow speed in the separated region that was approximately two and a half times the speed predicted by the Jones-Launder k-ε turbulence model. Unlike the Jones-Launder k-ε turbulence model solution, the Baldwin-Lomax model solution failed to converge to a steady state at the high transonic Mach number.

Mixing between the exhaust plume and the external flow was underpredicted. The discrepancy between the computed pitot-pressure profiles and experimental data was significantly greater in a plane that intersected the nozzle approximately at its corner. Possible reasons for this discrepancy may be the effects of an O-type grid and failure of the standard Jones-Launder k-ε model to predict cross-flow vortices.

The differences between the drag coefficients predicted by the two turbulence models illustrate that substantial development is still required for computing very complex flows (e.g., flows with massive shock-induced separation) before nozzle performance can be predicted reliably, particularly at transonic speeds.

Current and future research efforts include implementation and evaluation of more advanced turbulence models such as explicit algebraic Reynolds stress models and full Reynolds stress models.

NASA Langley Research Center
Hampton, VA 23681-0001
April 23, 1996

Appendix A

Governing Equations

The Navier-Stokes equations mathematically model the physical laws governing the motion of a compressible fluid with dissipation. In PAB3D, the three-dimensional, time-dependent, Reynolds-averaged, Navier-Stokes equations are written in strong conservation form for a Cartesian coordinate system (x, y, z). Body forces are assumed to play an insignificant role in the afterbody flow problem and are neglected. Because the dominant dissipative effects for most aerodynamic problems arise mainly from diffusion normal to the main flow direction, only those diffusion terms normal to the generalized coordinate most nearly aligned with the free stream are retained. The resulting time-dependent equations for conservation of mass, linear momentum, and energy can be expressed in terms of a fixed generalized coordinate system (ξ, η, ζ) as

$$\hat{\mathbf{Q}}_t + \hat{\mathbf{F}}_\xi + (\hat{\mathbf{G}} - \hat{\mathbf{G}}_v)_\eta + (\hat{\mathbf{H}} - \hat{\mathbf{H}}_v)_\zeta = 0 \tag{A1}$$

where

$$\left.\begin{aligned} \hat{\mathbf{Q}} &= \frac{\mathbf{Q}}{J} & \hat{\mathbf{F}} &= \frac{1}{J}(\xi_x \mathbf{F} + \xi_y \mathbf{G} + \xi_z \mathbf{H}) \\ \hat{\mathbf{G}} &= \frac{1}{J}(\eta_x \mathbf{F} + \eta_y \mathbf{G} + \eta_z \mathbf{H}) & \hat{\mathbf{G}}_v &= \frac{1}{J}(\eta_x \mathbf{F}_v + \eta_y \mathbf{G}_v + \eta_z \mathbf{H}_v) \\ \hat{\mathbf{H}} &= \frac{1}{J}(\zeta_x \mathbf{F} + \zeta_y \mathbf{G} + \zeta_z \mathbf{H}) & \hat{\mathbf{H}}_v &= \frac{1}{J}(\zeta_x \mathbf{F}_v + \zeta_y \mathbf{G}_v + \zeta_z \mathbf{H}_v) \end{aligned}\right\} \tag{A2}$$

and

$$\left.\begin{aligned} \mathbf{Q}_t &= \begin{Bmatrix} \rho \\ \rho u \\ \rho v \\ \rho w \\ e \end{Bmatrix} \quad \mathbf{F}_\xi = \begin{Bmatrix} \rho u \\ \rho uu + p \\ \rho uv \\ \rho uw \\ (e+p)u \end{Bmatrix} \quad \mathbf{G} = \begin{Bmatrix} \rho v \\ \rho uv \\ \rho vv + p \\ \rho wv \\ (e+p)v \end{Bmatrix} \quad \mathbf{H} = \begin{Bmatrix} \rho w \\ \rho uw \\ \rho vw \\ \rho ww + p \\ (e+p)w \end{Bmatrix} \\ \mathbf{F}_v &= \begin{Bmatrix} 0 \\ \tau_{xx} \\ \tau_{xy} \\ \tau_{xz} \\ -q_x + u\tau_{xx} + v\tau_{xy} + w\tau_{xz} \end{Bmatrix} \quad \mathbf{G}_v = \begin{Bmatrix} 0 \\ \tau_{xy} \\ \tau_{yy} \\ \tau_{yz} \\ -q_y + u\tau_{xy} + v\tau_{yy} + w\tau_{yz} \end{Bmatrix} \\ \mathbf{H}_v &= \begin{Bmatrix} 0 \\ \tau_{xz} \\ \tau_{yz} \\ \tau_{zz} \\ -q_z + u\tau_{xz} + v\tau_{yz} + w\tau_{zz} \end{Bmatrix} \end{aligned}\right\} \tag{A3}$$

where

$$-q_i = \frac{1}{\gamma - 1}\left(\frac{\mu^L}{\mathrm{Pr}} + \frac{\mu^T}{\mathrm{Pr}_t}\right)\frac{\partial a^2}{\partial x_i} \tag{A4}$$

Here and later in the discussion, i, j, and k represent the x, y, and z components, respectively. In these equations, ρ is the density; u, v, and w are the velocity components in the x, y, and z directions, respectively; e is the total energy per unit volume; and p is the pressure. The relations between energy, pressure, and enthalpy for an ideal gas complete the system of equations.

The viscous stresses are assumed to be composed of a laminar component and a turbulent component (e.g., $\tau_{ij} = \tau_{ij}^L + \tau_{ij}^T$). The laminar stresses τ_{ij}^T are expressed as

$$\tau_{ij}^L = \mu^L\left[\left(\frac{\partial u_i}{\partial x_j} + \frac{\partial u_j}{\partial x_i}\right) - \frac{2}{3}\frac{\partial u_k}{\partial x_k}\delta_{ij}\right]$$

The expressions for the turbulent stresses τ_{ij}^T are described in the main body of the paper.

Appendix B

Mathematical Description of Model

External Geometry

The model, which was 63.04 in. long, consisted of a generic forebody with a nonaxisymmetric convergent-divergent nozzle attached. The model had a conical nose that blended smoothly into a superelliptical cross section at model station 26.50 in. This cross section was nearly rectangular with rounded corners. The external geometry then remained constant to fuselage station 55.05 in. where the nozzle connected to the forebody. The following equations define the external geometry up to this point:

$$\left.\begin{aligned} r' &= \left[\left(\frac{\cos\eta}{a}\right)^{\beta} + \left(\frac{\sin\eta}{b}\right)^{\beta}\right]^{-1/\beta} \\ y &= r'\cos\eta \\ z &= r'\sin\eta \end{aligned}\right\} \tag{B1}$$

where η is the circumferential angle.

From $x = 0$ to $x = 6.010$ in.,

$$\left.\begin{aligned} \beta &= 2.00 \\ a &= x\tan(14\pi/180) \\ b &= x\tan(14\pi/180) \end{aligned}\right\} \tag{B2}$$

From $x = 6.010$ to $x = 26.50$ in.,

$$\left.\begin{aligned} \beta &= 3.5\sin\left[\pi\left(\frac{x - 16.255}{20.490}\right)\right] + 5.50 \\ a &= -0.363118x - 9.924540 + \sqrt{-0.834887x^2 10^{-13} + 16.665089x + 84.948188} \\ b &= -0.209539x - 2.196445 + \sqrt{-0.213163x^2 10^{-13} + 4.546669x - 2.781034} \end{aligned}\right\} \tag{B3}$$

From $x = 26.50$ to $x = 55.05$ in.,

$$\left.\begin{aligned} \beta &= 9.0000 \\ a &= 3.4000 \\ b &= 3.1000 \end{aligned}\right\} \tag{B4}$$

From $x = 55.05$ to $x = 63.04$ in. is the nozzle.

Model station 55.05 in. is the nozzle connect station. Details of the nonaxisymmetric convergent-divergent nozzle are given in figure 4. The external cross-sectional geometry varied from the superellipse at the nozzle connect station to essentially a rectangle with superelliptical corners at the nozzle exit. The equation defining the external cross-sectional geometry of the nozzle is

$$\left(\frac{y - y_0}{a}\right)^{\beta} + \left(\frac{z - z_0}{b}\right)^{\beta} = 1.0 \tag{B5}$$

where y_0, z_0, a, b, and β are given in figure 4(b) as functions of x.

Internal Transition Section Geometry

The internal geometry of the model varied from a circular cross section at the instrumentation section (fig. 3) to a rectangular cross section at the nozzle connect station (model station 55.05 in.). The transition section provided a smooth constant-area transition between the instrumentation section and the nozzle by means of a superelliptical cross section. The equations for the semimajor axis, the semiminor axis, and the exponent of the superellipse for the transition section are

From $x = 49.90$ to $x = 52.87$ in.,

$$\left.\begin{aligned} a &= 2.4750 \\ b &= 19.2442185a\left[4\int_0^a (a^{\beta} - t)^{1/\beta}\,dt\right]^{-1} \\ \beta &= \frac{\ln 2}{\ln(\sqrt{2}/c)} \end{aligned}\right\} \tag{B6}$$

where

$$c = 1 + 0.207107\left[\sin\left(\pi\frac{x - 45.445000}{2.9700}\right) + 1\right]$$

and the cross-sectional area of the transition section is 19.2442185 in^2.

From $x = 52.87$ to $x = 55.05$ in., the internal cross section of the transition section was a rectangle with a semiwidth of 2.475 in. and a semiheight of 1.944 in. Ahead of model station 49.90 in., the cross section was circular with a diameter of 2.475 in.

References

1. Capone, F. J.: The Nonaxisymmetric Nozzle: It is for Real—Fighter Aircraft. AIAA-79-1810, Aug. 1979.

2. Swanson, R. Charles, Jr.: *Numerical Solutions of the Navier-Stokes Equations for Transonic Afterbody Flows.* NASA TP-1784, 1980.

3. Deiwert, George S.; and Rothmund, Herbert: Three-Dimensional Flow Over a Conical Afterbody Containing a Centered Propulsive Jet: A Numerical Simulation. AIAA-83-1709, July 1983.

4. Vatsa, V. N.; Thomas, J. L.; and Wedan, B. W.: Navier-Stokes Computations of Prolate Spheroids at Angle of Attack. AIAA-87-2627, Aug. 1987.

5. Carlson, John R.: *Evaluation and Application of VSAERO to a Nonaxisymmetric Afterbody With Thrust Vectoring.* SAE Paper 871775, Oct. 1987.

6. Compton, William B., III; Thomas, James L.; Abeyounis, William K.; and Mason, Mary L.: *Transonic Navier-Stokes Solutions of Three-Dimensional Afterbody Flows.* NASA TM-4111, 1989.

7. Abdol-Hamid, Khaled S.; and Compton, William B., III: Supersonic Navier-Stokes Simulations of Turbulent Afterbody Flows. AIAA-89-2194, July–Aug. 1989.

8. Compton, William B., III; and Abdol-Hamid, Khaled S.: Navier-Stokes Simulation of Nozzle-Afterbody Flows With Jets at Off-Design Conditions. AIAA-91-3207, Sept. 1991.

9. Compton, William B., III; Abdol-Hamid, Khaled S.; and Abeyounis, William K.: Comparison of Algebraic Turbulence Models for Afterbody Flows With Jet Exhaust. *AIAA J.*, vol. 30, no. 11, Nov. 1992, pp. 2716–2722.

10. *Aerodynamics of 3-D Aircraft Afterbodies.* AGARD-AR-318, Sept. 1995.

11. Jones, W. P.; and Launder, B. E.: The Calculation of Low-Reynolds-Number Phenomena With a Two-Equation Model of Turbulence. *Int. J. Heat & Mass Transf.*, vol. 16, June 1973, pp. 1119–1130.

12. Abdol-Hamid, Khaled S.; Lakshmanan, B.; and Carlson, John R.: *Application of Navier-Stokes Code PAB3D With* κ-ε *Turbulence Model to Attached and Separated Flows.* NASA TP-3480, 1995.

13. Baldwin, Barrett; and Lomax, Harvard: Thin-Layer Approximation and Algebraic Model for Separated Turbulent Flows. AIAA-78-257, Jan. 1978.

14. Degani, David; and Schiff, Lewis B.: Computation of Supersonic Viscous Flows Around Pointed Bodies at Large Incidence. AIAA-83-0034, Jan. 1983.

15. Abdol-Hamid, Khaled S.: The Application of 3D Marching Scheme for the Prediction of Supersonic Free Jets. AIAA-89-2897, July 1989.

16. Dash, S. M.; and Kenzakowski, D. C.: Recent Advances in Jet Flowfield Simulation. I—Steady Flows. AIAA-93-4390, Oct. 1993.

17. Wilcox, David C.: Progress in Hypersonic Turbulence Modeling. AIAA-91-1785, June 1991.

18. Launder, B. E.; and Sharma, B. I.: Application of the Energy-Dissipation Model of Turbulence to the Calculation of Flow Near a Spinning Disc. *Lett. Heat & Mass Transf.*, vol. 1, Nov.–Dec. 1974, pp. 131–137.

19. Cebeci, Tuncer: Calculation of Compressible Turbulent Boundary Layers With Heat and Mass Transfer. AIAA-70-741, June–July 1970.

20. Corson, Blake W., Jr.; Runckel, Jack F.; and Igoe, William B.: *Calibration of the Langley 16-Foot Transonic Tunnel With Test Section Air Removal.* NASA TR R-423, 1974.

21. Putnam, Lawrence E.; and Mercer, Charles E.: *Pitot-Pressure Measurements in Flow Fields Behind a Rectangular Nozzle With Exhaust Jet for Free-Stream Mach Numbers of 0.00, 0.60, and 1.20.* NASA TM-88990, 1986.

22. Lakshmanan, B.; Chylek, T.; and Tiwari, S. N.: Application of Nonlinear κ-ε Model to Supersonic Separated Flows. AIAA-95-0228, Jan. 1995.

23. Driver, David M.: Reynolds Shear Stress Measurements in a Separated Boundary Layer Flow. AIAA-91-1787, June 1991.

24. Ludwieg, H.; and Tillmann, W.: *Investigations of the Wall-Shearing Stress in Turbulent Boundary Layers.* NACA TM 1285, 1950.

25. Carlson, John R.: *Computational Prediction of Isolated Performance of an Axismmetric Nozzle at Mach Number 0.90.* NASA TM-4506, 1994.

Table I. Block Structure and Mesh Density for Computational Grid

Block	Location	Topology	Number of grid planes in direction—		
			i (streamwise)	*j* (circumferential)	*k* (radial)
1	Upstream	H-O	25	53	77
2	Model external	H-O	113	53	77
3	Downstream	H-O	57	53	153
[a]3(a)	Downstream	H-O	81	53	153
4	Nozzle internal	H-O	89	53	49

[a]Block 3(a) is a substitute for block 3 with a modified grid distribution and density.

Table II. Experimental Surface Pressures

External surface				Internal surface			
		C_p for—				$p/p_{t,j}$ for—	
Row	x, in.	$M_\infty = 0.600$; NPR = 4.003	$M_\infty = 0.938$; NPR = 4.017	Row	x, in.	$M_\infty = 0.600$; NPR = 4.003	$M_\infty = 0.938$; NPR = 4.017
1	55.180	–0.1744	–0.1127	6	55.800	0.9572	0.9598
1	55.800	–.2654	–.2056	6	56.730	.8677	.8645
1	57.040	–.3833	–.5296	6	57.223	.2527	.2505
1	57.660	–.3566	–.4815	6	58.280	.4113	.4128
1	58.280	–.2762	–.1606	6	60.140	.3436	.3434
1	58.900	–.1587	–.1166	6	62.620	.2447	.2411
1	59.520	–.0466	–.1081				
1	60.140	.0244	–.1014	7	58.280	.4216	.4232
1	61.380	.1143	–.0719	7	60.140	.3262	.3267
1	62.620	.1743	–.0101	7	62.620	.2594	.2589
1	Base	.1653	.0479				
				8	57.223	.2549	.2540
2	55.800	–.2333	–.1901	8	58.280	.4137	.4163
2	58.280	–.2677	–.1775	8	60.140	.3255	.3259
2	59.520	–.0580	–.1201	8	62.620	.2600	.2598
2	61.380	.0947	–.0768				
				9	57.223	.6031	.5754
3	55.800	–.1767	–.1682	9	58.280	.3075	.3022
3	56.420	–.2215	–.2715	9	60.140	.2839	.2842
3	57.040	–.2500	–.3898	9	62.620	.2429	.2400
3	58.280	–.2863	–.4545				
3	59.520	–.2078	–.1431				
3	61.380	.0129	–.1535				
3	62.620	.1090	.0063				
3	Base	–.0583	–.0296				
4	57.040	–.2225	–.4547				
4	58.280	–.1514	–.4009				
4	59.520	–.1716	–.1416				
4	61.380	.0267	–.0072				
5	55.180	–.1271	–.0952				
5	55.800	–.2104	–.2005				
5	56.420	–.2798	–.4026				
5	57.040	–.2256	–.5292				
5	58.280	–.1120	–.3812				
5	59.520	–.0640	–.1498				
5	61.380	.0201	.0068				
5	62.610	.0383	.0300				
5	Base	–.0293	.0023				

Table III. Jet Exhaust Plume Experimental Data

[Excerpted from ref. 21]

(a) $x/L \approx 1.00$; $\phi \approx 15°$

x, in.	y, in.	z, in.	r, in.	ϕ, deg	$p_{pitot}/p_{t,\infty}$
62.86787	−0.14663	0.11929	0.19	−50.87	2.749
62.86963	−.11207	.21021	.24	−28.06	2.749
62.87138	−.06327	.31391	.32	−11.40	2.750
62.86963	−.03476	.41355	.42	−4.80	2.760
62.86787	.00097	.50754	.51	.11	2.848
62.86787	.03104	.58665	.59	3.03	2.855
62.86963	.06561	.67758	.68	5.53	2.861
62.87138	.12354	.77770	.79	9.03	2.863
62.86963	.14291	.88092	.89	9.21	2.862
62.86787	.17865	.97491	.99	10.38	2.851
62.86787	.20872	1.05402	1.07	11.20	2.749
62.86963	.24329	1.14494	1.17	12.00	1.521
62.87138	.31036	1.24148	1.28	14.04	.831
62.86963	.32059	1.34828	1.39	13.38	.835
62.86787	.35632	1.44228	1.49	13.88	.846
62.86787	.38640	1.52139	1.57	14.25	.864
62.86963	.42097	1.61231	1.67	14.63	.879
62.87138	.49718	1.70527	1.78	16.25	.900
62.86963	.49827	1.81565	1.88	15.35	.915
62.86787	.53400	1.90964	1.98	15.62	.926
62.86787	.56408	1.98875	2.07	15.84	.940
62.86963	.59864	2.07967	2.16	16.06	.950
62.87138	.68400	2.16906	2.27	17.50	.960
62.86963	.67595	2.28301	2.38	16.49	.968
62.86787	.71168	2.37701	2.48	16.67	.978
62.86787	.74176	2.45612	2.57	16.80	.986
62.86963	.77632	2.54704	2.66	16.95	.991
62.87138	.87082	2.63285	2.77	18.30	.994
62.86963	.85363	2.75038	2.88	17.24	.996
62.86787	.88936	2.84437	2.98	17.36	.996
62.86436	.91718	2.91755	3.06	17.45	.995
62.86963	.95400	3.01440	3.16	17.56	.995
62.86085	.98958	3.10799	3.26	17.66	.994
62.86963	1.03130	3.21774	3.38	17.77	.995
62.86787	1.06703	3.31174	3.48	17.86	.994
62.86436	1.09486	3.38492	3.56	17.92	.996
62.86085	1.13759	3.49734	3.68	18.02	.996
62.86085	1.16726	3.57536	3.76	18.08	.996
62.84679	1.20486	3.67427	3.87	18.16	.996
62.86436	1.27253	3.85228	4.06	18.28	.995
62.86085	1.31527	3.96470	4.18	18.35	.995
62.86085	1.34493	4.04272	4.26	18.40	.996
62.84679	1.38253	4.14163	4.37	18.46	.995
62.86436	1.45021	4.31965	4.56	18.56	.994

Table III. Continued

(b) $x/L \approx 1.00$; $\phi \approx 66°$

x, in.	y, in.	z, in.	r, in.	ϕ, deg	$p_{pitot}/p_{t,\infty}$
62.86787	0.01625	0.00331	0.02	78.49	2.726
62.86787	.07965	.03984	.09	63.43	2.727
62.86436	.15560	.07444	.17	64.43	2.728
62.86436	.25201	.11805	.28	64.90	2.731
62.85558	.35081	.16275	.39	65.11	2.736
62.86787	.43930	.20278	.48	65.22	2.731
62.86787	.53533	.24563	.59	65.35	2.739
62.86436	.61116	.28053	.67	65.34	2.752
62.86436	.70756	.32414	.78	65.39	2.762
62.85558	.80636	.36883	.89	65.42	2.793
62.86787	.89485	.40887	.98	65.44	2.841
62.86787	.99102	.45142	1.09	65.51	2.839
62.86436	1.06671	.48661	1.17	65.48	2.836
62.86436	1.16312	.53022	1.28	65.49	2.831
62.85558	1.26192	.57492	1.39	65.51	2.829
62.86787	1.35041	.61495	1.48	65.52	2.828
62.86787	1.44670	.65721	1.59	65.57	2.829
62.86436	1.52226	.69270	1.67	65.53	2.829
62.86436	1.61867	.73631	1.78	65.54	2.832
62.85558	1.71747	.78100	1.89	65.55	2.831
62.86787	1.80596	.82103	1.98	65.55	2.827
62.86787	1.90239	.86301	2.09	65.60	2.820
62.86436	1.97782	.89878	2.17	65.56	2.816
62.86436	2.07422	.94239	2.28	65.57	2.814
62.85558	2.17303	.98709	2.39	65.57	2.803
62.86787	2.26151	1.02712	2.48	65.57	2.769
62.86787	2.35807	1.06880	2.59	65.62	2.724
62.86436	2.43337	1.10486	2.67	65.58	2.637
62.86436	2.52978	1.14848	2.78	65.58	1.264
62.85558	2.62858	1.19317	2.89	65.59	.852
62.86787	2.71707	1.23320	2.98	65.59	.863
62.86787	2.81376	1.27459	3.09	65.63	.898
62.86436	2.88892	1.31095	3.17	65.59	.921
62.86436	2.98533	1.35456	3.28	65.59	.948
62.85558	3.08413	1.39926	3.39	65.60	.969
62.82747	3.17942	1.44236	3.49	65.60	.985
62.82396	3.25929	1.47309	3.58	65.68	.992
62.81693	3.36242	1.52097	3.69	65.66	.996
62.81518	3.44562	1.55709	3.78	65.68	.996
62.82747	3.63497	1.64845	3.99	65.61	.998
62.82396	3.71510	1.67859	4.08	65.69	.998
62.81693	3.81817	1.72662	4.19	65.67	.998
62.81518	3.90144	1.76259	4.28	65.69	.998
62.82747	4.09052	1.85453	4.49	65.61	.997

Table III. Continued

(c) $x/L \approx 1.08$; $\phi \approx -7°$

x, in.	y, in.	z, in.	r, in.	ϕ, deg	$p_{pitot}/p_{t,\infty}$
68.11902	–0.23782	0.12131	0.27	–62.97	2.633
68.08737	–.24150	.23168	.33	–46.19	2.635
68.07683	–.24617	.43014	.50	–29.78	2.662
68.08210	–.24166	.54991	.60	–23.72	2.681
68.11902	–.25547	.62100	.67	–22.36	2.725
68.08737	–.25884	.73138	.78	–19.49	2.725
68.07683	–.26141	.92991	.97	–15.70	2.489
68.08210	–.25063	1.04983	1.08	–13.43	2.242
68.11902	–.27313	1.12069	1.15	–13.70	1.670
68.08737	–.27617	1.23108	1.26	–12.64	1.460
68.07683	–.27665	1.42968	1.46	–10.95	1.110
68.08210	–.25960	1.54975	1.57	–9.51	1.027
68.11902	–.29078	1.62038	1.65	–10.17	.965
68.08737	–.29350	1.73078	1.76	–9.62	.965
68.07683	–.29189	1.92944	1.95	–8.60	.977
68.08210	–.26857	2.04967	2.07	–7.46	.987
68.11902	–.30844	2.12006	2.14	–8.28	.994
68.08737	–.31083	2.23048	2.25	–7.93	.997
68.07683	–.30714	2.42921	2.45	–7.21	.997
68.08210	–.27754	2.54958	2.56	–6.21	.997
68.11902	–.32609	2.61975	2.64	–7.10	.997
68.08737	–.32816	2.73018	2.75	–6.85	.998
68.07683	–.32238	2.92898	2.95	–6.28	.998
68.08210	–.28650	3.04950	3.06	–5.37	.998
68.11902	–.34374	3.11944	3.14	–6.29	.999
68.08737	–.34549	3.22988	3.25	–6.11	.999
68.07683	–.34108	3.32526	3.34	–5.86	.996
68.07683	–.33762	3.42875	3.45	–5.62	.998
68.08210	–.29547	3.54942	3.56	–4.76	.997
68.07683	–.36029	3.65654	3.67	–5.63	.997
68.07683	–.36566	3.73987	3.76	–5.58	.997
68.07683	–.36270	3.76169	3.78	–5.51	.996
68.07683	–.35729	3.82500	3.84	–5.34	.996
68.07683	–.30494	3.93220	3.94	–4.43	.998
68.07683	–.37762	4.15624	4.17	–5.19	.997
68.07683	–.38332	4.23956	4.26	–5.17	.998
68.07683	–.37987	4.26139	4.28	–5.09	.998
68.07683	–.37349	4.32474	4.34	–4.94	.998
68.07683	–.31423	4.43211	4.44	–4.06	.997
68.07683	–.39495	4.65593	4.67	–4.85	.999

Table III. Continued

(d) $x/L \approx 1.08$; $\phi \approx 26°$

x, in.	y, in.	z, in.	r, in.	ϕ, deg	$p_{pitot}/p_{t,\infty}$
68.18931	−0.11589	0.09895	0.15	−49.51	2.633
68.18931	−.06324	.19074	.20	−18.34	2.640
68.18578	−.01333	.27805	.28	−2.74	2.652
68.18578	.04256	.37555	.38	6.47	2.668
68.18578	.08327	.44617	.45	10.57	2.679
68.18931	.13288	.53267	.55	14.01	2.717
68.18931	.18553	.62446	.65	16.55	2.733
68.18578	.23530	.71185	.75	18.29	2.722
68.18578	.29119	.80935	.86	19.79	2.610
68.18578	.33204	.8799	.94	20.67	2.517
68.18931	.38165	.96639	1.04	21.55	2.035
68.18931	.43430	1.05818	1.14	22.31	1.755
68.18578	.48393	1.14565	1.24	22.90	1.531
68.18578	.53982	1.24316	1.36	23.47	1.281
68.18578	.58081	1.31362	1.44	23.85	1.201
68.18931	.63041	1.40011	1.54	24.24	1.021
68.18931	.68307	1.49191	1.64	24.60	.980
68.18578	.73256	1.57945	1.74	24.88	.965
68.18578	.78845	1.67696	1.85	25.18	.963
68.18578	.82957	1.74734	1.93	25.40	.965
68.18931	.87918	1.83383	2.03	25.61	.975
68.18931	.93183	1.92563	2.14	25.82	.983
68.18578	.98119	2.01325	2.24	25.98	.989
68.18578	1.03708	2.11076	2.35	26.17	.993
68.18578	1.07834	2.18106	2.43	26.31	.996
68.18931	1.12795	2.26755	2.53	26.45	.997
68.18931	1.18060	2.35935	2.64	26.58	.997
68.18578	1.22982	2.44705	2.74	26.68	.997
68.18578	1.28570	2.54456	2.85	26.81	.997
68.18578	1.32711	2.61478	2.93	26.91	.997
68.18931	1.37672	2.70127	3.03	27.01	.999
68.18931	1.42937	2.79307	3.14	27.10	1.000
68.18578	1.47845	2.88085	3.24	27.17	.999
68.18578	1.53433	2.97836	3.35	27.26	.999
68.18578	1.57588	3.04850	3.43	27.34	.999
68.18578	1.61921	3.12405	3.52	27.40	.997
68.18578	1.68625	3.24093	3.65	27.49	.997
68.18403	1.72386	3.30650	3.73	27.54	.997
68.18228	1.79758	3.40361	3.85	27.84	.997
68.18578	1.86798	3.55777	4.02	27.70	.998
68.18578	1.93502	3.67465	4.15	27.77	.998
68.18403	1.97263	3.74022	4.23	27.81	.998
68.18228	2.04802	3.83637	4.35	28.10	.998
68.18578	2.11675	3.99149	4.52	27.94	1.000

Table III. Continued

(e) $x/L \approx 1.08$; $\phi \approx 65°$

x, in.	y, in.	z, in.	r, in.	ϕ, deg	$p_{pitot}/p_{t,\infty}$
68.18931	–0.02583	–0.00606	0.03	256.80	2.642
68.18578	.08165	.04339	.09	62.01	2.645
68.18578	.16824	.08323	.19	63.68	2.651
68.18578	.26557	.12801	.29	64.27	2.661
68.19107	.33713	.16115	.37	64.45	2.668
68.18931	.42840	.20292	.47	64.65	2.678
68.18578	.53588	.25237	.59	64.78	2.687
68.18578	.62247	.29221	.69	64.85	2.696
68.18578	.71980	.33699	.79	64.91	2.708
68.19107	.79129	.37029	.87	64.92	2.715
68.18931	.88263	.41191	.97	64.98	2.739
68.18578	.99010	.46136	1.09	65.02	2.744
68.18578	1.07670	.50120	1.19	65.04	2.751
68.18578	1.17403	.54598	1.29	65.06	2.756
68.19107	1.24545	.57942	1.37	65.05	2.757
68.18931	1.33686	.62090	1.47	65.09	2.708
68.18578	1.44434	.67035	1.59	65.10	2.673
68.18578	1.53093	.71019	1.69	65.11	2.637
68.18578	1.62826	.75497	1.79	65.12	2.562
68.19107	1.69962	.78855	1.87	65.11	2.505
68.18931	1.79109	.82988	1.97	65.14	2.250
68.18578	1.89856	.87933	2.09	65.15	2.097
68.18578	1.98515	.91917	2.19	65.15	1.978
68.18578	2.08249	.96395	2.29	65.16	1.811
68.19107	2.15378	.99768	2.37	65.15	1.713
68.18931	2.24532	1.03887	2.47	65.17	1.382
68.18578	2.35279	1.08832	2.59	65.18	1.260
68.18578	2.43938	1.12816	2.69	65.18	1.184
68.18578	2.53672	1.17294	2.79	65.18	1.097
68.19107	2.60794	1.20682	2.87	65.17	1.063
68.18931	2.69955	1.24786	2.97	65.19	.988
68.18578	2.80702	1.29731	3.09	65.20	.980
68.18578	2.89361	1.33715	3.19	65.20	.979
68.18578	2.99094	1.38193	3.29	65.20	.988
68.19107	3.06210	1.41595	3.37	65.18	.993
68.18931	3.26117	1.48724	3.58	65.48	.999
68.18931	3.36916	1.51959	3.70	65.72	.997
68.18931	3.45923	1.52740	3.78	66.18	.997
68.18931	3.71633	1.69418	4.08	65.49	.998
68.18931	3.82513	1.72477	4.20	65.73	.999
68.18931	3.91670	1.72920	4.28	66.18	.998

Table III. Continued

(f) $x/L \approx 1.08$; $\phi \approx 92°$

x, in.	y, in.	z, in.	r, in.	ϕ, deg	$p_{pitot}/p_{t,\infty}$
68.18931	0.00000	−0.10007	0.10	180.00	2.653
68.18931	.12488	−.10011	.16	128.72	2.657
68.18931	.22546	−.10015	.25	113.95	2.660
68.18931	.31616	−.10018	.33	107.58	2.662
68.18931	.39964	−.10020	.41	104.08	2.663
68.18931	.50000	−.10024	.51	101.34	2.665
68.18931	.62488	−.10027	.63	99.12	2.668
68.18931	.72546	−.10031	.73	97.87	2.669
68.18931	.81617	−.10034	.82	97.01	2.675
68.18931	.89964	−.10036	.91	96.37	2.678
68.18931	1.00000	−.10040	1.01	95.73	2.697
68.18931	1.12488	−.10044	1.13	95.10	2.707
68.18931	1.22546	−.10047	1.23	94.69	2.714
68.18931	1.31616	−.10050	1.32	94.37	2.722
68.18931	1.39964	−.10052	1.40	94.11	2.728
68.18931	1.50000	−.10056	1.50	93.84	2.747
68.18931	1.62488	−.10060	1.63	93.54	2.752
68.18931	1.72546	−.10063	1.73	93.34	2.758
68.18931	1.81616	−.10066	1.82	93.17	2.762
68.18931	1.89964	−.10068	1.90	93.03	2.729
68.18931	2.00000	−.10072	2.00	92.88	2.452
68.18931	2.12488	−.10076	2.13	92.71	2.052
68.18931	2.22546	−.10079	2.23	92.59	1.687
68.18931	2.31616	−.10082	2.32	92.49	1.393
68.18931	2.39964	−.10085	2.40	92.41	1.235
68.18931	2.50000	−.10088	2.50	92.31	1.042
68.18931	2.62488	−.10092	2.63	92.20	.972
68.18931	2.72546	−.10095	2.73	92.12	.958
68.18931	2.81616	−.10098	2.82	92.05	.966
68.18931	2.89964	−.10101	2.90	92.00	.972
68.19107	3.00908	−.10104	3.01	91.92	.982
68.18931	3.11293	−.10107	3.11	91.86	.989
68.18931	3.20890	−.10111	3.21	91.80	.995
68.18931	3.30223	−.10114	3.30	91.75	.996
68.18931	3.39964	−.10117	3.40	91.70	.999
68.19107	3.50908	−.10120	3.51	91.65	.997
68.18931	3.61293	−.10124	3.61	91.61	.997
68.18931	3.70890	−.10127	3.71	91.56	.997
68.18931	3.80223	−.10130	3.80	91.53	.997
68.19107	4.00908	−.10136	4.01	91.45	.998
68.18931	4.11293	−.10140	4.11	91.41	.998
68.18931	4.20890	−.10143	4.21	91.38	.998
68.18931	4.30223	−.10146	4.30	91.35	.998
68.19107	4.50908	−.10152	4.51	91.29	1.000

Table III. Continued

(g) $x/L \approx 1.16$; $\phi \approx -5°$

x, in.	y, in.	z, in.	r, in.	ϕ, deg	$p_{pitot}/p_{t,\infty}$
73.22530	–0.23118	0.14183	0.27	–58.47	2.695
73.22530	–.23168	.24435	.34	–43.48	2.706
73.22706	–.24094	.32965	.41	–36.16	2.717
73.22706	–.24339	.42557	.49	–29.77	2.719
73.22706	–.23311	.53942	.59	–23.37	2.706
73.22530	–.23361	.64182	.68	–20.00	2.641
73.22530	–.23411	.74434	.78	–17.46	2.565
73.22706	–.25367	.82948	.87	–17.00	2.459
73.22706	–.25612	.92540	.96	–15.47	2.302
73.22706	–.23555	1.03942	1.07	–12.77	2.122
73.22530	–.23605	1.14181	1.17	–11.68	1.846
73.22530	–.23654	1.24433	1.27	–10.76	1.700
73.22706	–.26641	1.32932	1.36	–11.33	1.566
73.22706	–.26885	1.42524	1.45	–10.68	1.430
73.22706	–.23798	1.53941	1.56	–8.79	1.306
73.22530	–.23848	1.64181	1.66	–8.26	1.155
73.22530	–.23898	1.74433	1.76	–7.80	1.099
73.22706	–.27914	1.82916	1.85	–8.68	1.055
73.22706	–.28158	1.92508	1.95	–8.32	1.023
73.22706	–.24042	2.03941	2.05	–6.72	1.003
73.22530	–.24092	2.14180	2.16	–6.42	.998
73.22530	–.24141	2.24432	2.26	–6.14	.998
73.22706	–.29187	2.32900	2.35	–7.14	.999
73.22706	–.29431	2.42492	2.44	–6.92	.999
73.22706	–.24285	2.53940	2.55	–5.46	.998
73.22530	–.24335	2.64180	2.65	–5.26	.999
73.22530	–.24385	2.74432	2.76	–5.08	.999
73.22706	–.30460	2.82884	2.85	–6.15	.999
73.22706	–.30704	2.92476	2.94	–5.99	.999
73.22706	–.24528	3.03939	3.05	–4.61	.998
73.22530	–.23740	3.12678	3.14	–4.34	.996
73.22530	–.21191	3.23189	3.24	–3.75	.998
73.22530	–.24453	3.33837	3.35	–4.19	.998
73.22530	–.24725	3.44220	3.45	–4.11	.998
73.22706	–.24772	3.53939	3.55	–4.00	.999
73.22530	–.23855	3.62678	3.63	–3.76	.998
73.22530	–.20919	3.73188	3.74	–3.21	.998
73.22530	–.24664	3.83837	3.85	–3.68	.998
73.22530	–.24968	3.94219	3.95	–3.62	.998
73.22530	–.23970	4.12678	4.13	–3.32	.995
73.22530	–.20648	4.23188	4.24	–2.79	.995
73.22530	–.24875	4.33836	4.35	–3.28	.995
73.22530	–.25211	4.44219	4.45	–3.25	.995
73.22530	–.24084	4.62678	4.63	–2.98	.996

Table III. Continued

(h) $x/L \approx 1.16$; $\phi \approx 25°$

x, in.	y, in.	z, in.	r, in.	ϕ, deg	$p_{pitot}/p_{t,\infty}$
73.22706	–0.11425	0.11233	0.16	–45.49	2.686
73.22530	–.06428	.20260	.21	–17.60	2.702
73.22706	–.01150	.29057	.29	–2.27	2.71
73.22530	.03362	.37301	.37	5.15	2.718
73.22882	.07093	.46493	.47	8.67	2.714
73.22706	.12507	.55133	.57	12.78	2.669
73.22530	.17589	.64114	.66	15.34	2.629
73.22706	.23261	.72693	.76	17.74	2.558
73.22530	.27703	.80976	.86	18.89	2.451
73.22882	.30601	.90623	.96	18.66	2.326
73.22706	.36440	.99034	1.06	20.20	2.055
73.22530	.41606	1.07968	1.16	21.07	1.917
73.22706	.47672	1.16329	1.26	22.28	1.773
73.22530	.52044	1.24651	1.35	22.66	1.626
73.22882	.54108	1.34752	1.45	21.88	1.501
73.22706	.60372	1.42934	1.55	22.90	1.307
73.22530	.65623	1.51822	1.65	23.38	1.227
73.22706	.72083	1.59964	1.75	24.26	1.158
73.22530	.76385	1.68326	1.85	24.41	1.096
73.22882	.77616	1.78881	1.95	23.46	1.052
73.22706	.84304	1.86834	2.05	24.29	1.013
73.22530	.89640	1.95676	2.15	24.61	1.003
73.22706	.96495	2.03600	2.25	25.36	.998
73.22530	1.00726	2.12001	2.35	25.41	.997
73.22882	1.01123	2.23011	2.45	24.39	.999
73.22706	1.08237	2.30735	2.55	25.13	.998
73.22530	1.13657	2.39530	2.65	25.38	.998
73.22706	1.20906	2.47236	2.75	26.06	.998
73.22530	1.25067	2.55676	2.85	26.07	.999
73.22882	1.24630	2.67140	2.95	25.01	.999
73.23057	1.35567	2.73443	3.05	26.37	.997
73.22530	1.40700	2.82620	3.16	26.47	.997
73.22706	1.45129	2.90082	3.24	26.58	.998
73.22530	1.49950	2.98455	3.34	26.68	.997
73.22882	1.48138	3.11270	3.45	25.45	.999
73.23057	1.59978	3.17079	3.55	26.77	.999
73.22530	1.65111	3.26256	3.66	26.84	.998
73.22706	1.69568	3.33702	3.74	26.94	.998
73.22530	1.74403	3.42067	3.84	27.01	.998
73.23057	1.84389	3.60715	4.05	27.08	.995
73.22530	1.89523	3.69891	4.16	27.13	.995
73.22706	1.94007	3.77322	4.24	27.21	.995
73.22530	1.98857	3.85679	4.34	27.28	.995
73.23057	2.08800	4.04351	4.55	27.31	.996

Table III. Continued

(i) $x/L \approx 1.16$; $\phi \approx 64°$

x, in.	y, in.	z, in.	r, in.	ϕ, deg	$p_{pitot}/p_{t,\infty}$
73.33074	−0.01269	0.00306	0.01	−76.44	2.695
73.33074	.07757	.04587	.09	59.40	2.694
73.31844	.17733	.09318	.20	62.28	2.701
73.33250	.25512	.13007	.29	62.99	2.706
73.33250	.34894	.17456	.39	63.42	2.713
73.33074	.43909	.21731	.49	63.67	2.723
73.33074	.52934	.26012	.59	63.83	2.723
73.31844	.62910	.30743	.70	63.96	2.721
73.33250	.70689	.34432	.79	64.03	2.717
73.33250	.80071	.38881	.89	64.10	2.715
73.33074	.89086	.43156	.99	64.15	2.675
73.33074	.98111	.47437	1.09	64.20	2.651
73.31844	1.08087	.52168	1.20	64.24	2.603
73.33250	1.15866	.55857	1.29	64.26	2.564
73.33250	1.25248	.60306	1.39	64.29	2.530
73.33074	1.34263	.64581	1.49	64.31	2.395
73.33074	1.43288	.68862	1.59	64.33	2.327
73.31844	1.53264	.73593	1.70	64.35	2.229
73.33250	1.61043	.77282	1.79	64.36	2.146
73.33250	1.70425	.81731	1.89	64.38	2.072
73.33074	1.79440	.86006	1.99	64.39	1.951
73.33074	1.88465	.90287	2.09	64.40	1.859
73.31844	1.98441	.95018	2.20	64.41	1.738
73.33250	2.06220	.98707	2.29	64.42	1.632
73.33250	2.15602	1.03156	2.39	64.43	1.533
73.33074	2.24617	1.07432	2.49	64.44	1.368
73.33074	2.33643	1.11712	2.59	64.45	1.297
73.31844	2.43618	1.16443	2.70	64.45	1.218
73.33250	2.51397	1.20132	2.79	64.46	1.163
73.33250	2.60779	1.24582	2.89	64.46	1.119
73.33074	2.69794	1.28857	2.99	64.47	1.062
73.33074	2.78820	1.33137	3.09	64.48	1.046
73.31844	2.88795	1.37868	3.20	64.48	1.030
73.33250	2.96574	1.41557	3.29	64.48	1.024
73.33250	3.05956	1.46007	3.39	64.49	1.012
73.33074	3.22381	1.55980	3.58	64.18	1.011
73.33777	3.29761	1.65718	3.69	63.32	1.004
73.32723	3.39629	1.68599	3.79	63.60	1.000
73.33425	3.60456	1.72912	4.00	64.37	.995
73.33074	3.67447	1.77637	4.08	64.20	.996
73.33777	3.74516	1.88011	4.19	63.34	.996
73.32723	3.84484	1.90690	4.29	63.62	.996
73.33425	4.05585	1.94439	4.50	64.39	.997

Table III. Concluded

(j) $x/L \approx 1.16$; $\phi \approx 92°$

x, in.	y, in.	z, in.	r, in.	ϕ, deg	$p_{pitot}/p_{t,\infty}$
73.33777	0.00722	−0.10206	0.10	94.05	2.681
73.33953	.10842	−.10349	.15	136.33	2.694
73.33777	.20108	−.10444	.23	152.55	2.700
73.33777	.30491	−.10551	.32	109.09	2.707
73.33777	.41005	−.10659	.42	104.57	2.713
73.33777	.50720	−.10641	.52	101.85	2.699
73.33953	.60839	−.10863	.62	100.12	2.715
73.33777	.70105	−.10959	.71	98.88	2.724
73.33777	.80488	−.11066	.81	97.83	2.736
73.33777	.91003	−.11174	.92	97.00	2.747
73.33777	1.00718	−.11075	1.01	96.28	2.747
73.33953	1.10836	−.11378	1.11	95.86	2.768
73.33777	1.20102	−.11474	1.21	95.46	2.784
73.33777	1.30486	−.11581	1.31	95.07	2.799
73.33777	1.41000	−.11689	1.41	94.74	2.813
73.33777	1.50716	−.11510	1.51	94.37	2.807
73.33953	1.60834	−.11893	1.61	94.23	2.790
73.33777	1.70100	−.11989	1.71	94.03	2.688
73.33777	1.80483	−.12096	1.81	93.83	2.508
73.33777	1.90997	−.12204	1.91	93.66	2.261
73.33777	2.00714	−.11944	2.01	93.41	1.908
73.33953	2.10831	−.12408	2.11	93.37	1.699
73.33777	2.20097	−.12504	2.20	93.25	1.496
73.33777	2.30480	−.12611	2.31	93.13	1.354
73.33777	2.40995	−.12719	2.41	93.02	1.231
73.33777	2.50713	−.12378	2.51	92.83	1.111
73.33953	2.60828	−.12923	2.61	92.84	1.054
73.33777	2.70095	−.13018	2.70	92.76	1.013
73.33777	2.80478	−.13126	2.81	92.68	.997
73.33777	2.90992	−.13234	2.91	92.60	.992
73.33777	3.00711	−.12813	3.01	92.44	.995
73.33953	3.10826	−.13438	3.11	92.48	.996
73.33777	3.20092	−.13533	3.20	92.42	.998
73.33777	3.30475	−.13640	3.31	92.36	.999
73.33777	3.40989	−.13749	3.41	92.31	.999
73.33777	3.51762	−.13860	3.52	92.26	.999
73.33777	3.62277	−.13968	3.63	92.21	.998
73.33777	3.70622	−.14054	3.71	92.17	.998
73.33777	3.81268	−.14163	3.82	92.13	.998
73.33777	4.01759	−.14375	4.02	92.05	.996
73.33777	4.12274	−.14483	4.13	92.01	.996
73.33777	4.20620	−.14569	4.21	91.98	.997
73.33777	4.31266	−.14678	4.32	91.95	.995
73.33777	4.51757	−.14889	4.52	91.89	.997

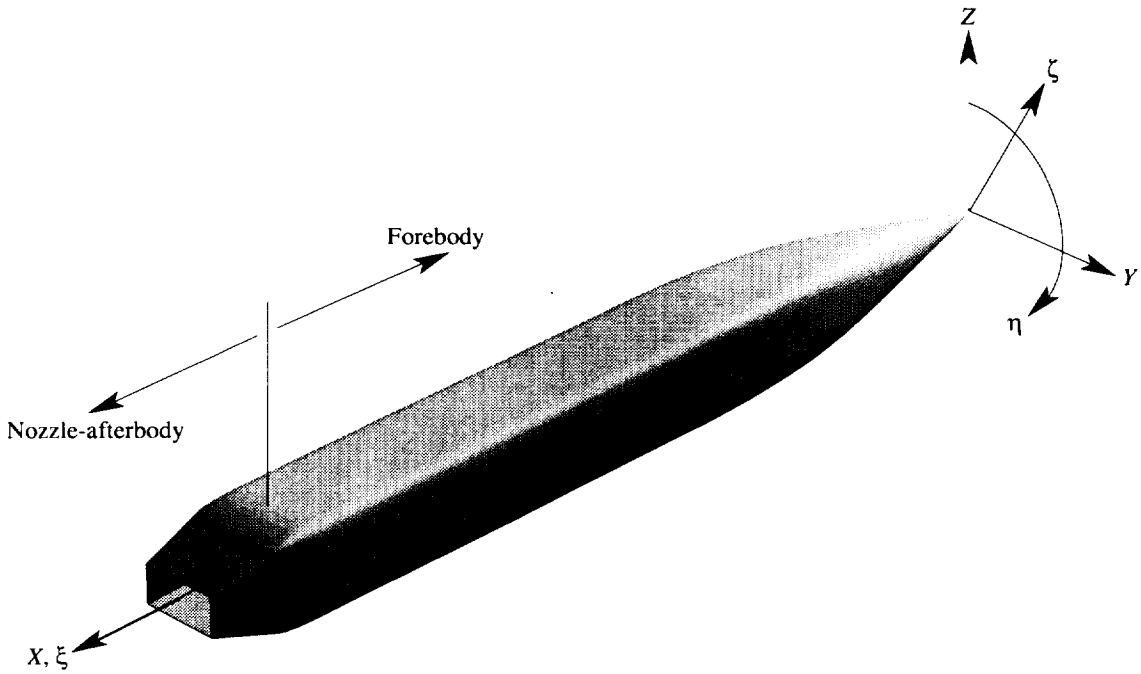

(a) Computational model and coordinate system.

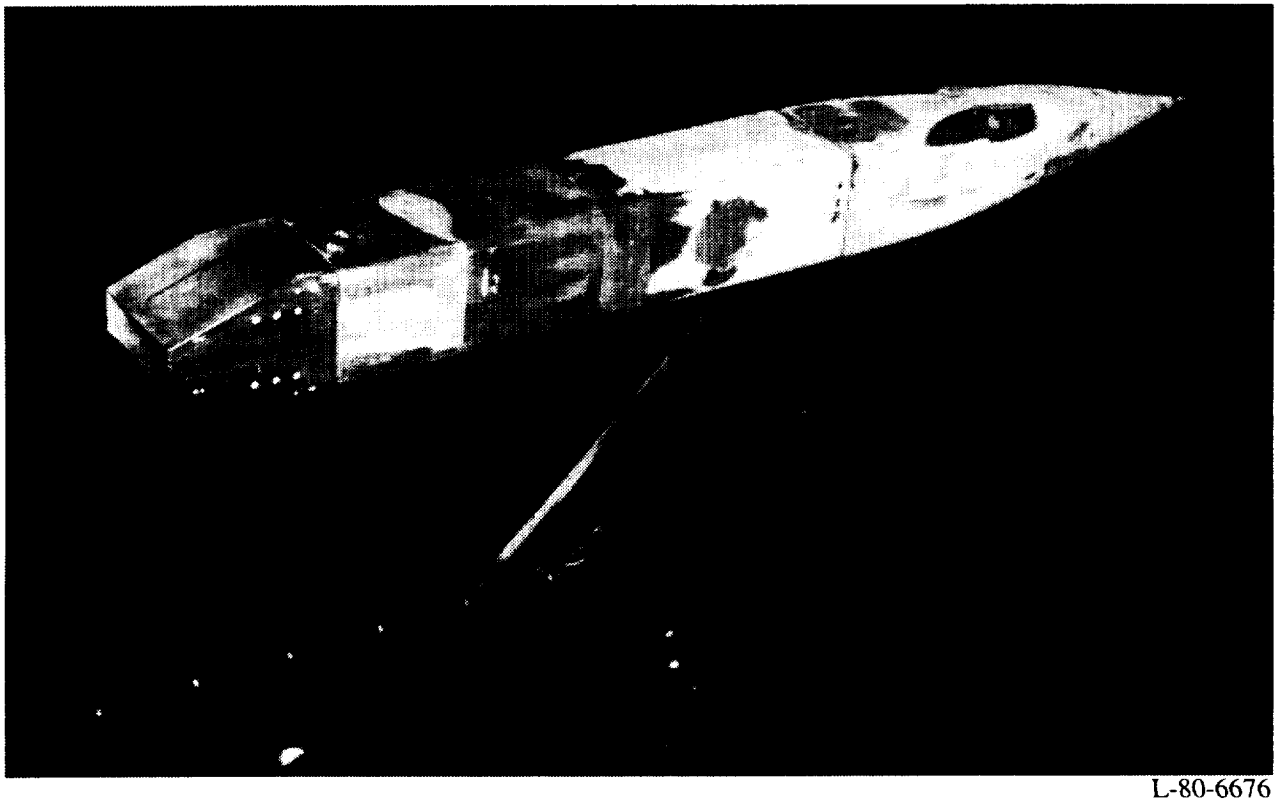

L-80-6676

(b) Experimental model installed in Langley 16-Foot Transonic Tunnel.

Figure 1. Computational and experimental models.

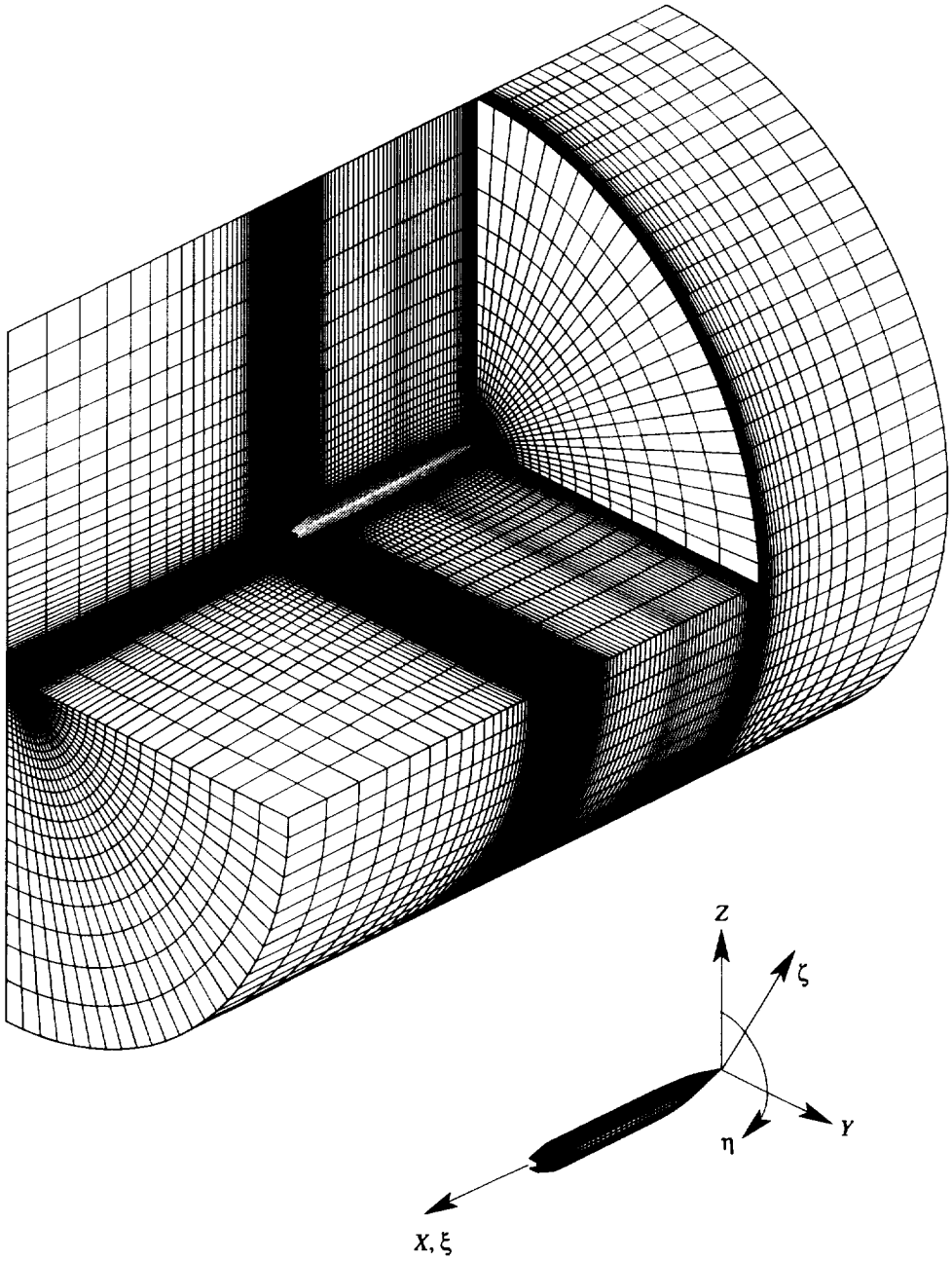

(a) Cutaway view of grid topology and coordinate system.

Figure 2. Details of computational region and grid.

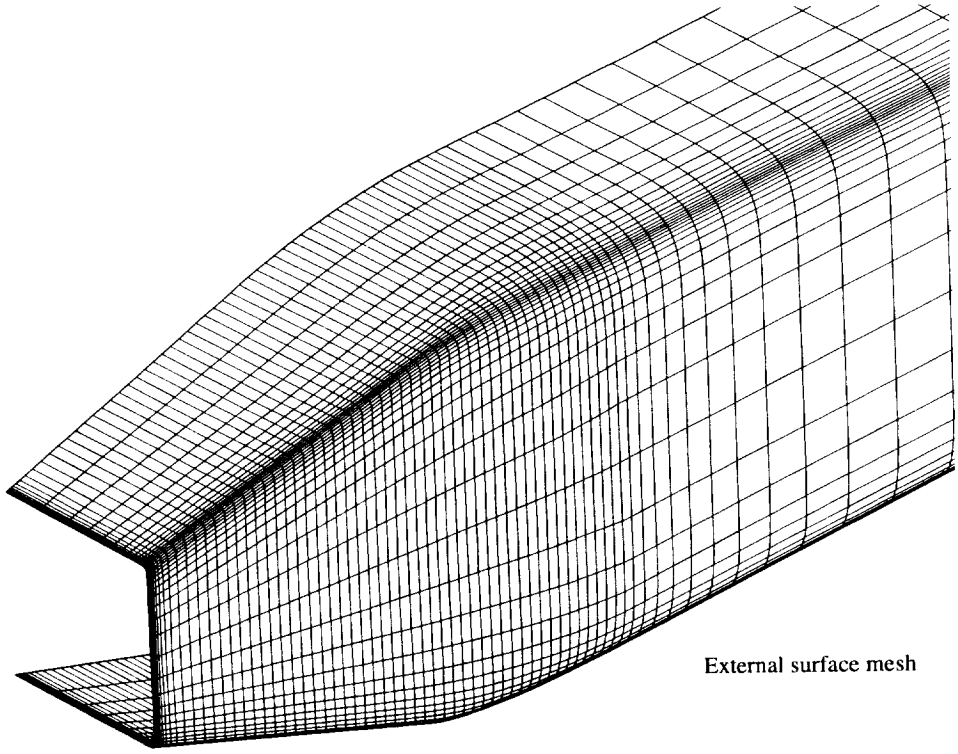

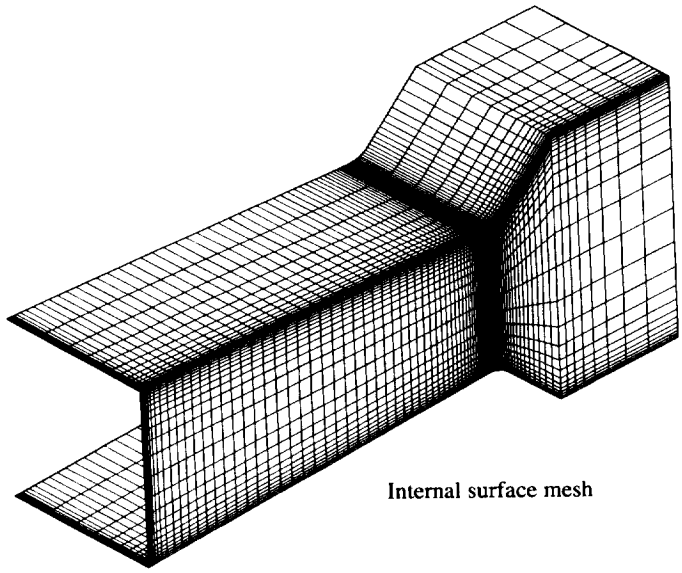

(b) Details of surface meshes in vicinity of nozzle-afterbody.

Figure 2. Continued.

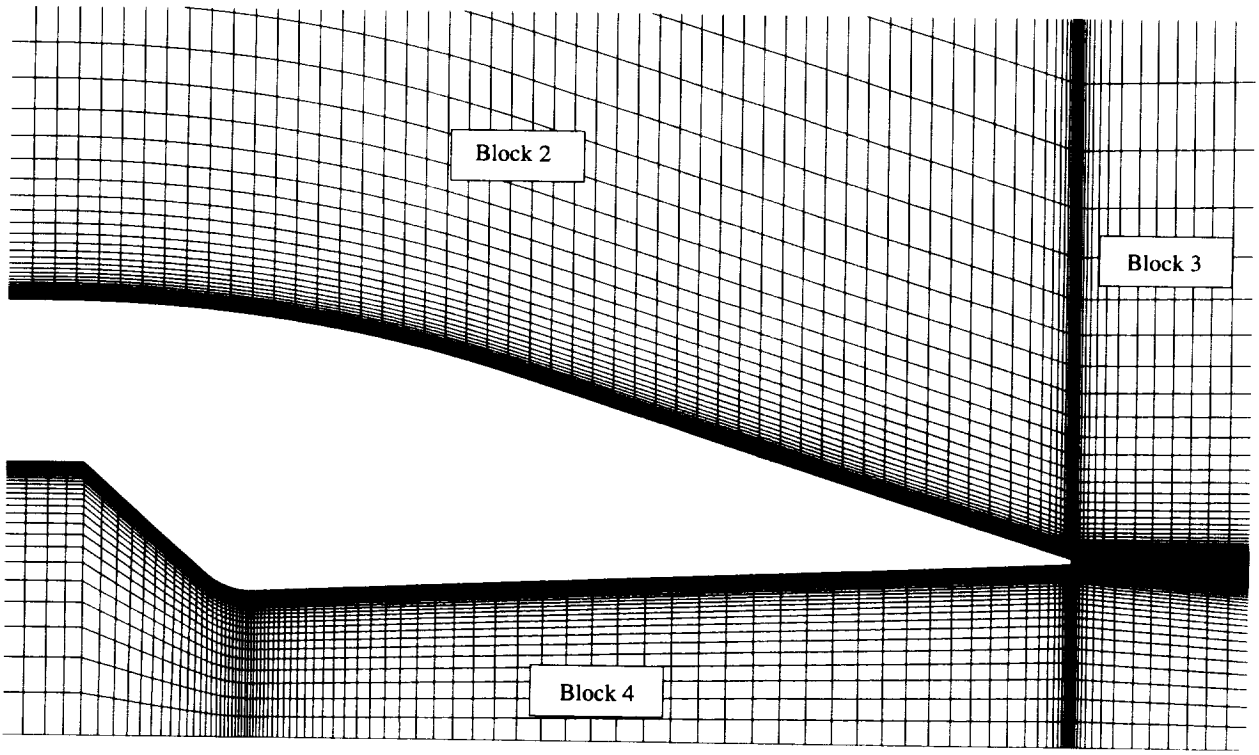

(c) Details of mesh in vertical plane of symmetry near nozzle-afterbody.

Figure 2. Concluded.

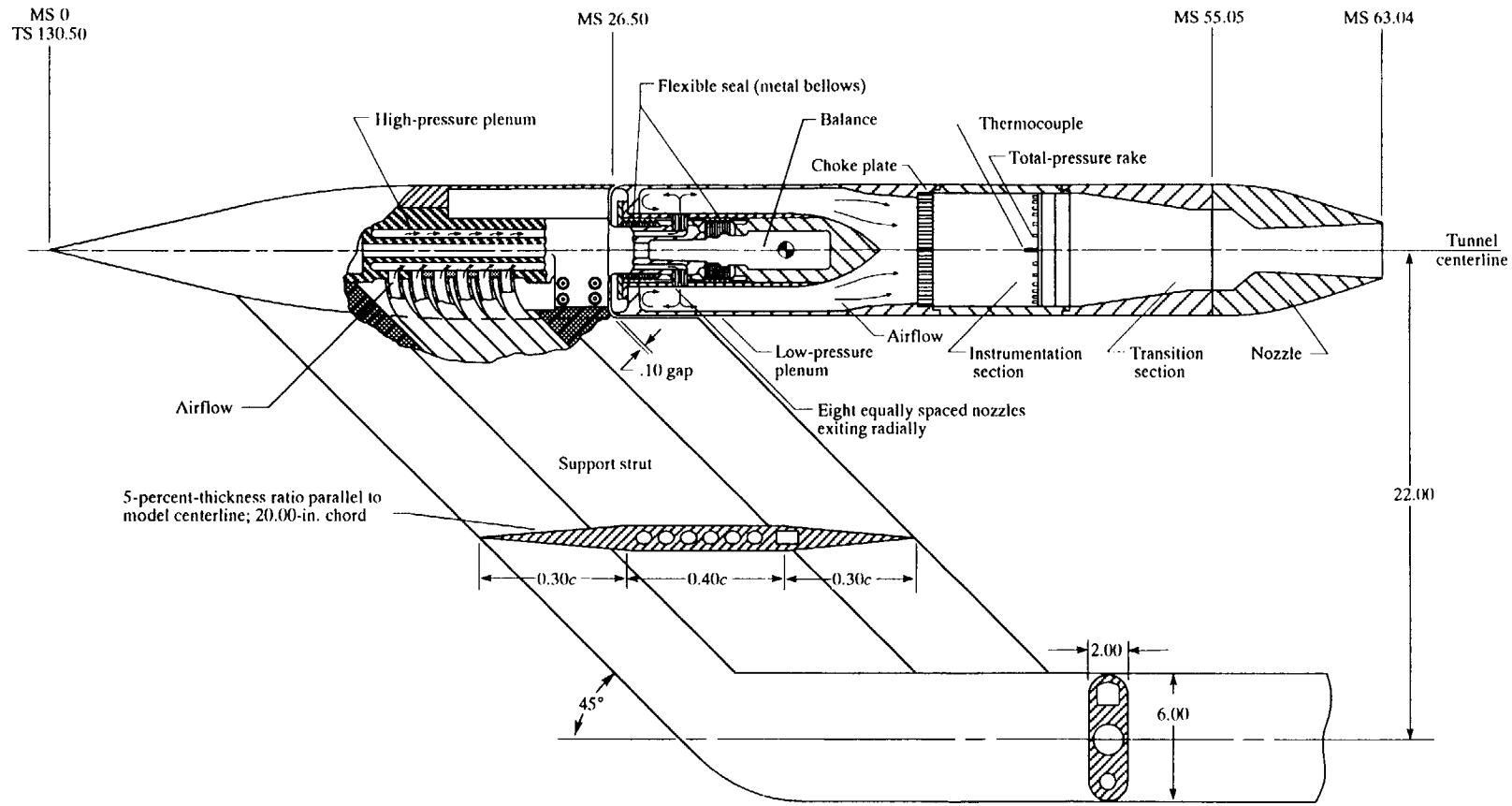

Figure 3. General arrangement of wind tunnel model and support system. All model linear dimensions and stations are in inches. Wind tunnel stations are in feet.

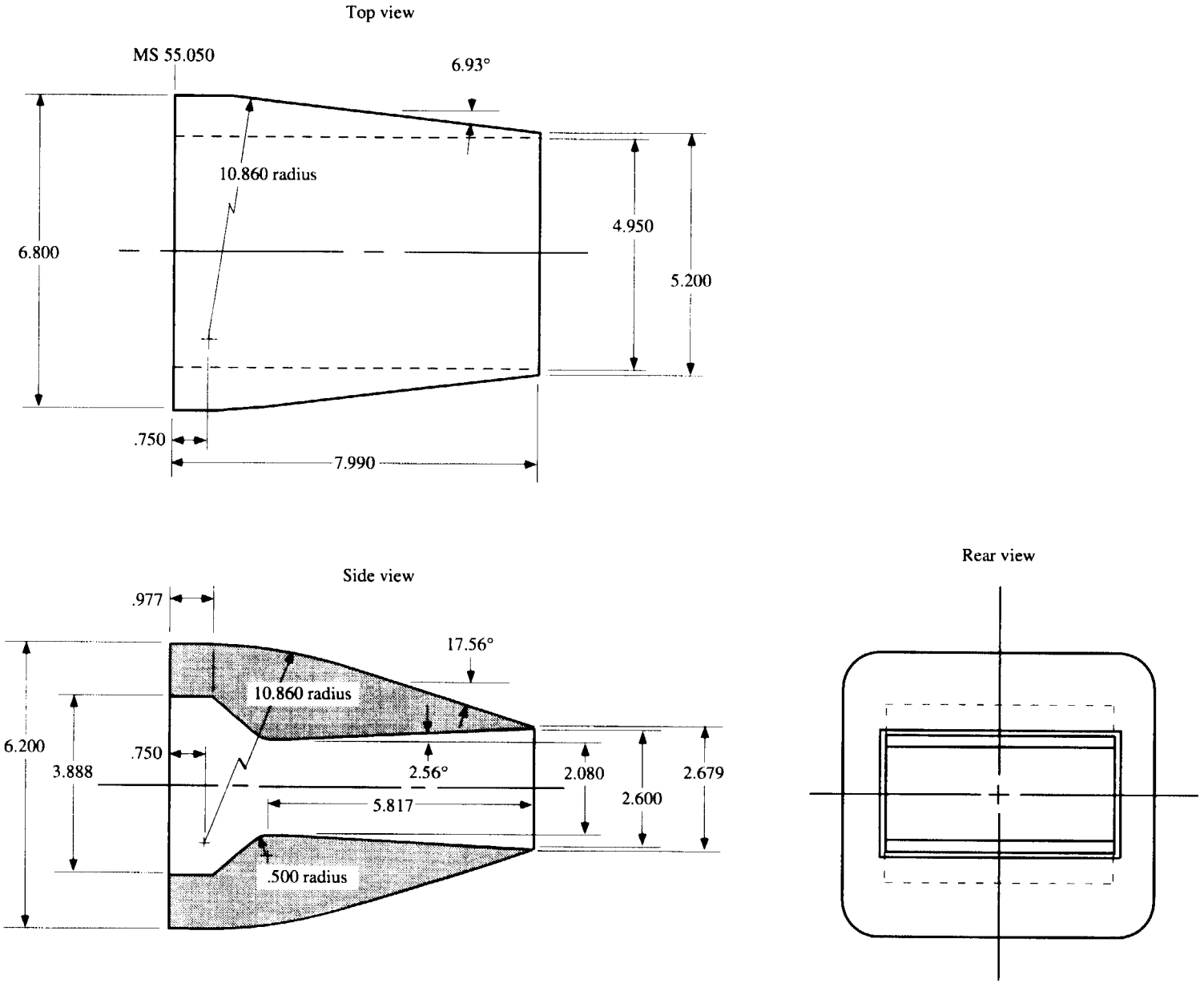

(a) Details of nozzle geometry. Linear dimensions are in inches.

Figure 4. Geometry of computational and experimental nozzle.

Typical cross section

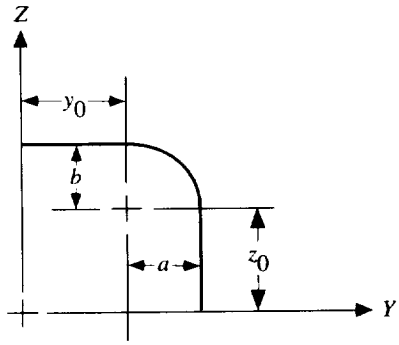

Nozzle external geometry parameter —					
x, in.	β	y_0, in.	a, in.	z_0, in.	b, in.
55.050000	9.000000	0.000000	3.400000	0.000000	3.100000
55.800000	9.000000	0.000000	3.400000	0.000000	3.100000
55.955000	8.971336	0.021620	3.377273	0.019712	3.079182
56.110000	8.885800	0.085850	3.309725	0.078265	3.017310
56.265000	8.744590	0.190812	3.199229	0.173926	2.916114
56.420000	8.550502	0.333435	3.048852	0.303860	2.778427
56.575000	8.306262	0.509542	2.862770	0.464213	2.608099
56.730000	8.016265	0.713960	2.646147	0.650215	2.409891
56.885000	7.685825	0.940668	2.404996	0.856320	2.189344
57.040000	7.321539	1.182966	2.146010	1.076359	1.952617
57.110255	7.147499	1.295949	2.024724	1.178869	1.841804
57.195000	6.923570	1.433990	1.873380	1.303889	1.706142
57.350000	6.459978	1.687944	1.603588	1.532708	1.456110
57.505000	5.932959	1.937487	1.335207	1.755519	1.209805
57.660000	5.351886	2.175169	1.078687	1.965047	0.974486
57.815000	4.728499	2.393870	0.841148	2.154417	0.757011
57.970000	4.078337	2.586997	0.629184	2.317381	0.563611
58.125000	3.424089	2.748665	0.448678	2.448520	0.399683
58.280000	2.803543	2.873865	0.304640	2.543429	0.269612
58.435000	2.287444	2.958598	0.201069	2.598861	0.176621
58.590000	2.006571	2.999990	0.140839	2.612835	0.122664
58.719355	2.000000	3.000108	0.125000	2.592250	0.108007
58.745000	2.000000	2.996991	0.125000	2.585239	0.107826
58.900000	2.000000	2.978153	0.125000	2.541479	0.106672
59.055000	2.000000	2.959315	0.125000	2.495322	0.105401
59.076861	2.000000	2.956659	0.125000	2.488617	0.105212
59.210000	2.000000	2.940478	0.125000	2.447643	0.104050
59.365000	2.000000	2.921640	0.125000	2.399957	0.102680
59.520000	2.000000	2.902802	0.125000	2.352287	0.101294
59.675000	2.000000	2.883964	0.125000	2.304635	0.099890
59.830000	2.000000	2.865126	0.125000	2.257001	0.098469
59.985000	2.000000	2.846288	0.125000	2.209385	0.097029
60.140000	2.000000	2.827450	0.125000	2.161787	0.095571
60.295000	2.000000	2.808613	0.125000	2.114208	0.094095
60.450000	2.000000	2.789755	0.125000	2.066648	0.092599
60.605000	2.000000	2.770937	0.125000	2.019108	0.091084
60.760000	2.000000	2.752099	0.125000	1.971587	0.089549
60.915000	2.000000	2.733261	0.125000	1.924087	0.087994
61.070000	2.000000	2.714423	0.125000	1.876607	0.086418
61.225000	2.000000	2.695585	0.125000	1.829148	0.084821
61.380000	2.000000	2.676747	0.125000	1.781711	0.083203
61.535000	2.000000	2.657910	0.125000	1.734295	0.081563
61.690000	2.000000	2.639072	0.125000	1.686902	0.079900
61.845000	2.000000	2.620234	0.125000	1.639532	0.078215
62.000000	2.000000	2.601396	0.125000	1.592185	0.076506
62.155000	2.000000	2.582558	0.125000	1.544826	0.074774
62.310000	2.000000	2.563720	0.125000	1.497563	0.073017
62.465000	2.000000	2.544882	0.125000	1.450289	0.071236
62.620000	2.000000	2.526045	0.125000	1.403040	0.069425
62.775000	2.000000	2.507207	0.125000	1.355817	0.067596
62.930000	2.000000	2.488369	0.125000	1.308621	0.065737
63.040000	2.000000	2.475000	0.125000	1.275143	0.064401

(b) Details of external cross sections.

Figure 4. Concluded.

Row	x, in.	y, in.	z, in.
1	55.18000	0	3.10000
1	55.80000	0	3.10000
1	57.04000	0	3.02898
1	57.66000	0	2.93958
1	58.28000	0	2.81304
1	58.90000	0	2.64815
1	59.52000	0	2.45358
1	60.14000	0	2.25736
1	61.38000	0	1.86491
1	62.62000	0	1.47246
1	Base		
2	55.80000	1.70000	3.09933
2	57.04000	1.66400	3.02897
2	58.28000	1.58900	2.81304
2	59.52000	1.51400	2.45358
2	61.38000	1.40100	1.86491
3	55.80000	3.18763	2.83000
3	56.42000	3.18233	2.82800
3	57.04000	3.16545	2.82200
3	58.28000	3.12765	2.73800
3	59.52000	3.00800	2.40700
3	61.38000	2.79131	1.81500
3	62.62000	2.64577	1.42300
3	Base		
4	57.04000	3.32897	1.51400
4	58.28000	3.17851	1.40700
4	59.52000	3.02780	1.22700
4	61.38000	2.80175	0.93200
5	55.18000	3.40000	0
5	55.80000	3.40000	0
5	56.42000	3.38229	0
5	57.04000	3.32898	0
5	58.28000	3.17851	0
5	59.52000	3.02780	0
5	61.38000	2.80175	0
5	62.62000	2.65104	0
5	Base		

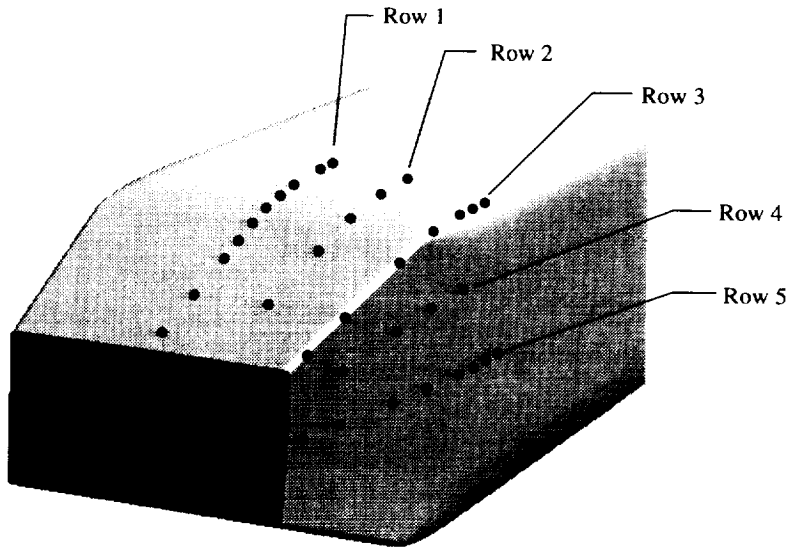

(a) External surface.

Figure 5. Orifice locations for experimental model.

Row	x, in.	y, in.	z, in.
6	55.80000	0	1.94400
6	56.73000	0	1.31107
6	57.22300	0	1.04000
6	58.28000	0	1.08683
6	60.14000	0	1.17013
6	62.62000	0	1.28119
7	58.28000	1.23700	1.08683
7	60.14000	1.23700	1.17013
7	62.62000	1.23700	1.28119
8	57.22300	2.37500	1.04000
8	58.28000	2.37500	1.08683
8	60.14000	2.37500	1.17013
8	62.62000	2.37500	1.28119
9	57.22300	2.47500	0
9	58.28000	2.47500	0
9	60.14000	2.47500	0
9	62.62000	2.75000	0

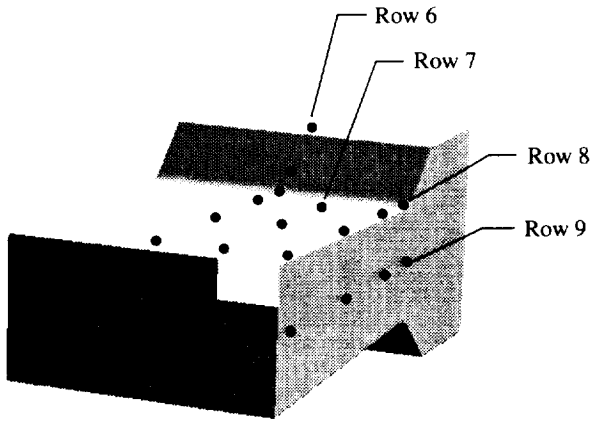

(b) Internal surface.

Figure 5. Concluded.

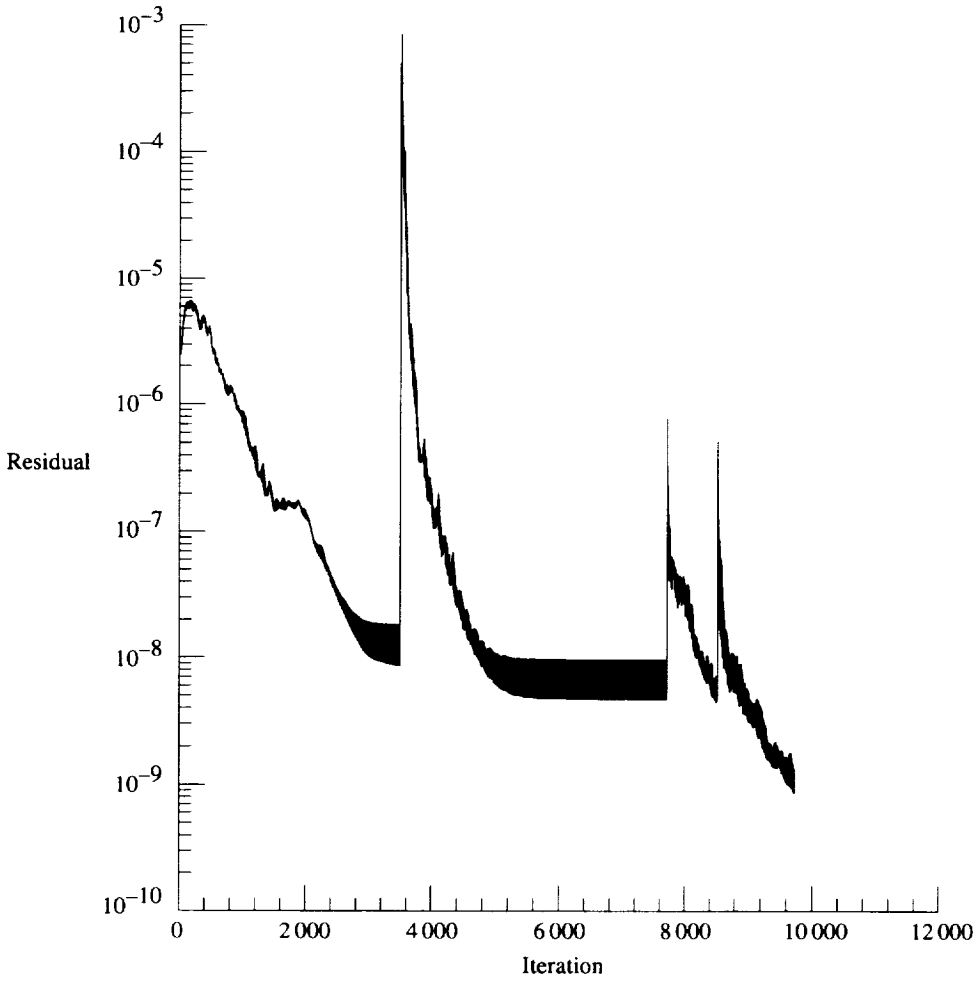

Figure 6. Typical convergence history. $M_\infty = 0.938$; NPR = 4.017; and Jones-Launder k-ε turbulence model.

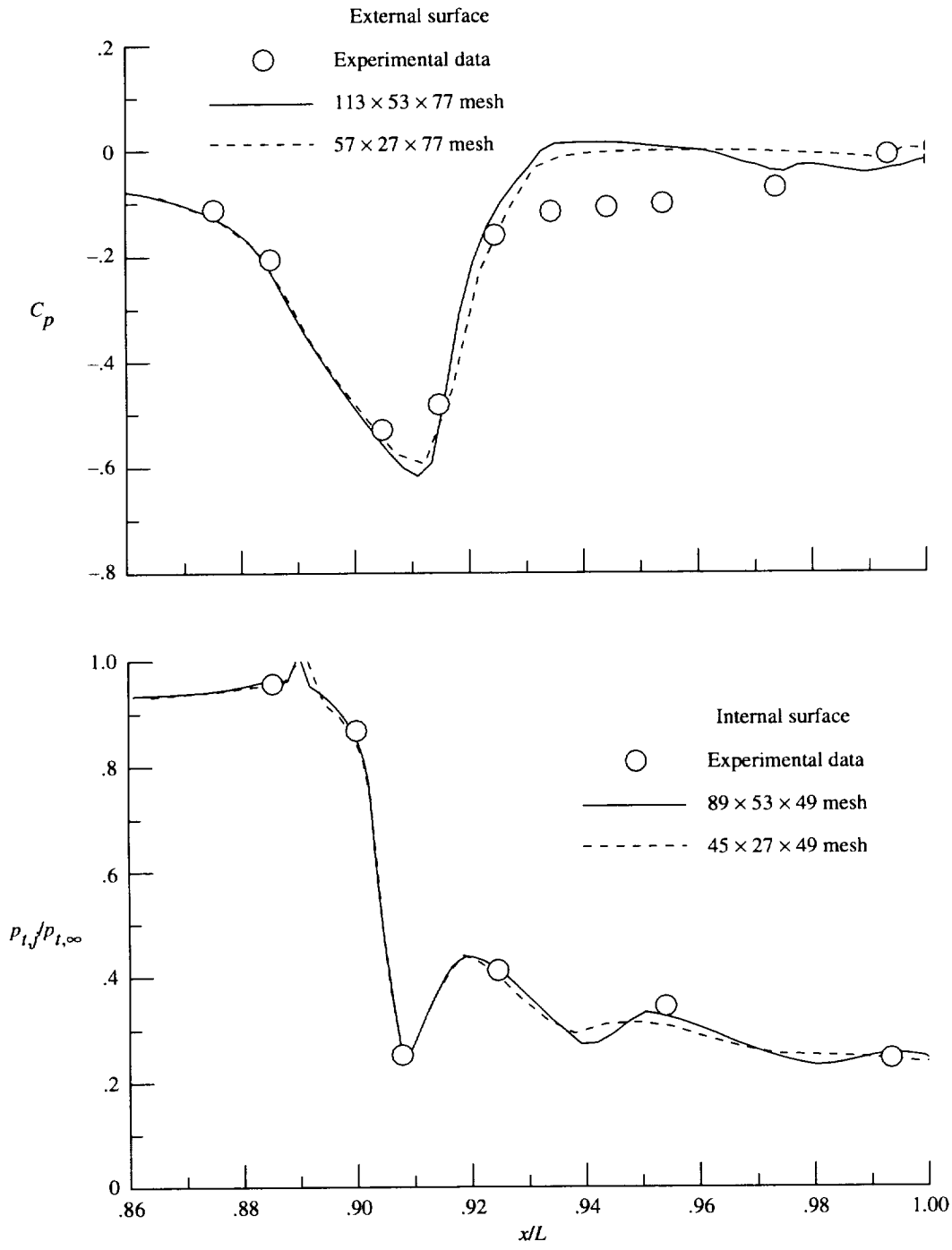

(a) Effect on surface pressures.

Figure 7. Effect of mesh density on solution. M_∞ = 0.938; NPR = 4.017; Baldwin-Lomax turbulence model; and top row.

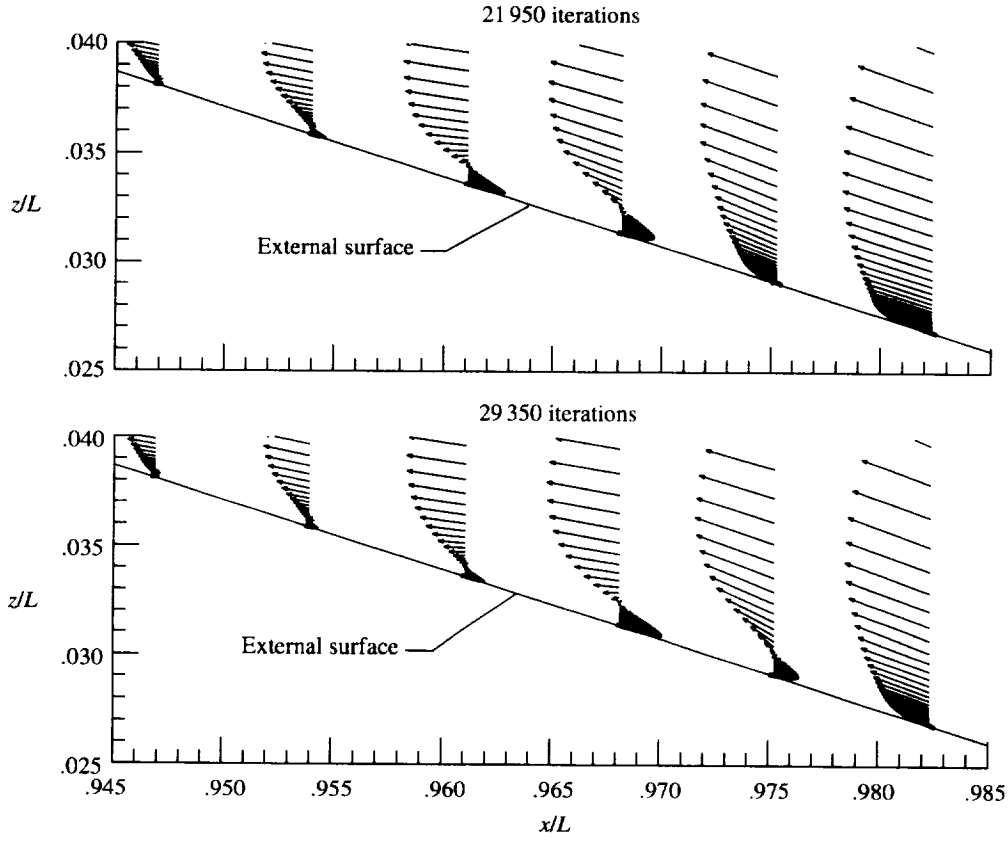

(b) Velocity vectors for 113 × 53 × 77 mesh.

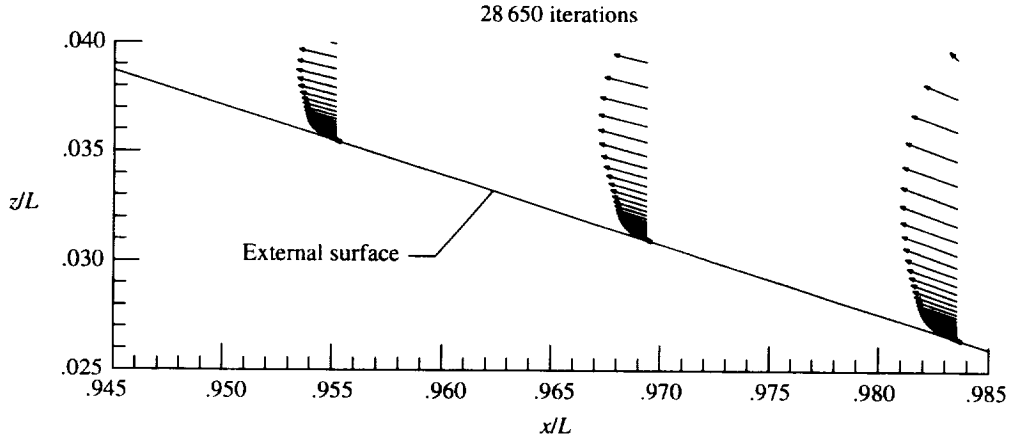

(c) Velocity vectors for 53 × 27 × 77 mesh.

Figure 7. Concluded.

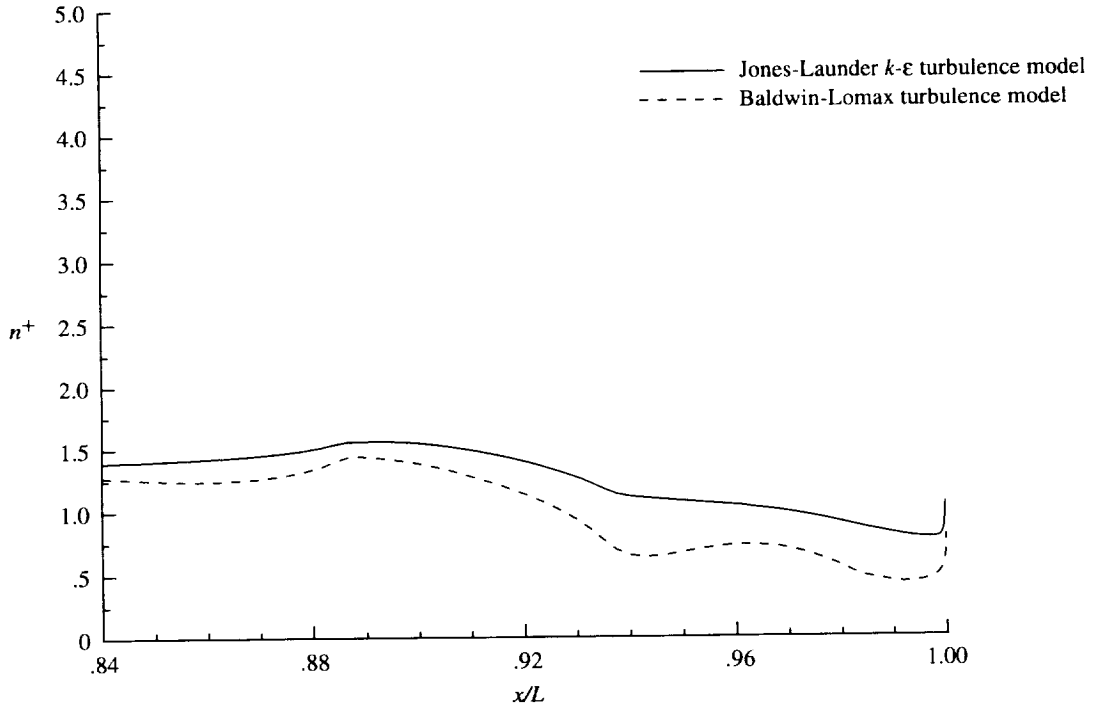

(a) $M_\infty = 0.600$; NPR = 4.003; and row 1 (external surface).

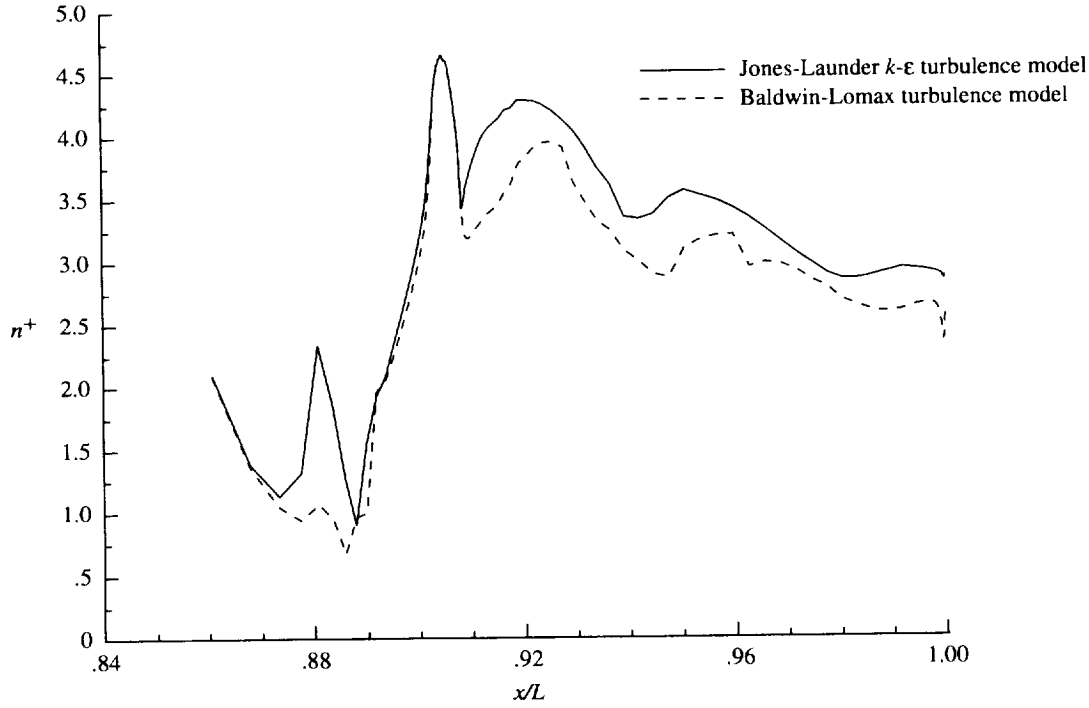

(b) $M_\infty = 0.600$; NPR = 4.003; and row 6 (internal surface).

Figure 8. The n^+ distributions for top row of nozzle-afterbody.

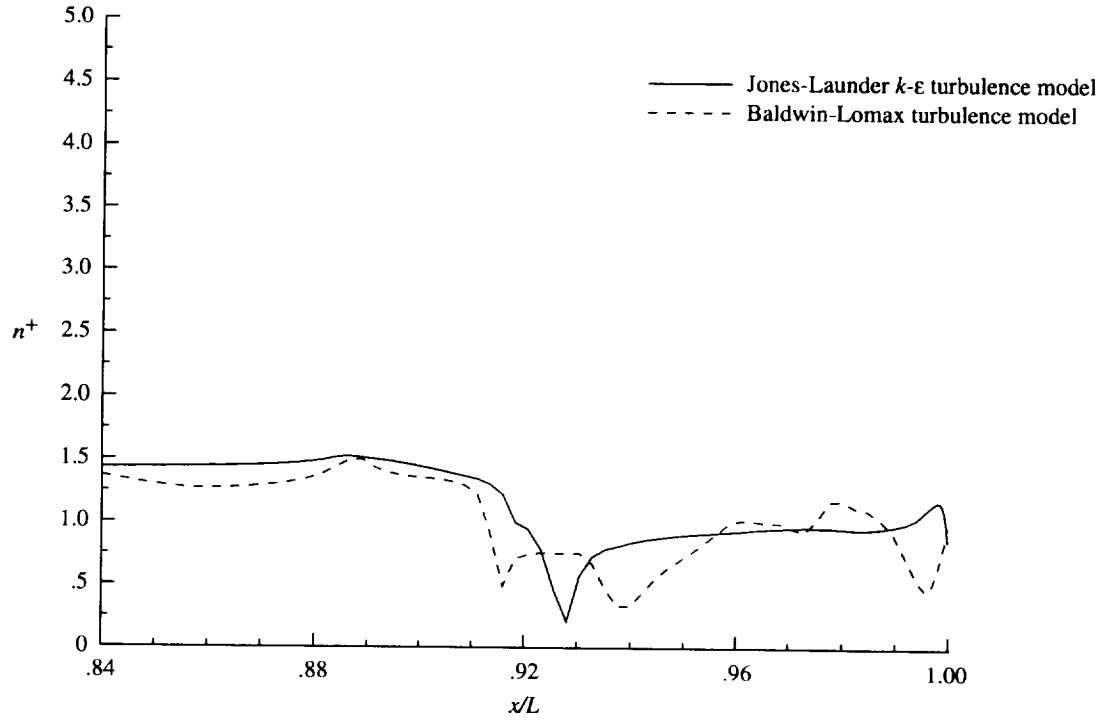

(c) $M_\infty = 0.938$; NPR = 4.017; and row 1 (external surface).

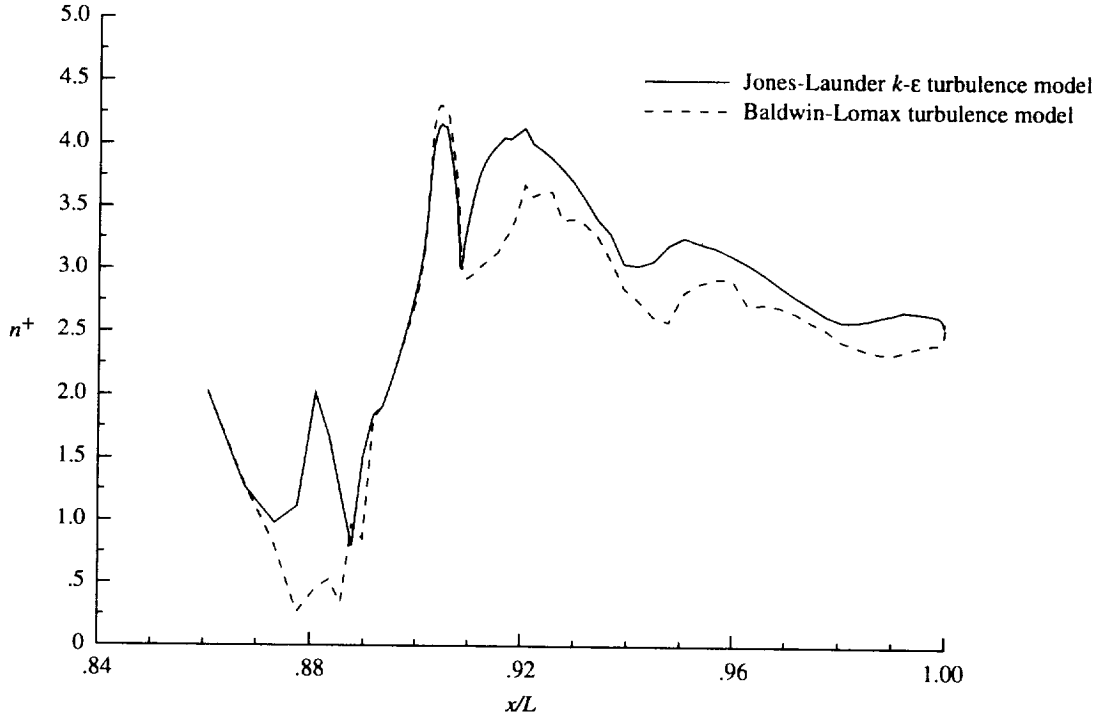

(d) $M_\infty = 0.938$; NPR = 4.017; and row 6 (internal surface).

Figure 8. Concluded.

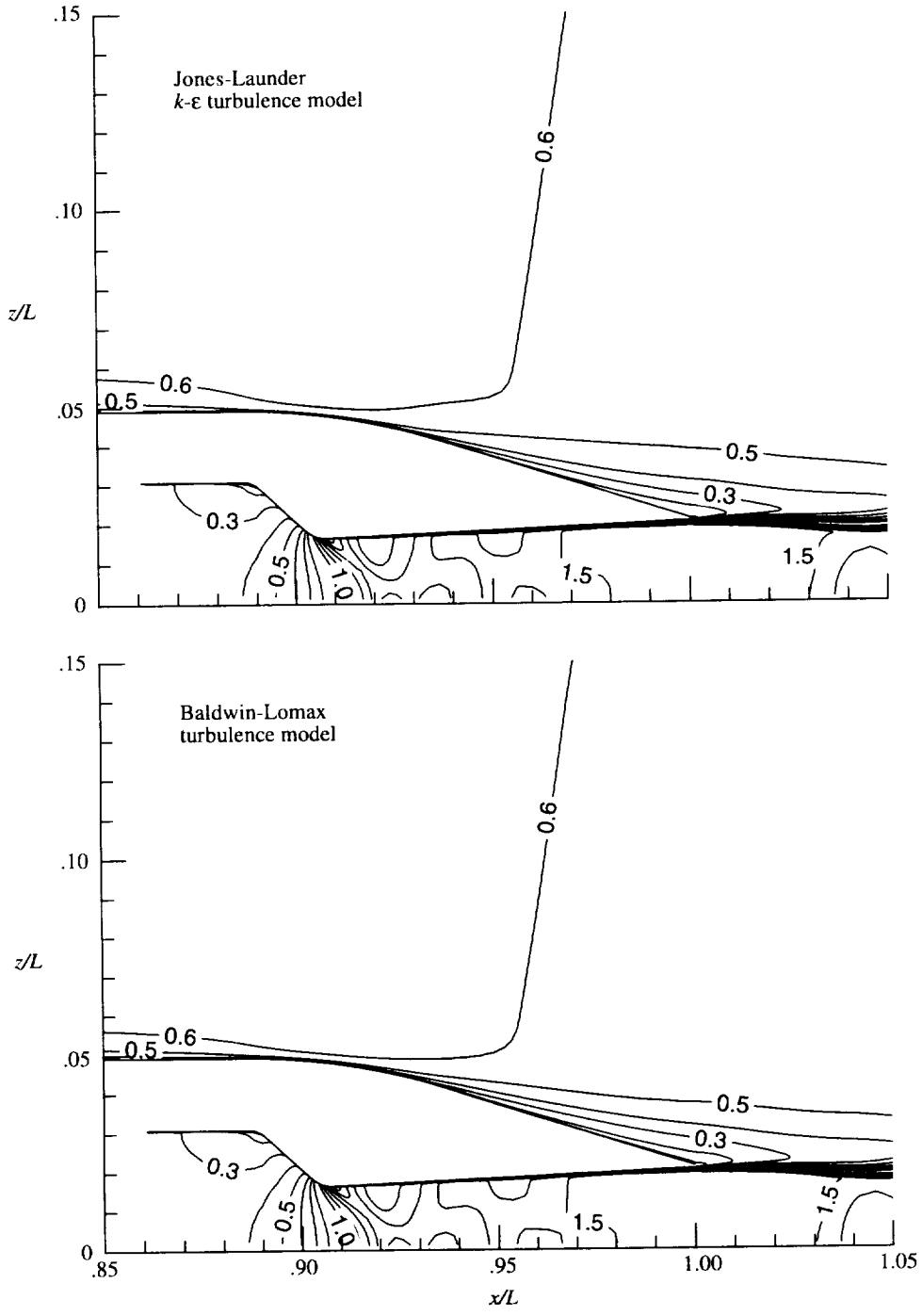

(a) Vertical plane of symmetry.

Figure 9. Mach number contours. M_∞ = 0.600; NPR = 4.003; and contour increment = 0.1.

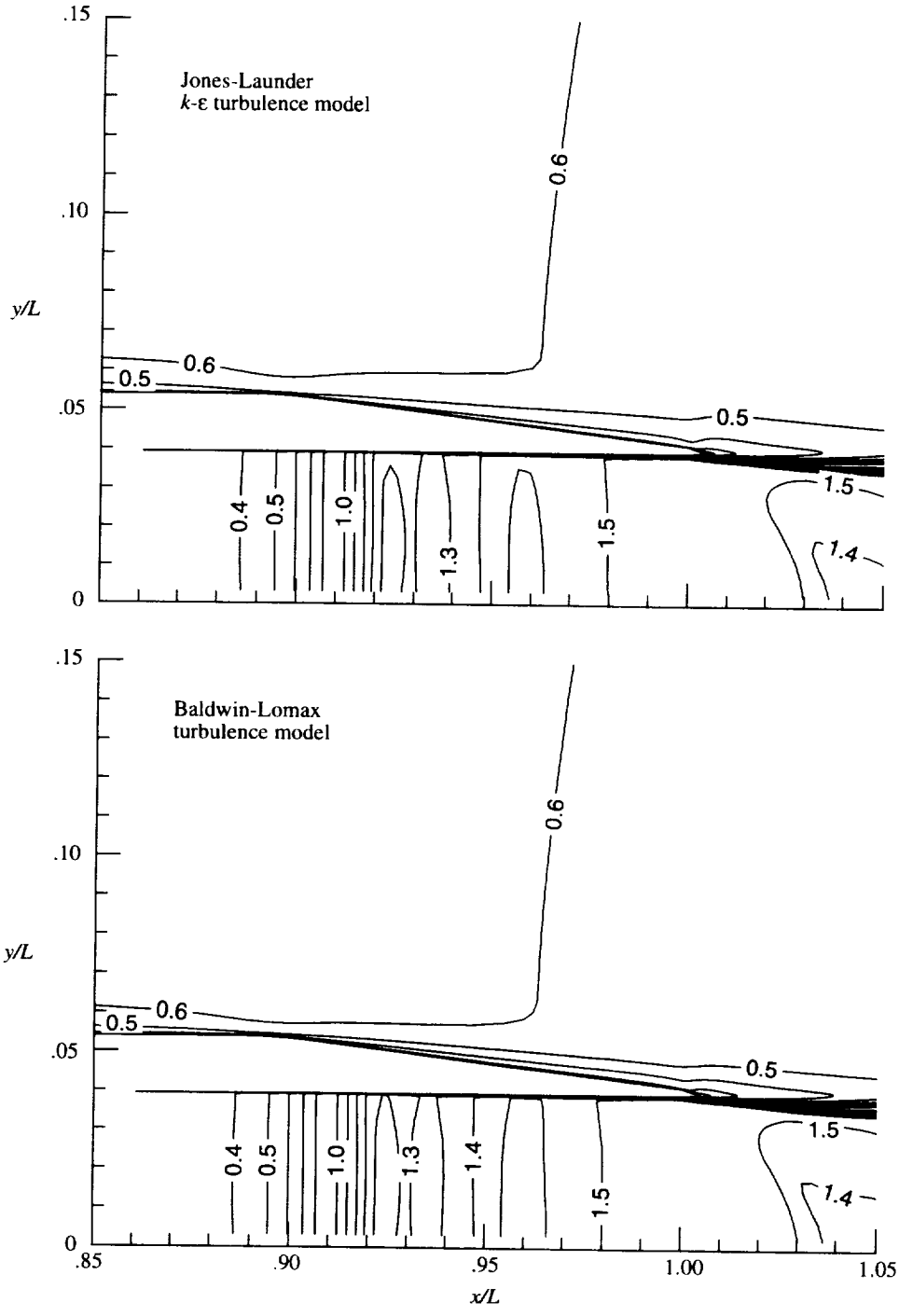

(b) Horizontal plane of symmetry.

Figure 9. Concluded.

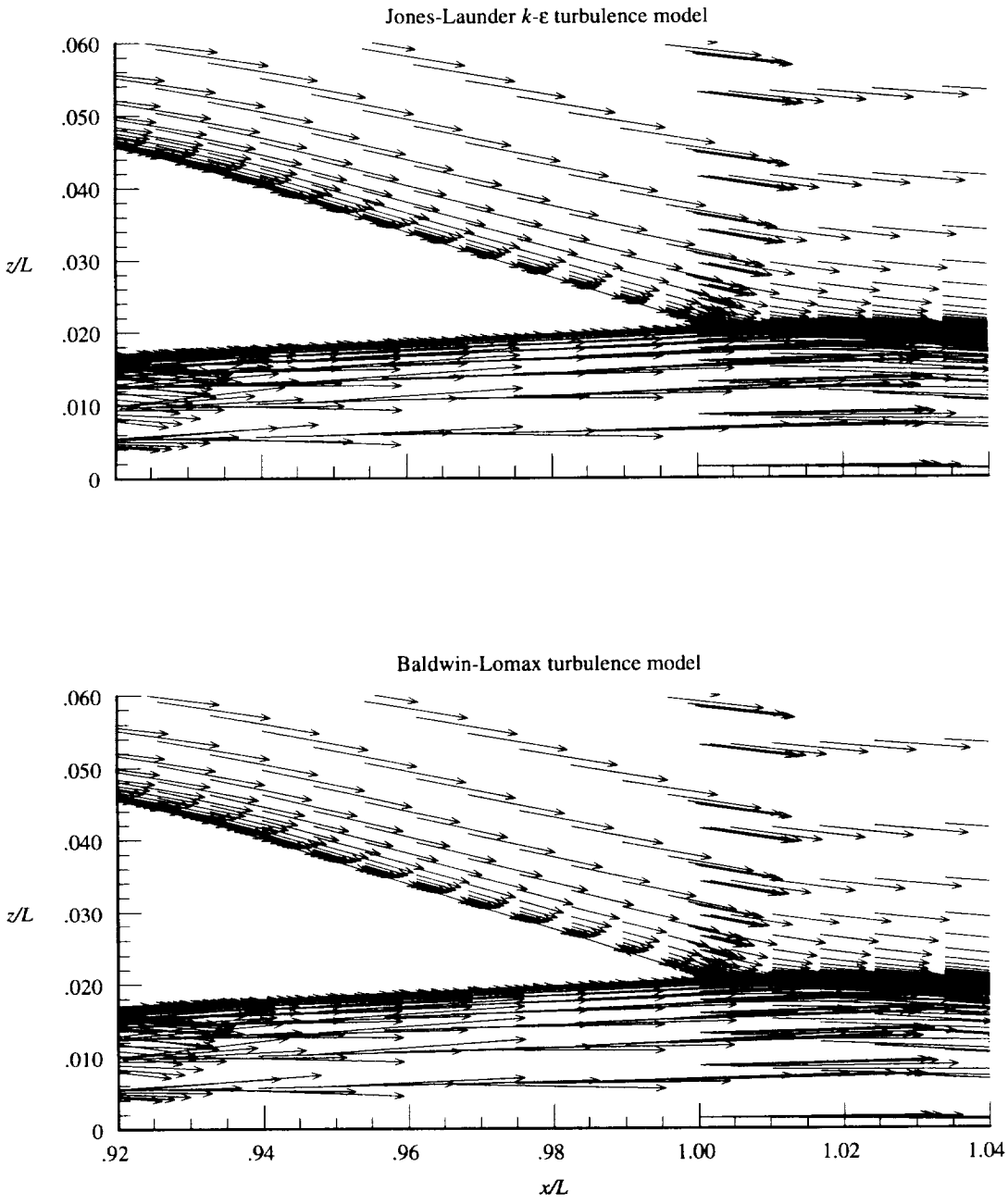

(a) Vertical plane of symmetry.

Figure 10. Velocity vectors. M_∞ = 0.600; NPR = 4.003. (Most vectors not shown for clarity.)

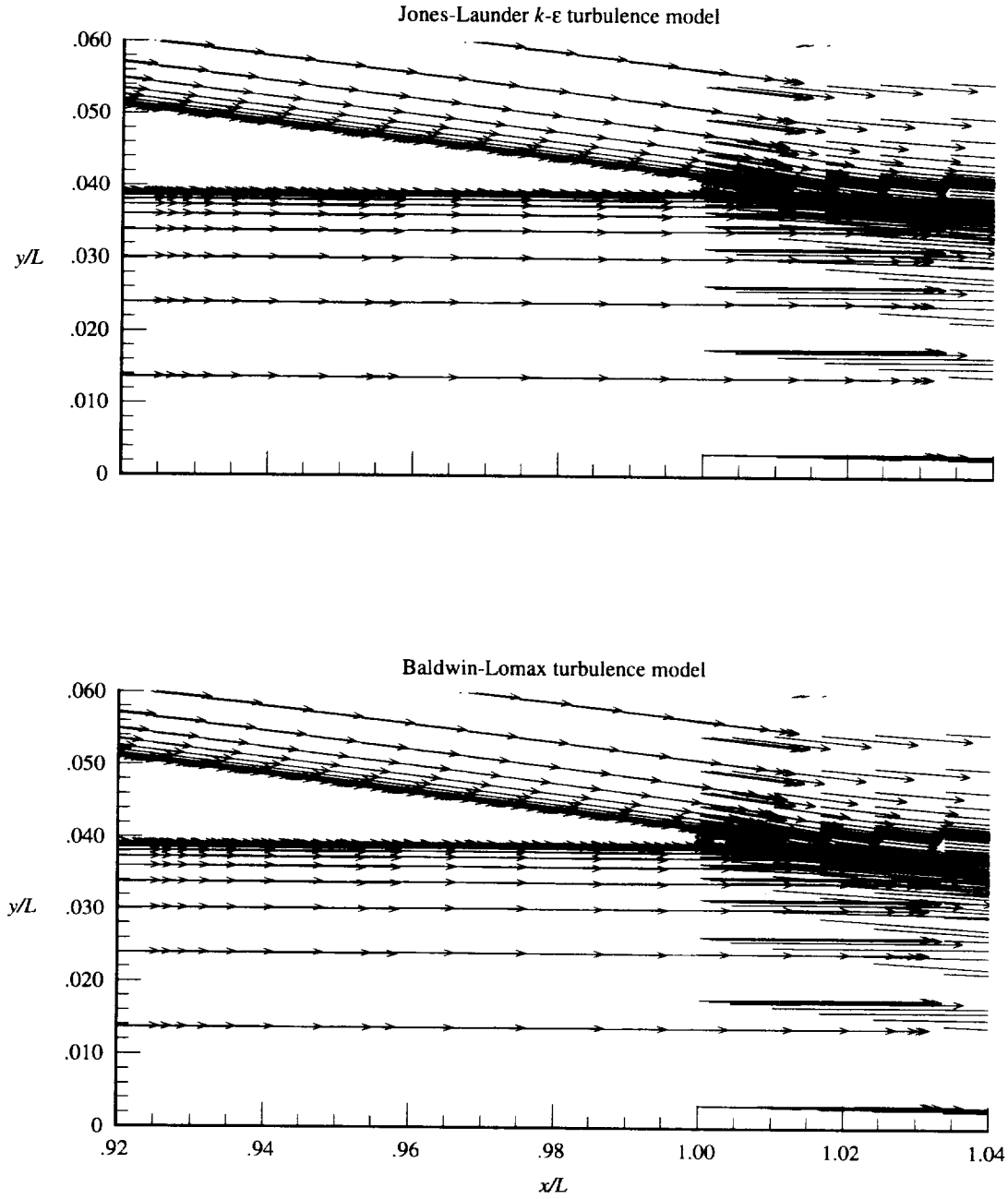

(b) Horizontal plane of symmetry.

Figure 10. Concluded.

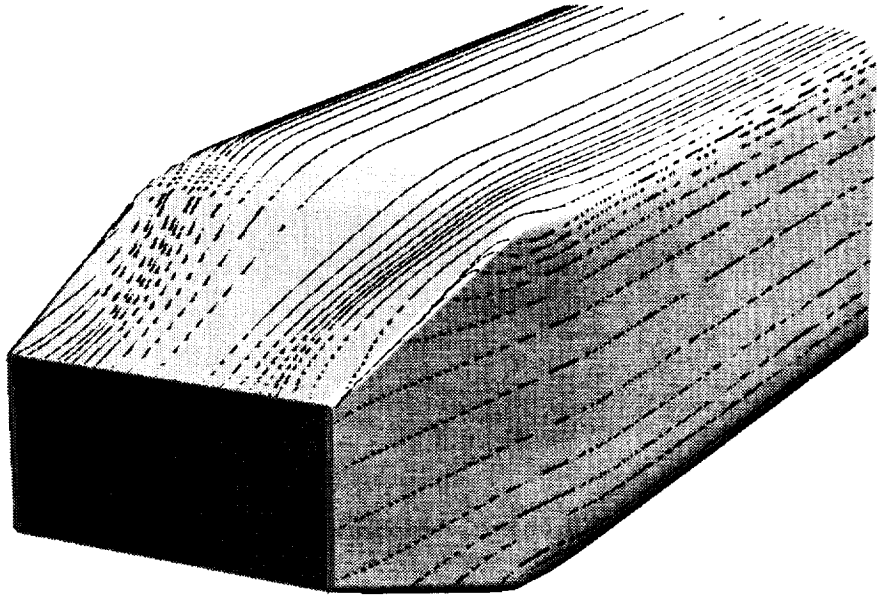

Jones-Launder k-ε turbulence model

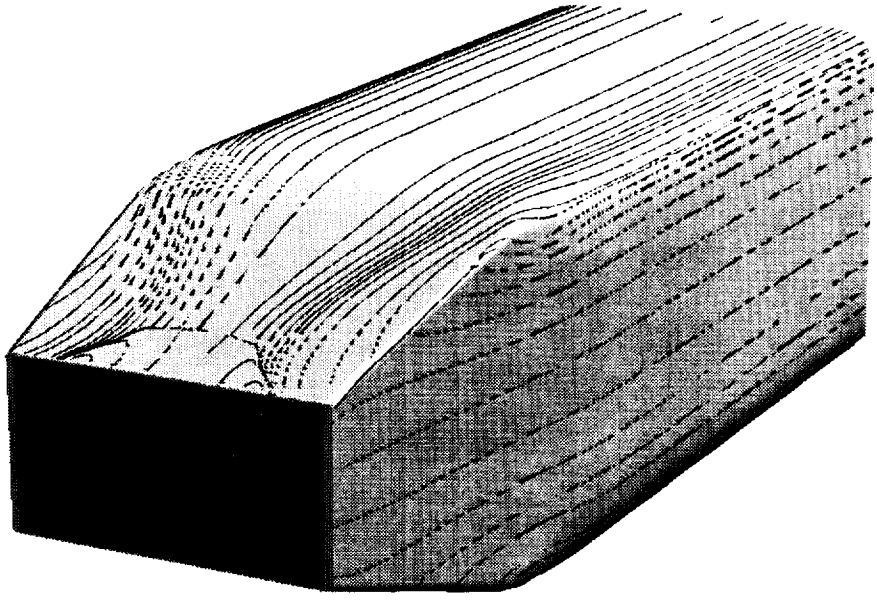

Baldwin-Lomax turbulence model

(a) External surface.

Figure 11. Computed oil flows (particle traces) on nozzle-afterbody surfaces. $M_\infty = 0.600$ and NPR = 4.003.

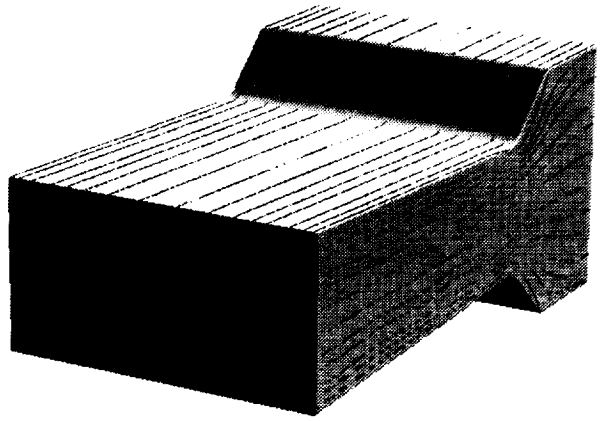

Jones-Launder k-ε turbulence model

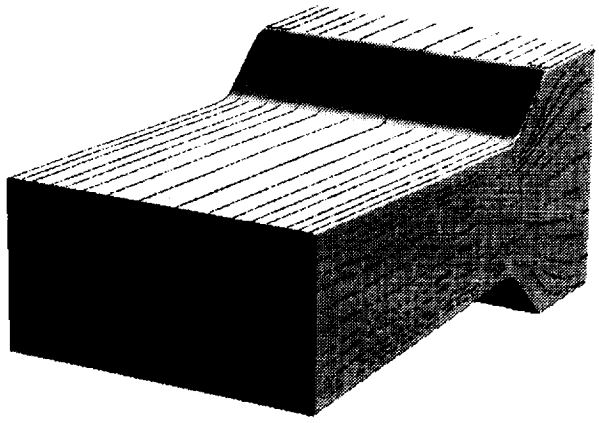

Baldwin-Lomax turbulence model

(b) Internal nozzle surface.

Figure 11. Concluded.

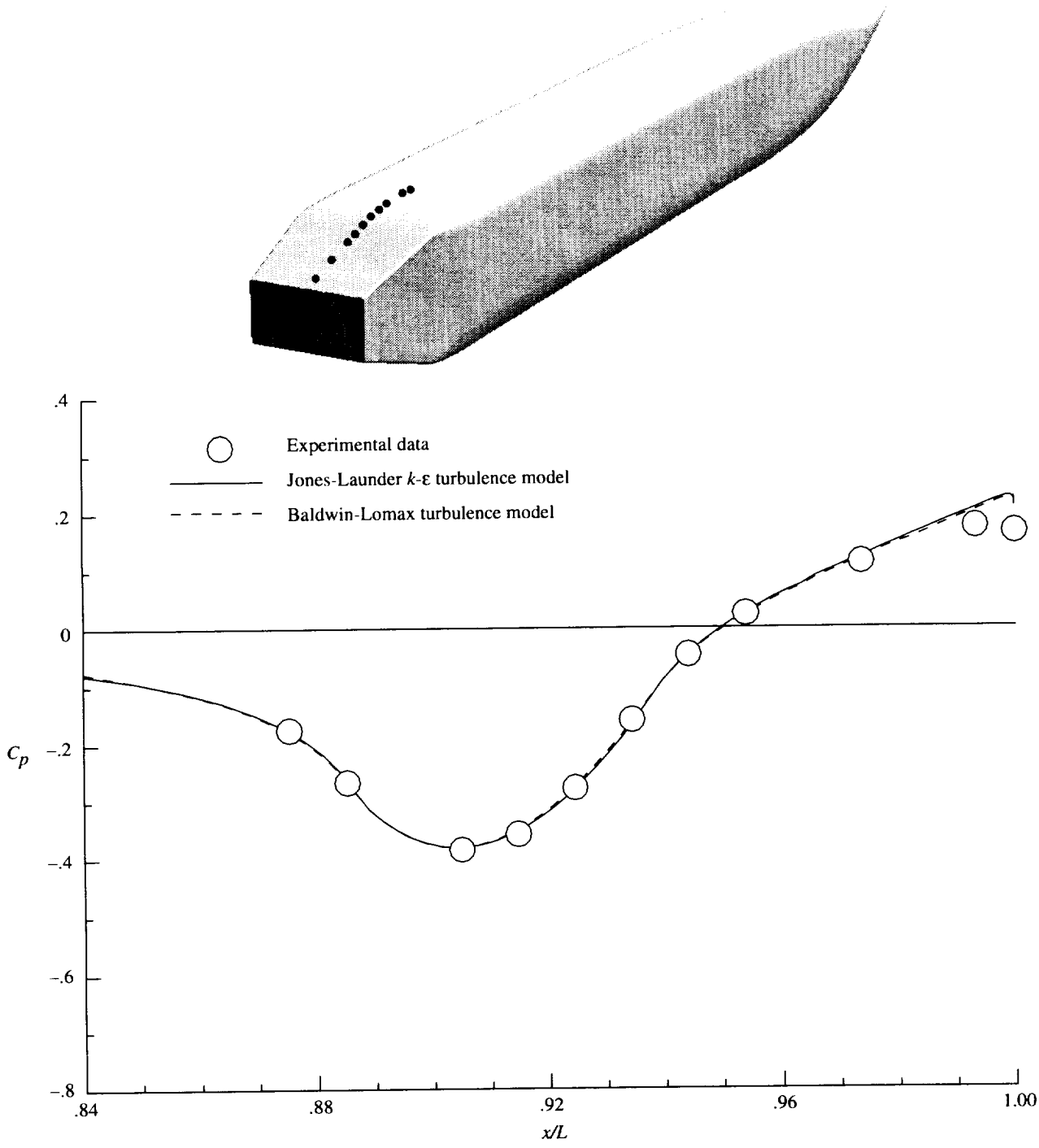

(a) $M_\infty = 0.600$; NPR = 4.003; and row 1.

Figure 12. External pressure coefficient distributions.

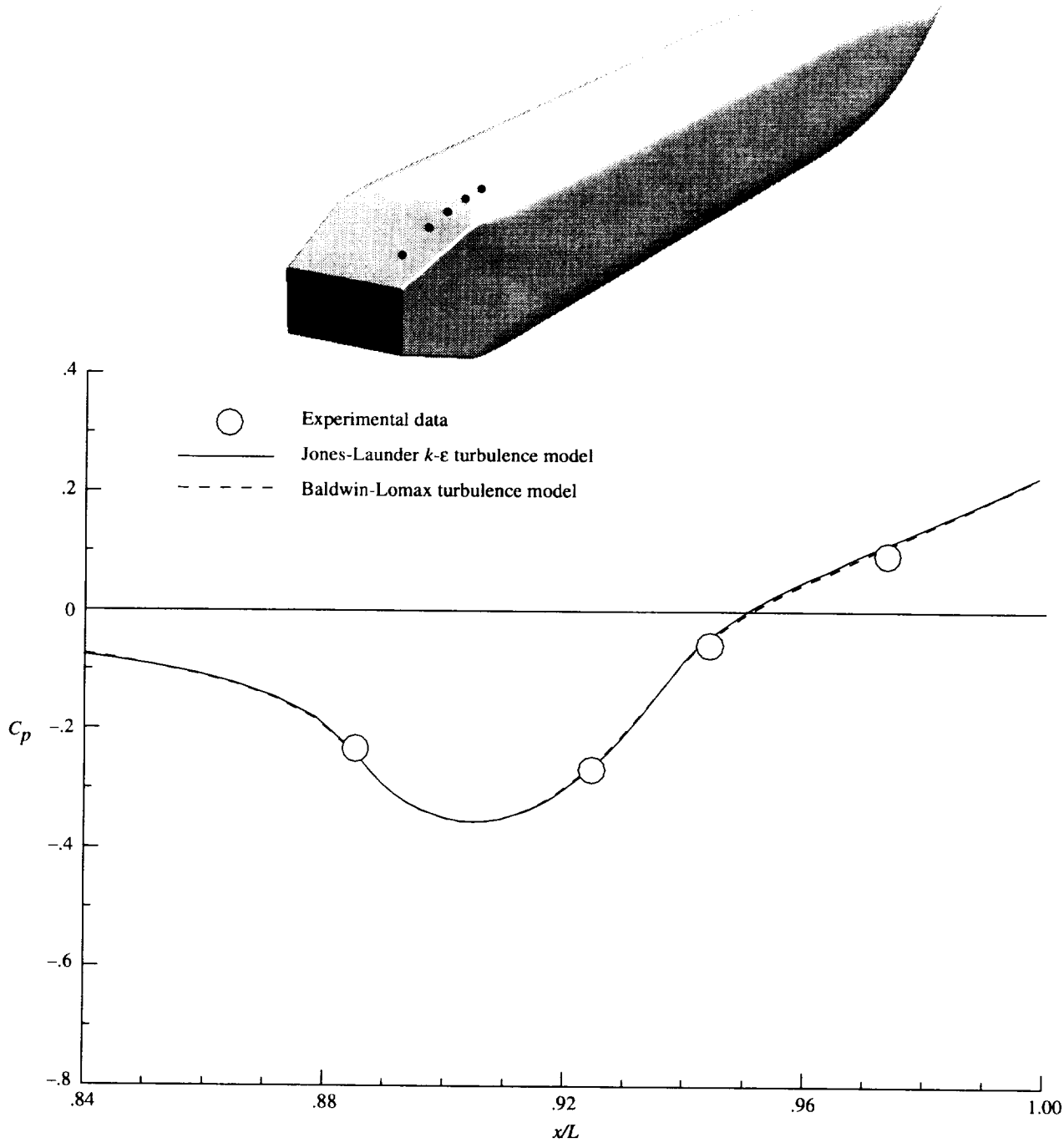

(b) $M_\infty = 0.600$; NPR = 4.003; and row 2.

Figure 12. Continued.

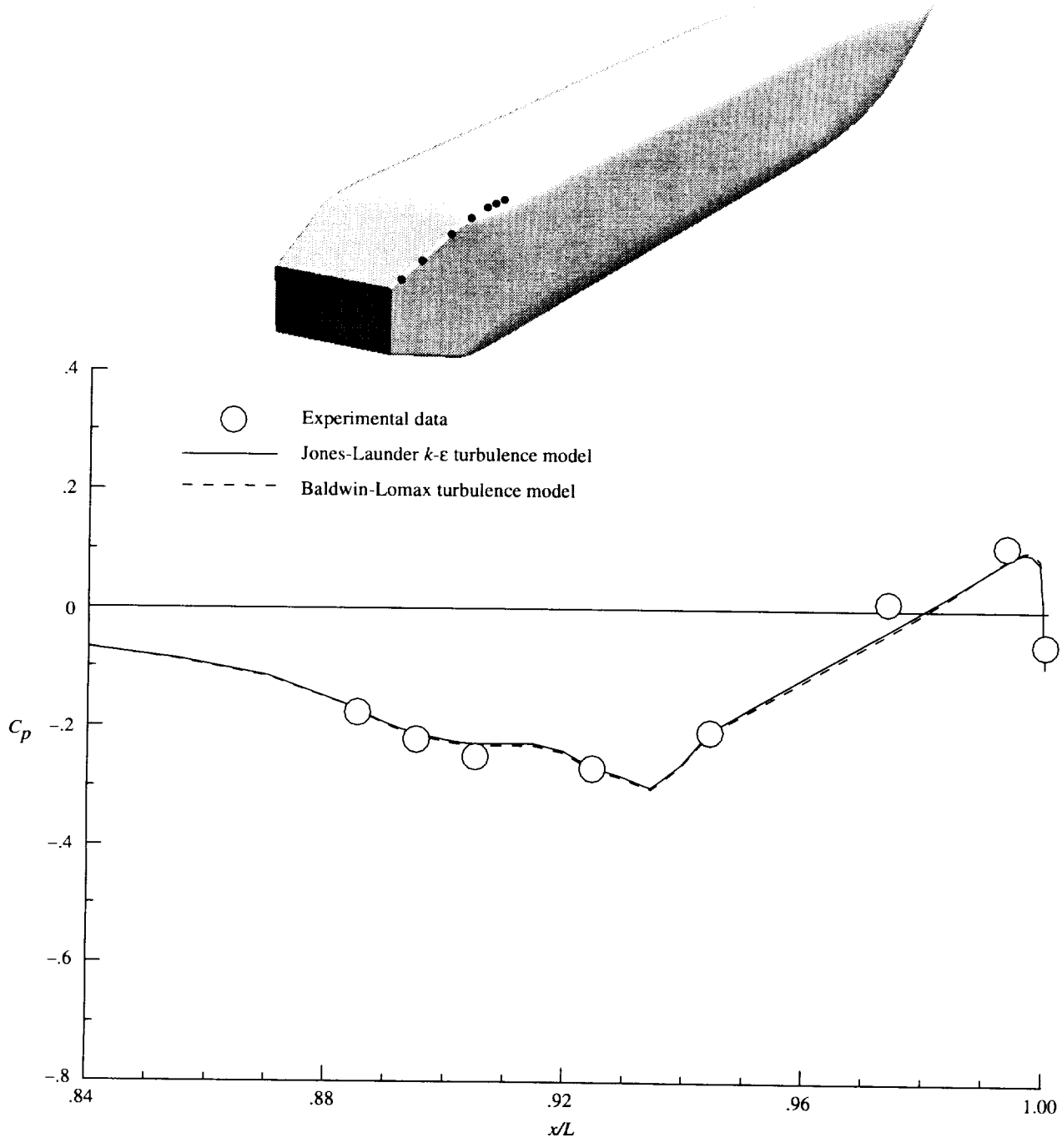

(c) $M_\infty = 0.600$; NPR = 4.003; and row 3.

Figure 12. Continued.

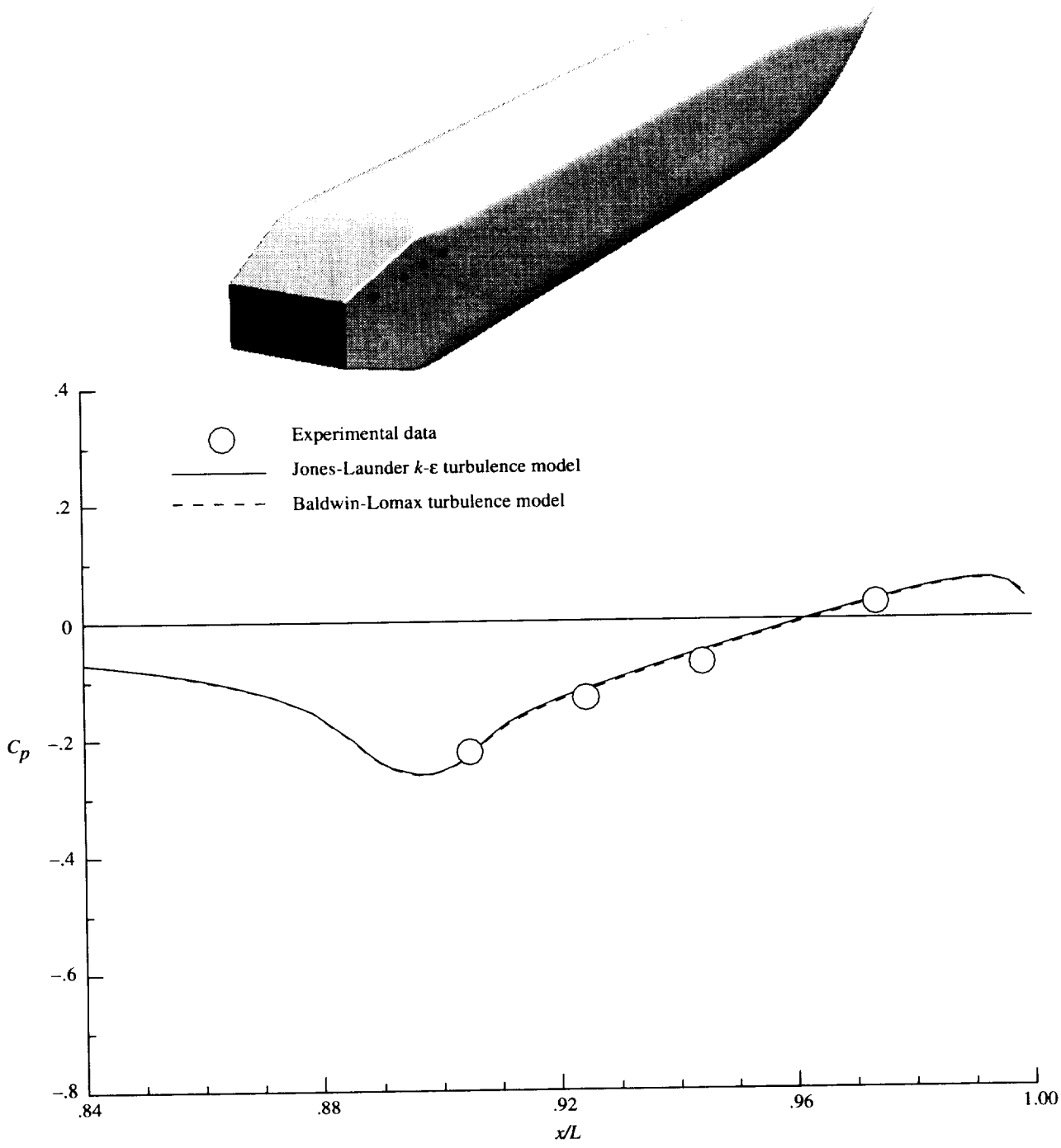

(d) $M_\infty = 0.600$; NPR = 4.003; and row 4.

Figure 12. Continued.

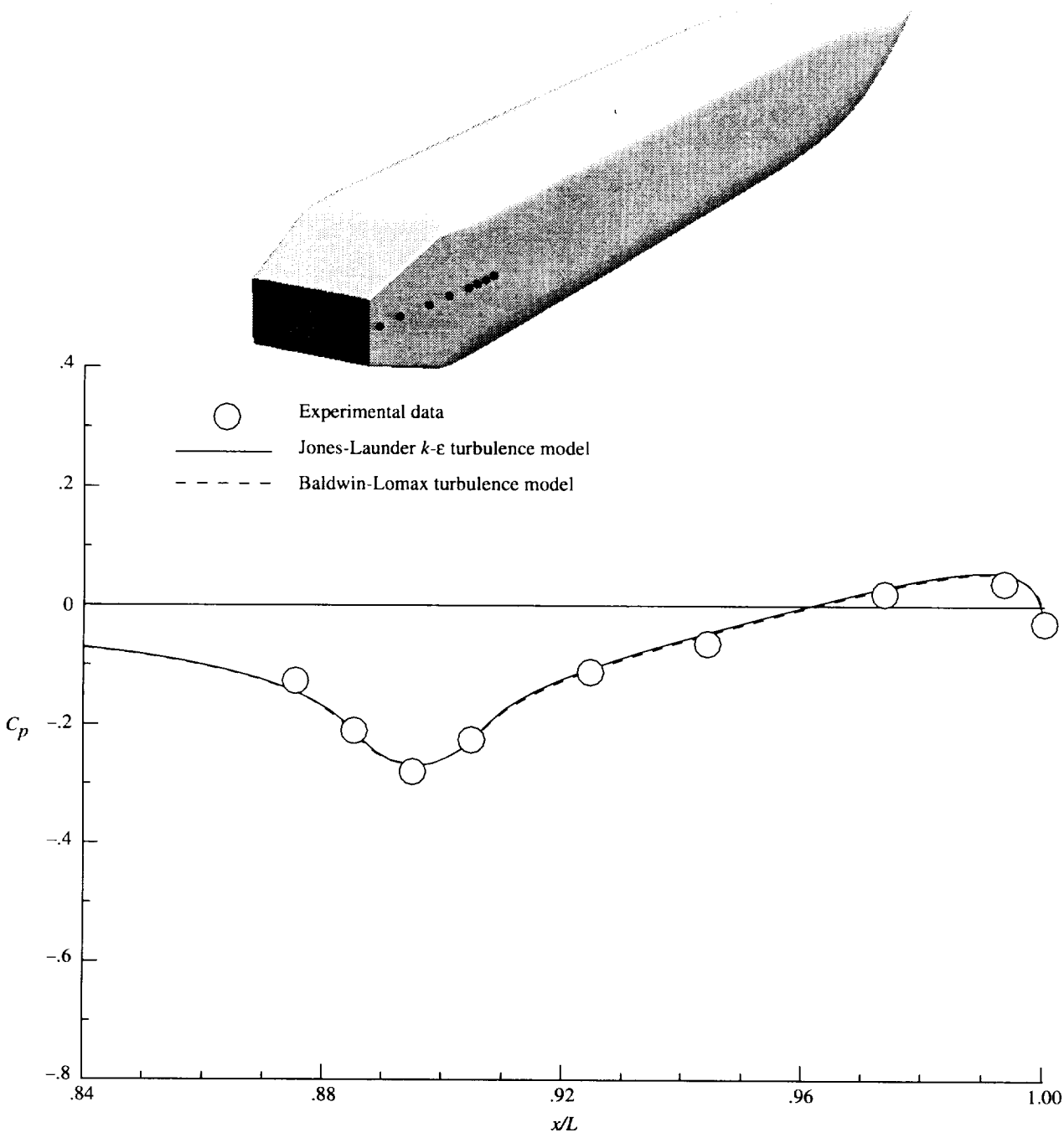

(e) $M_\infty = 0.600$; NPR = 4.003; and row 5.

Figure 12. Concluded.

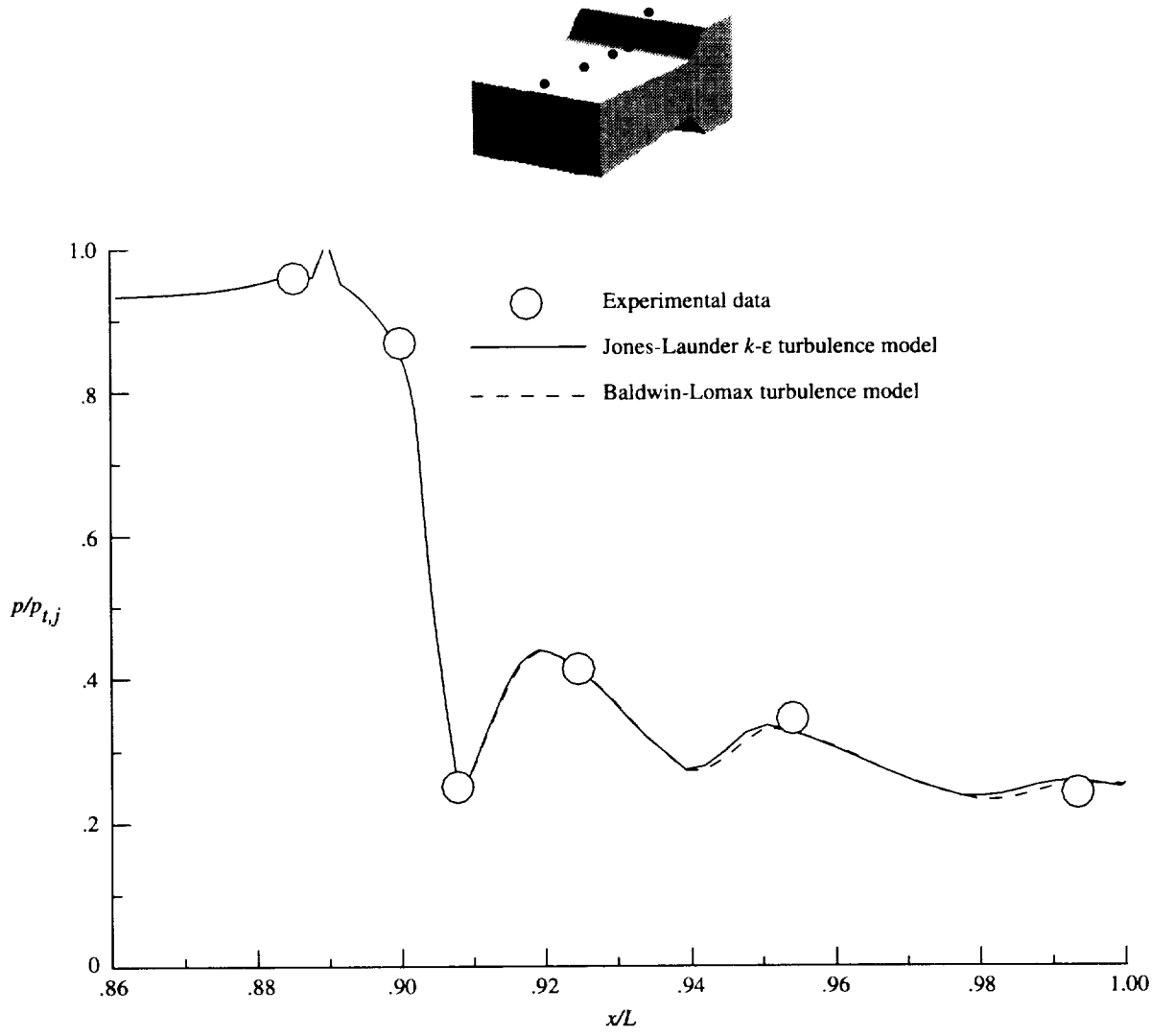

(a) $M_\infty = 0.600$; NPR = 4.003; and row 6.

Figure 13. Internal static pressure ratio distributions.

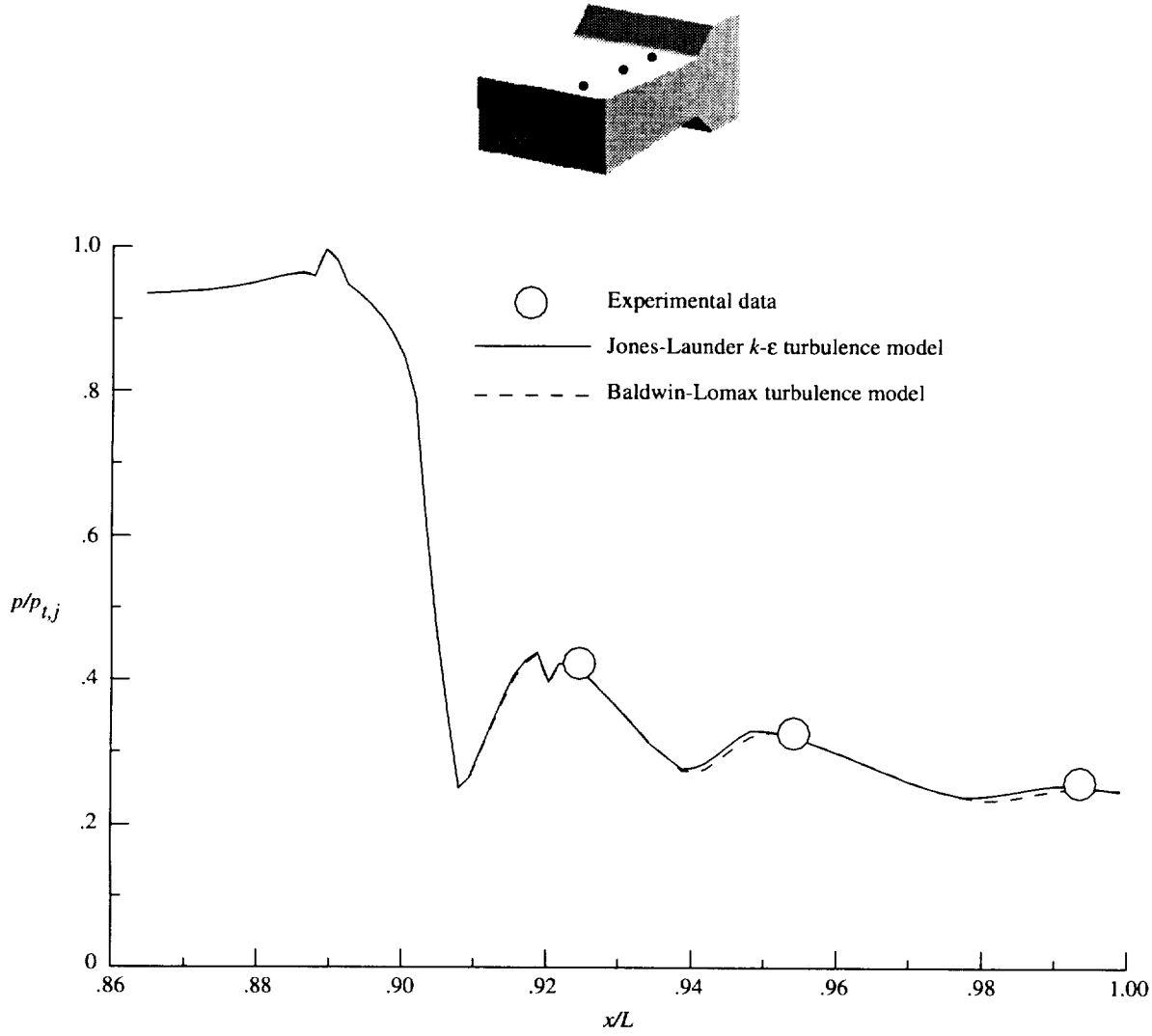

(b) $M_\infty = 0.600$; NPR = 4.003; and row 7.

Figure 13. Continued.

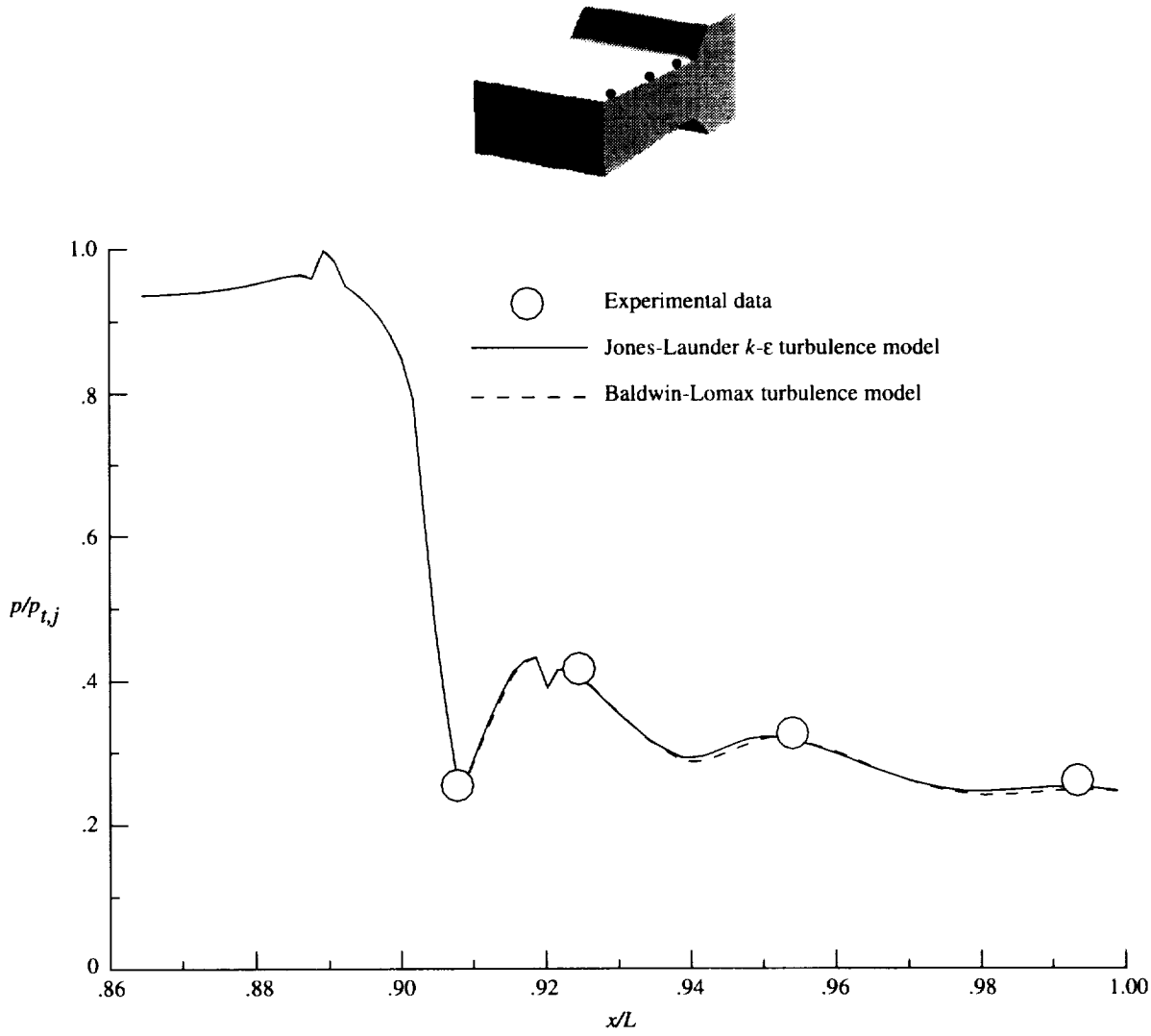

(c) $M_\infty = 0.600$; NPR = 4.003; and row 8.

Figure 13. Continued.

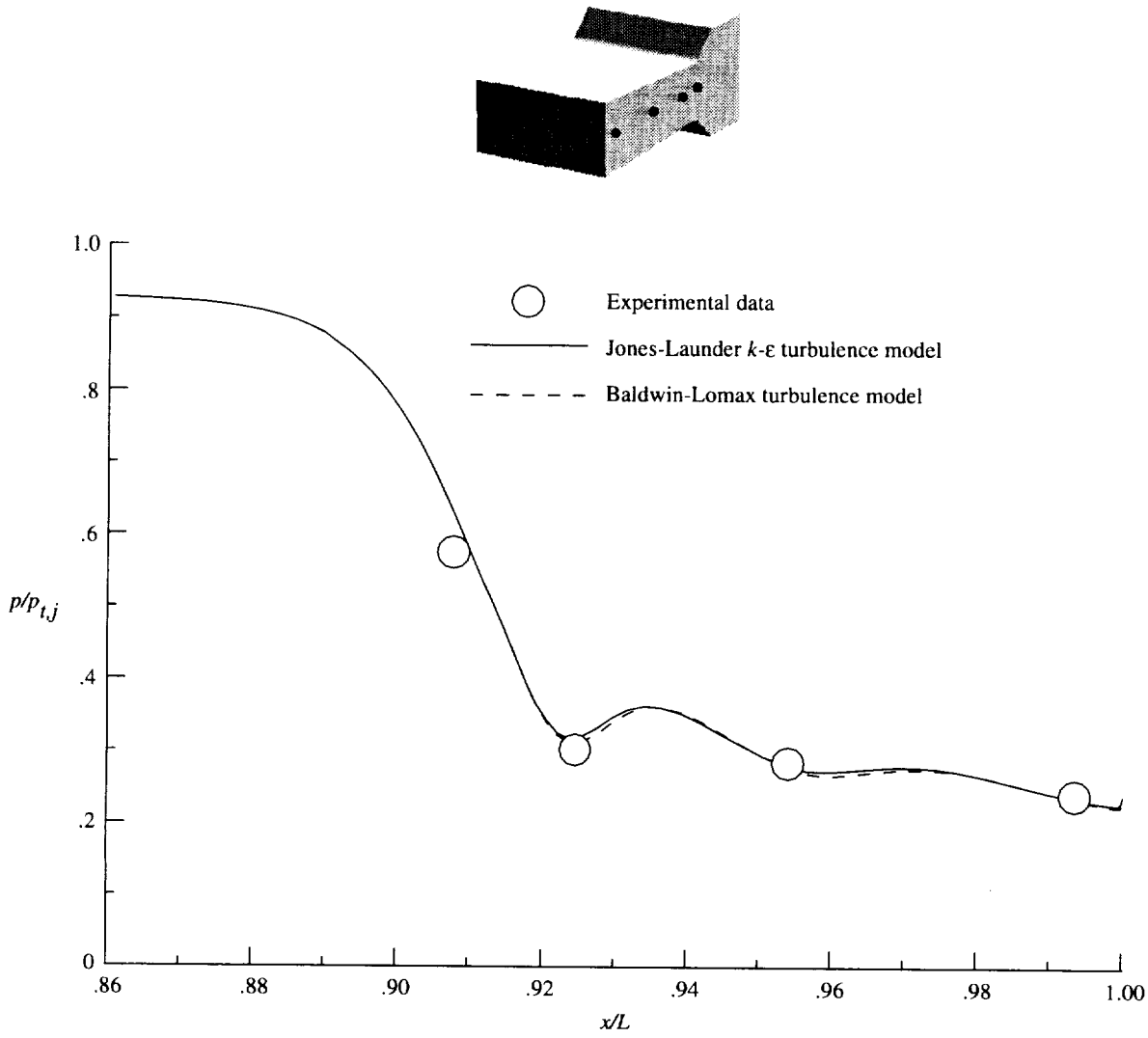

(d) $M_\infty = 0.600$; NPR = 4.003; and row 9.

Figure 13. Concluded.

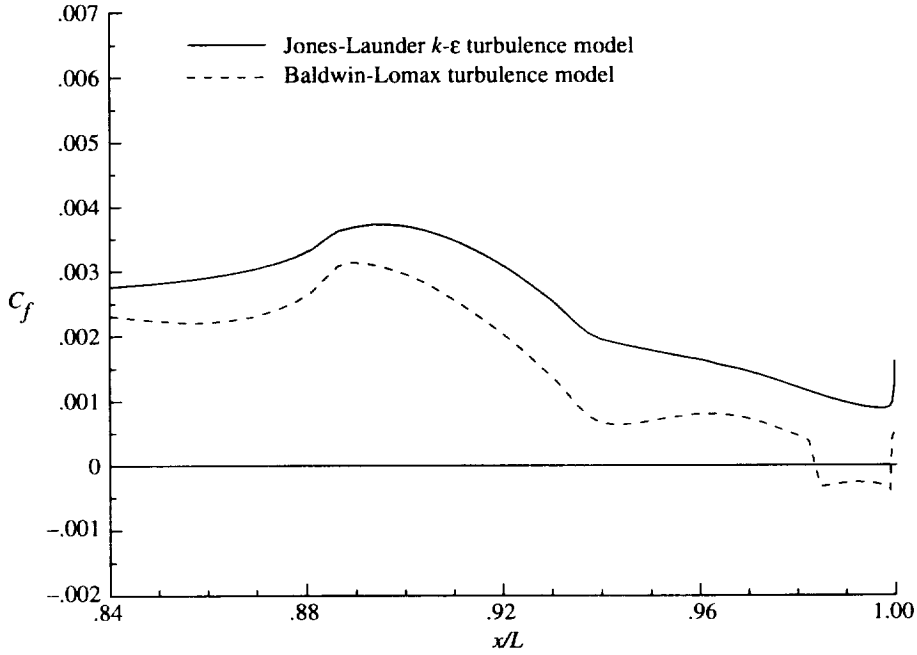

(a) $M_\infty = 0.600$; NPR = 4.003; and row 1 (external surface).

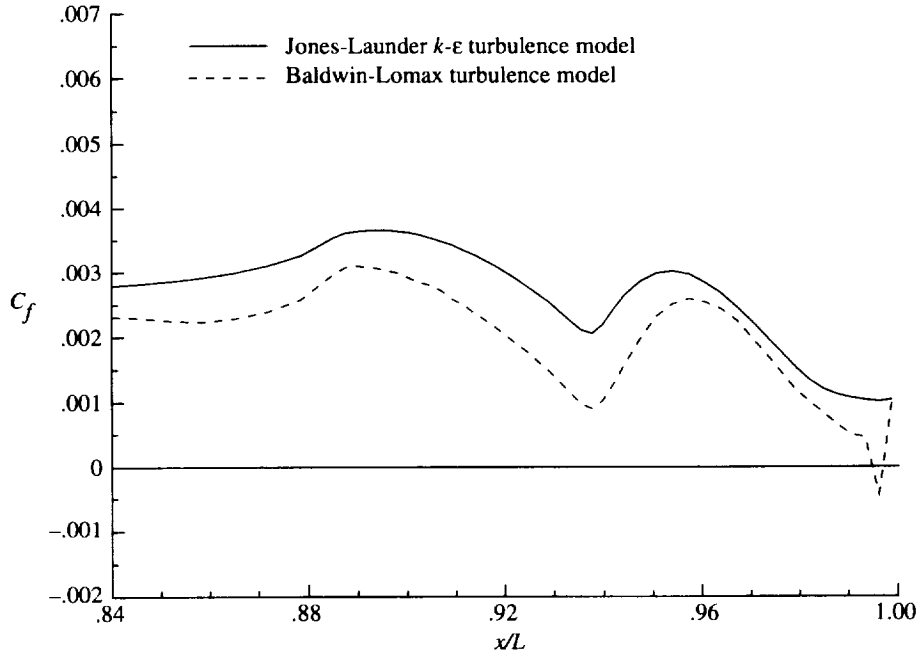

(b) $M_\infty = 0.600$; NPR = 4.003; and row 2 (external surface).

Figure 14. Skin-friction coefficient distributions.

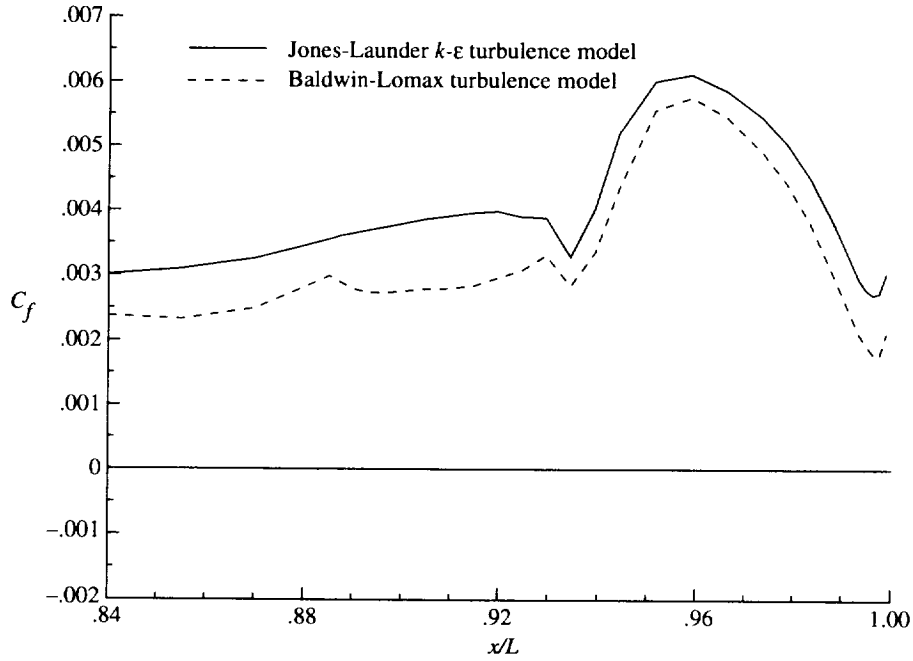

(c) $M_\infty = 0.600$; NPR = 4.003; and row 3 (external surface).

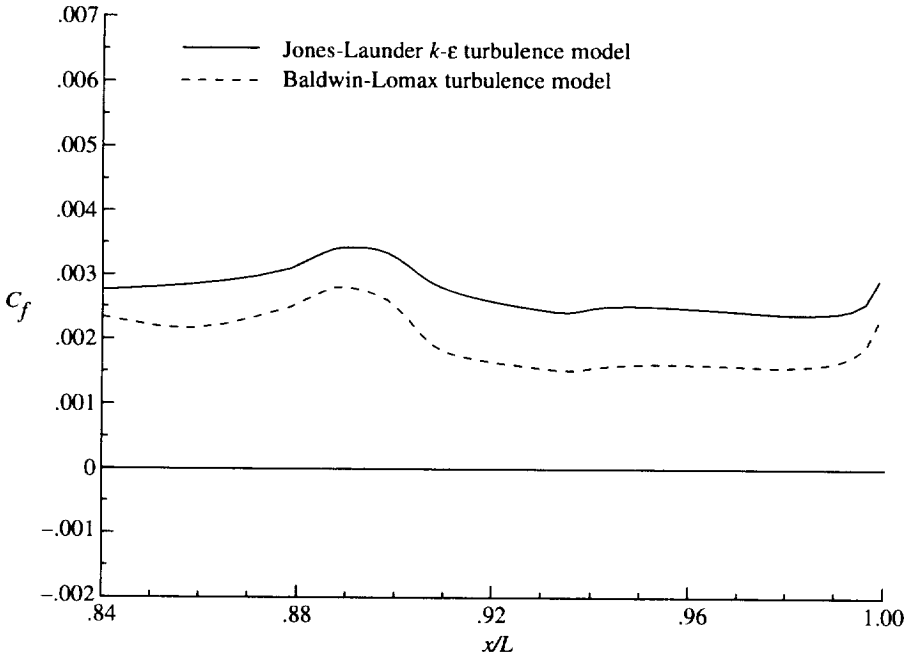

(d) $M_\infty = 0.600$; NPR = 4.003; and row 4 (external surface).

Figure 14. Continued.

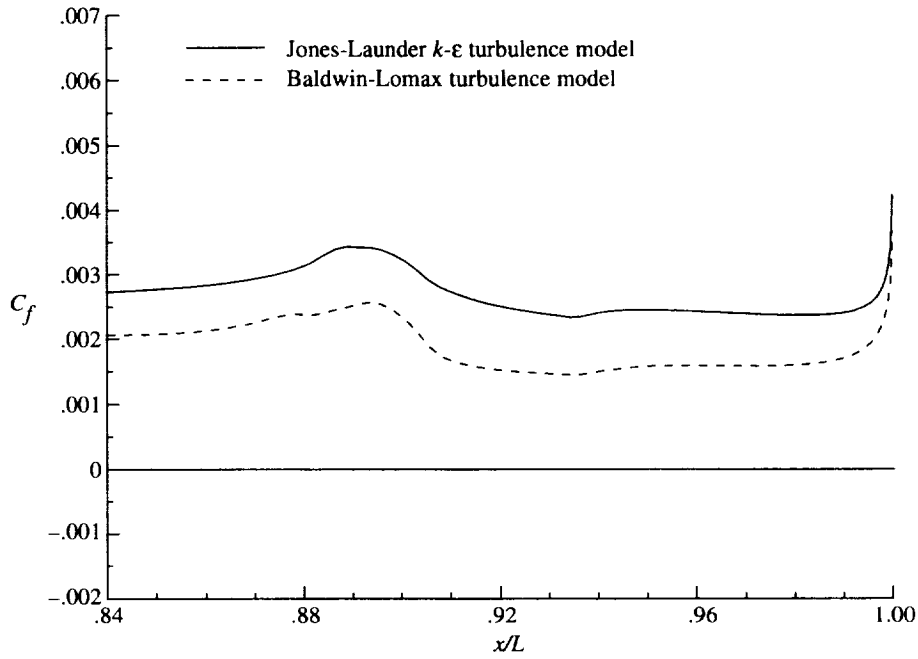

(e) $M_\infty = 0.600$; NPR = 4.003; and row 5 (external surface).

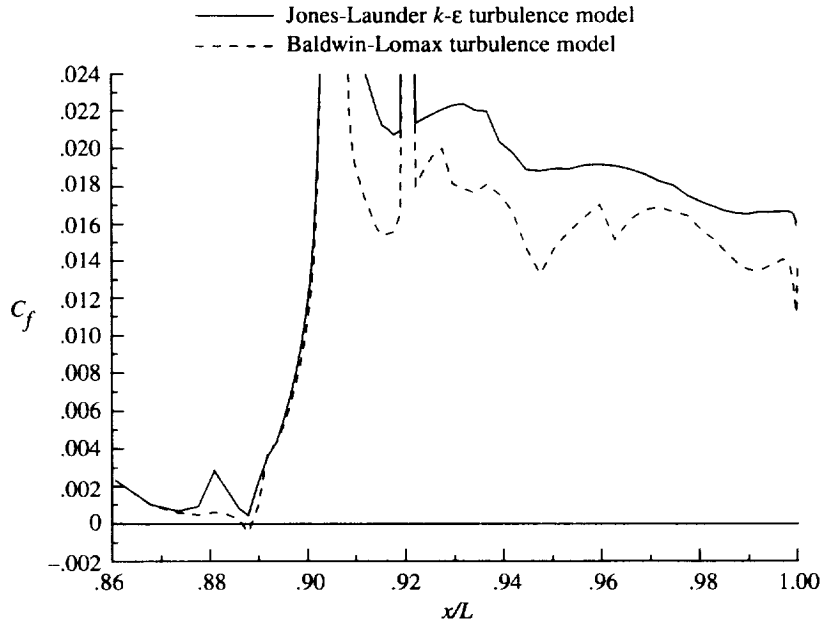

(f) $M_\infty = 0.600$; NPR = 4.003; and row 6 (internal surface).

Figure 14. Continued.

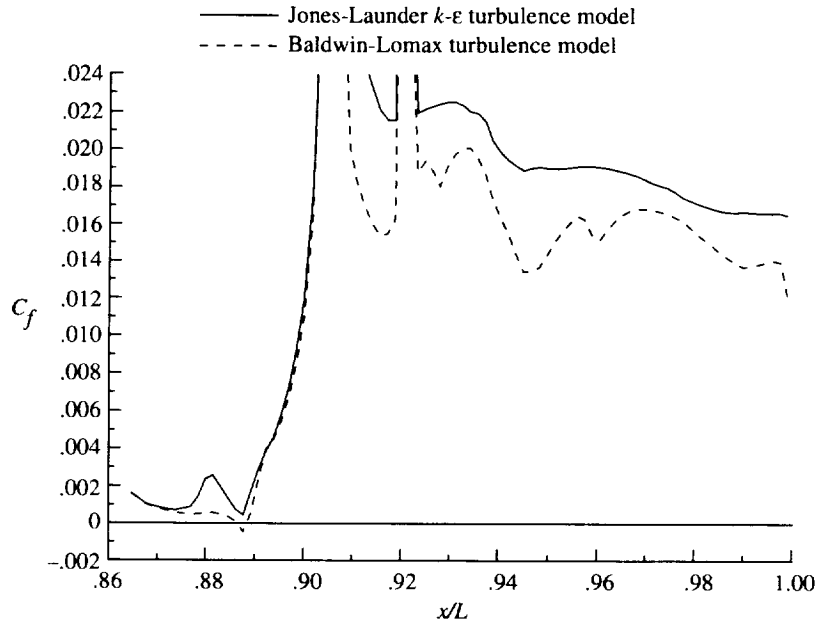

(g) $M_\infty = 0.600$; NPR = 4.003; and row 7 (internal surface).

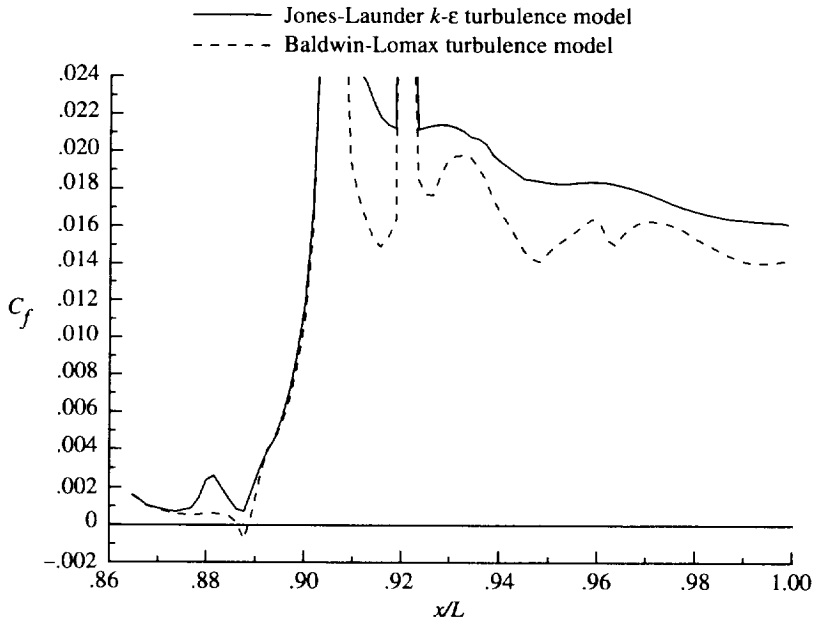

(h) $M_\infty = 0.600$; NPR = 4.003; and row 8 (internal surface).

Figure 14. Continued.

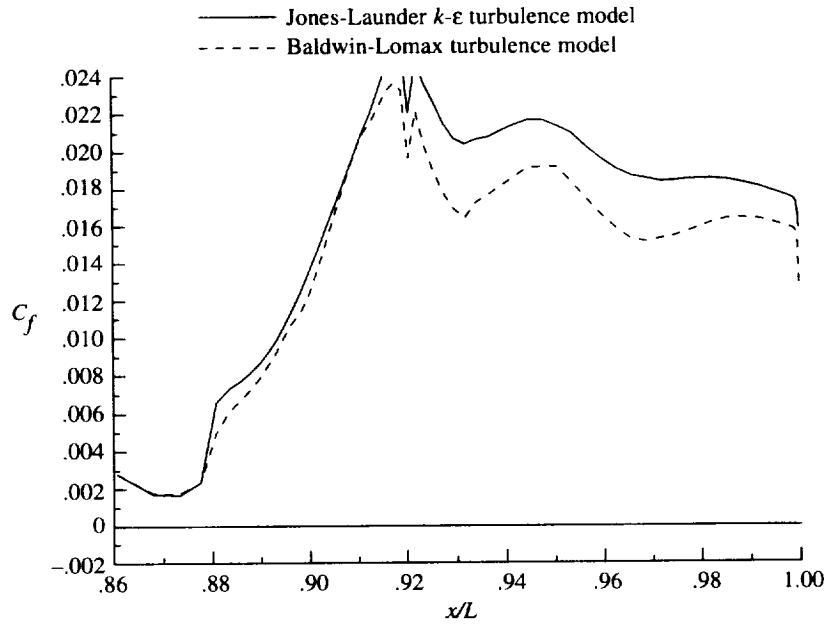

(i) $M_\infty = 0.600$; NPR = 4.003; and row 9 (internal surface).

Figure 14. Concluded.

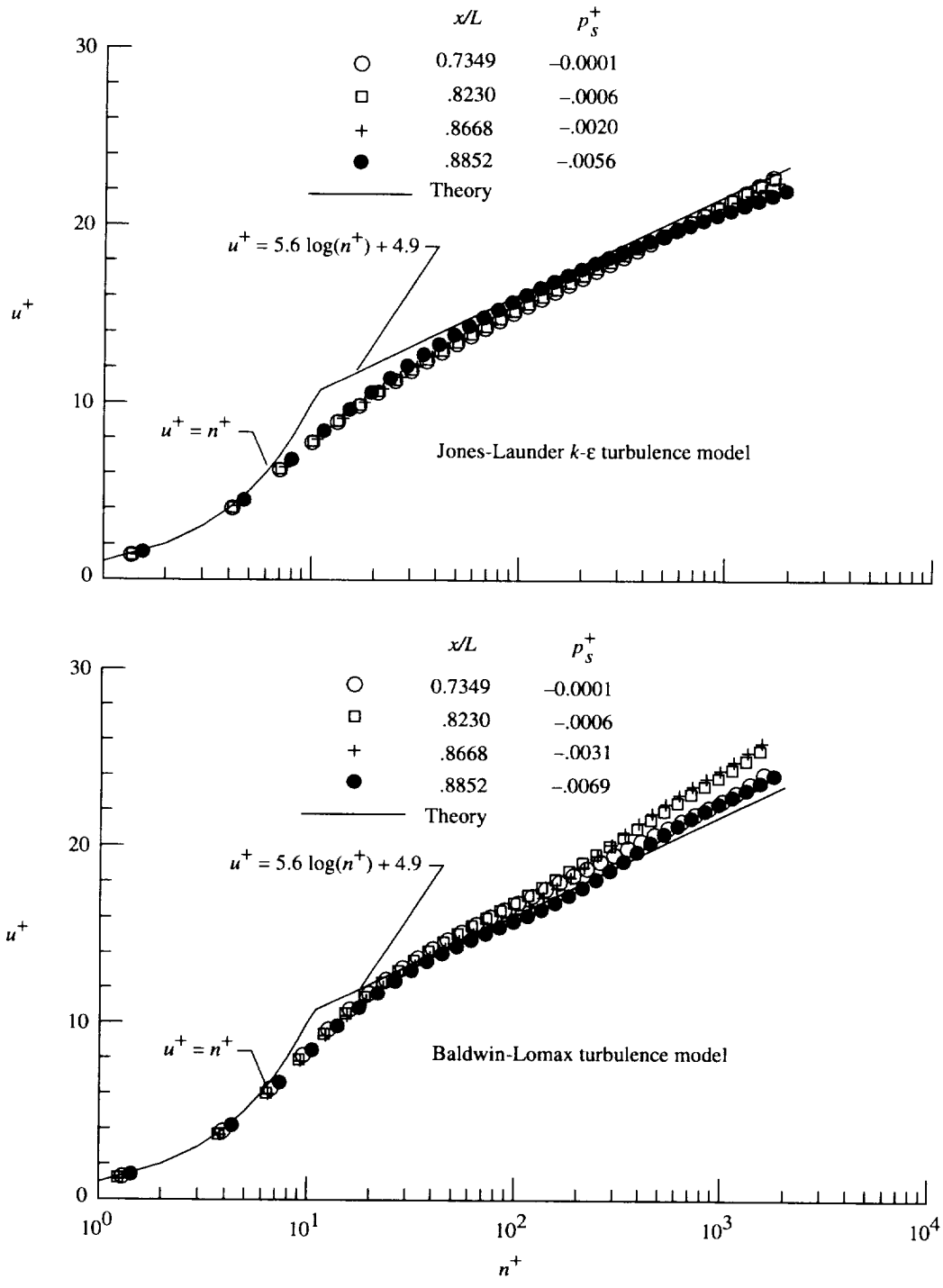

(a) $\phi = 0°$ (top row).

Figure 15. Universal law-of-the-wall boundary layer profiles at $M_\infty = 0.600$.

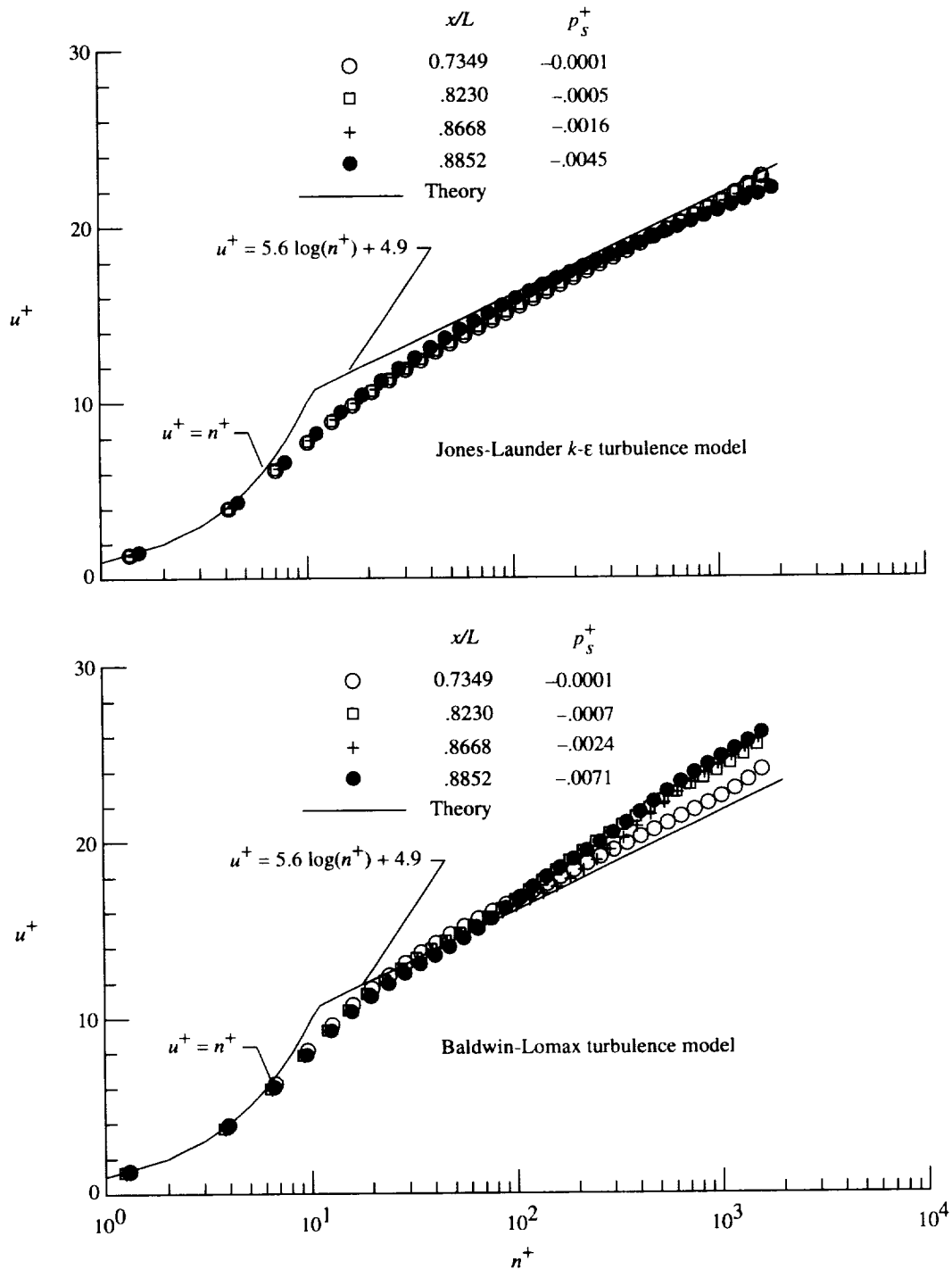

(b) $\phi = 90°$ (side row).

Figure 15. Concluded.

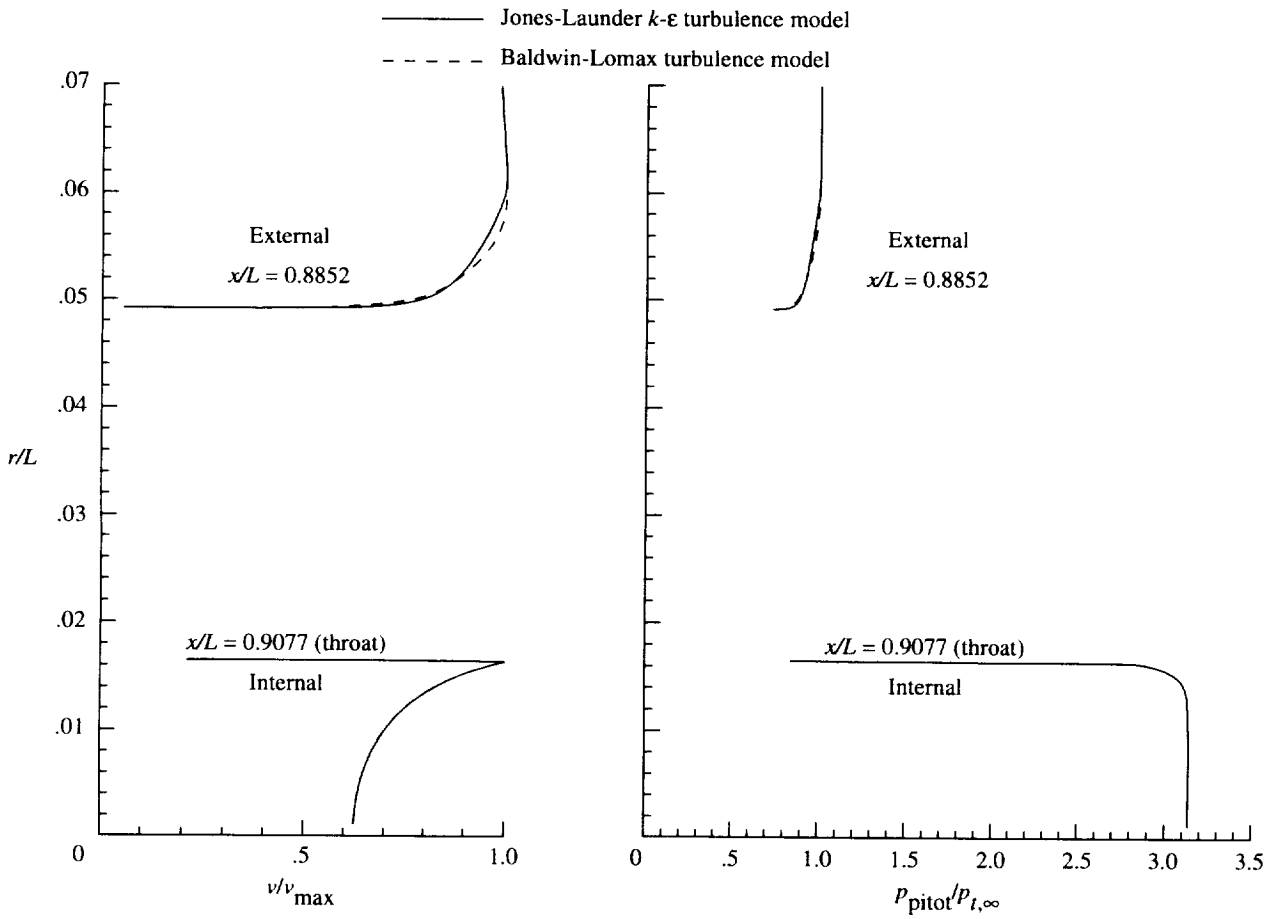

(a) $\phi = 0°$.

Figure 16. Boundary layer profiles at $M_\infty = 0.600$.

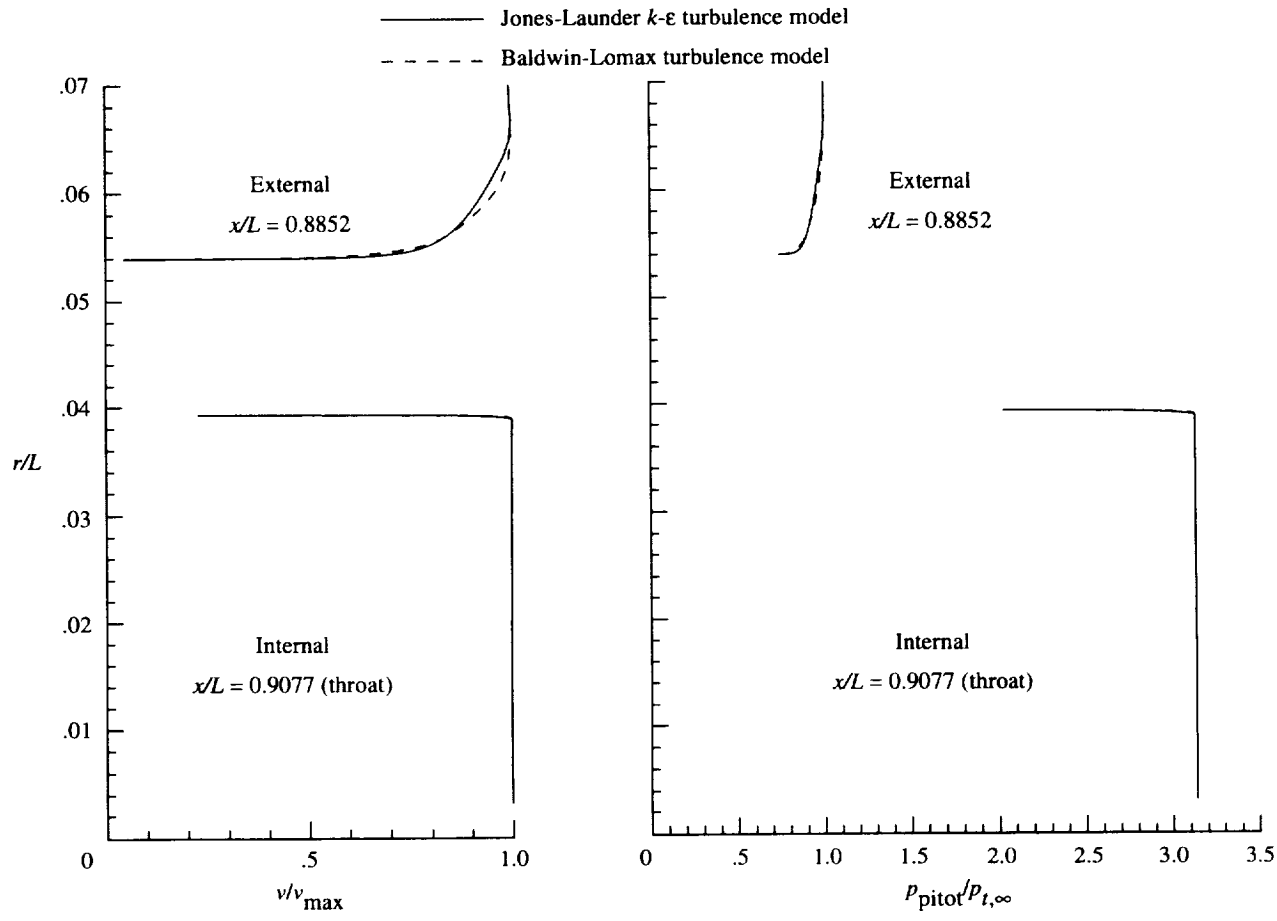

(b) $\phi = 90°$.

Figure 16. Continued.

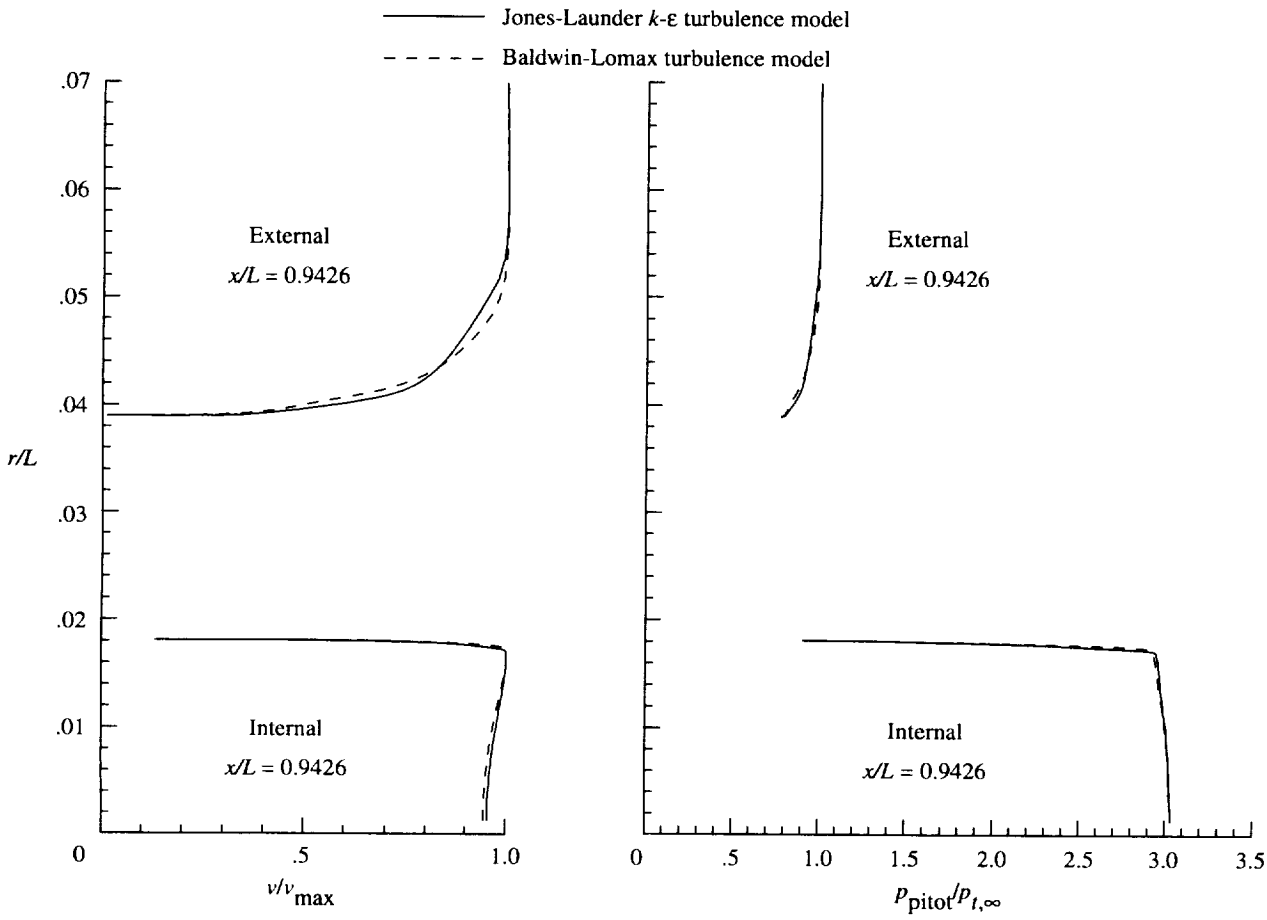

(c) $\phi = 0°$.

Figure 16. Continued.

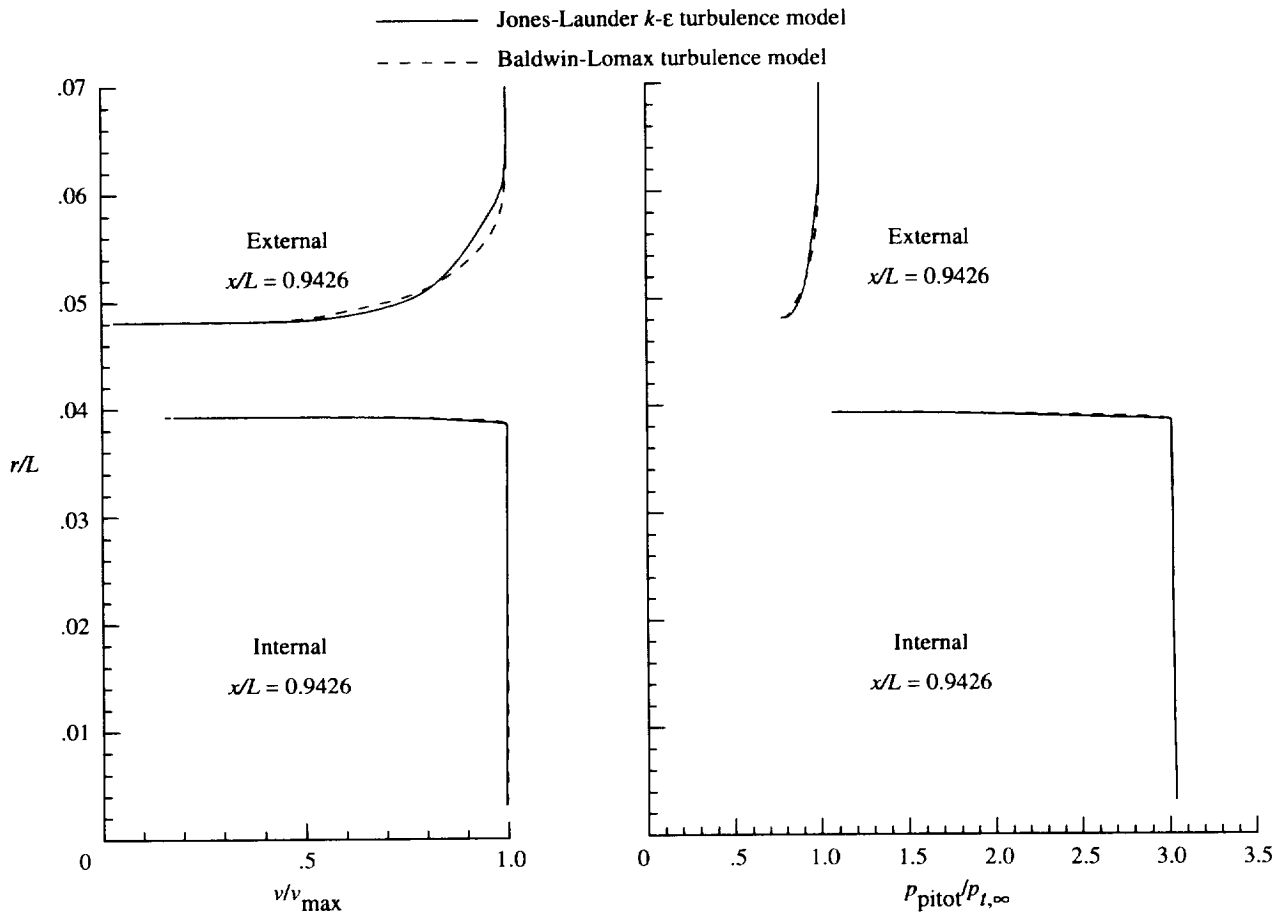

(d) $\phi = 90°$.

Figure 16. Continued.

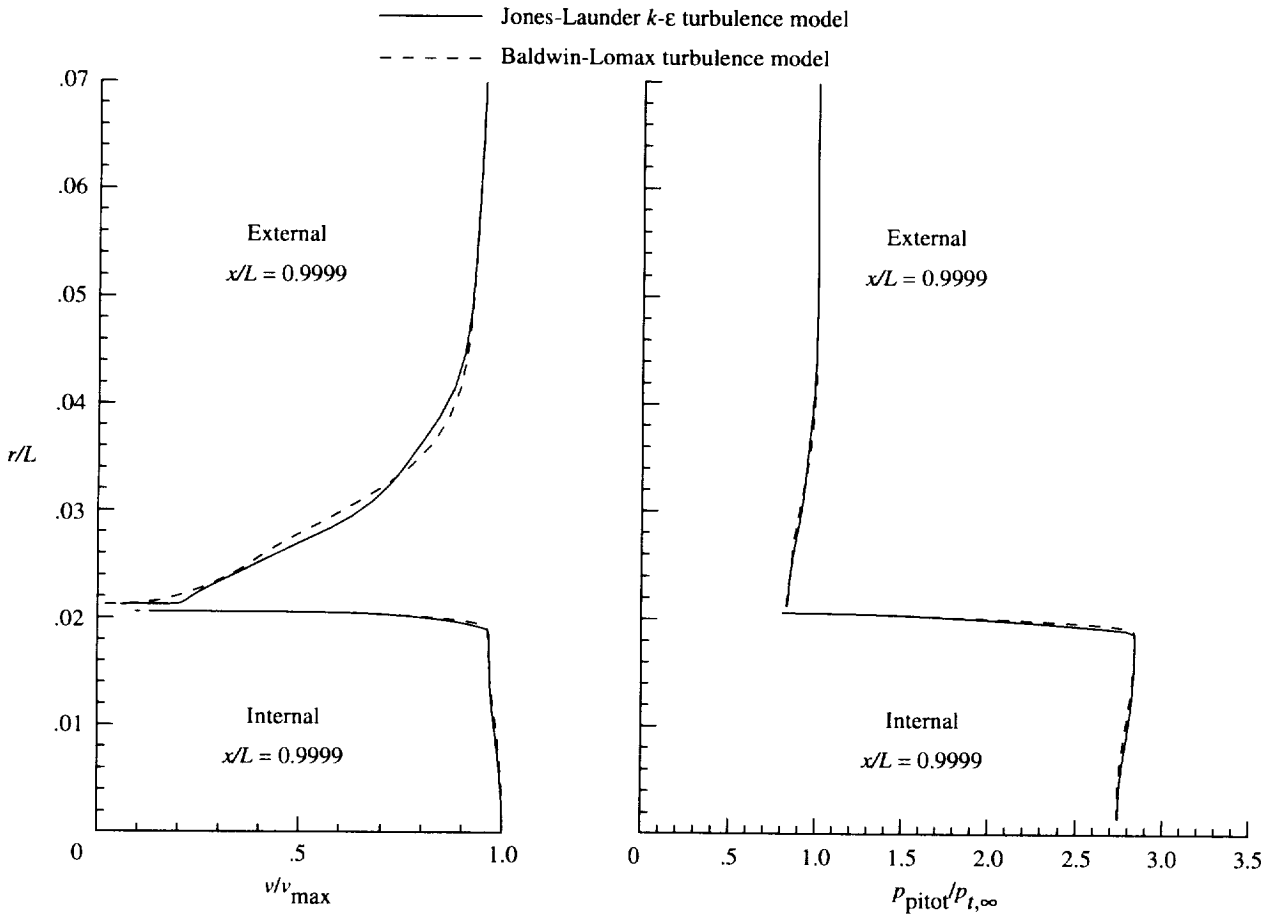

(e) $\phi = 0°$.

Figure 16. Continued.

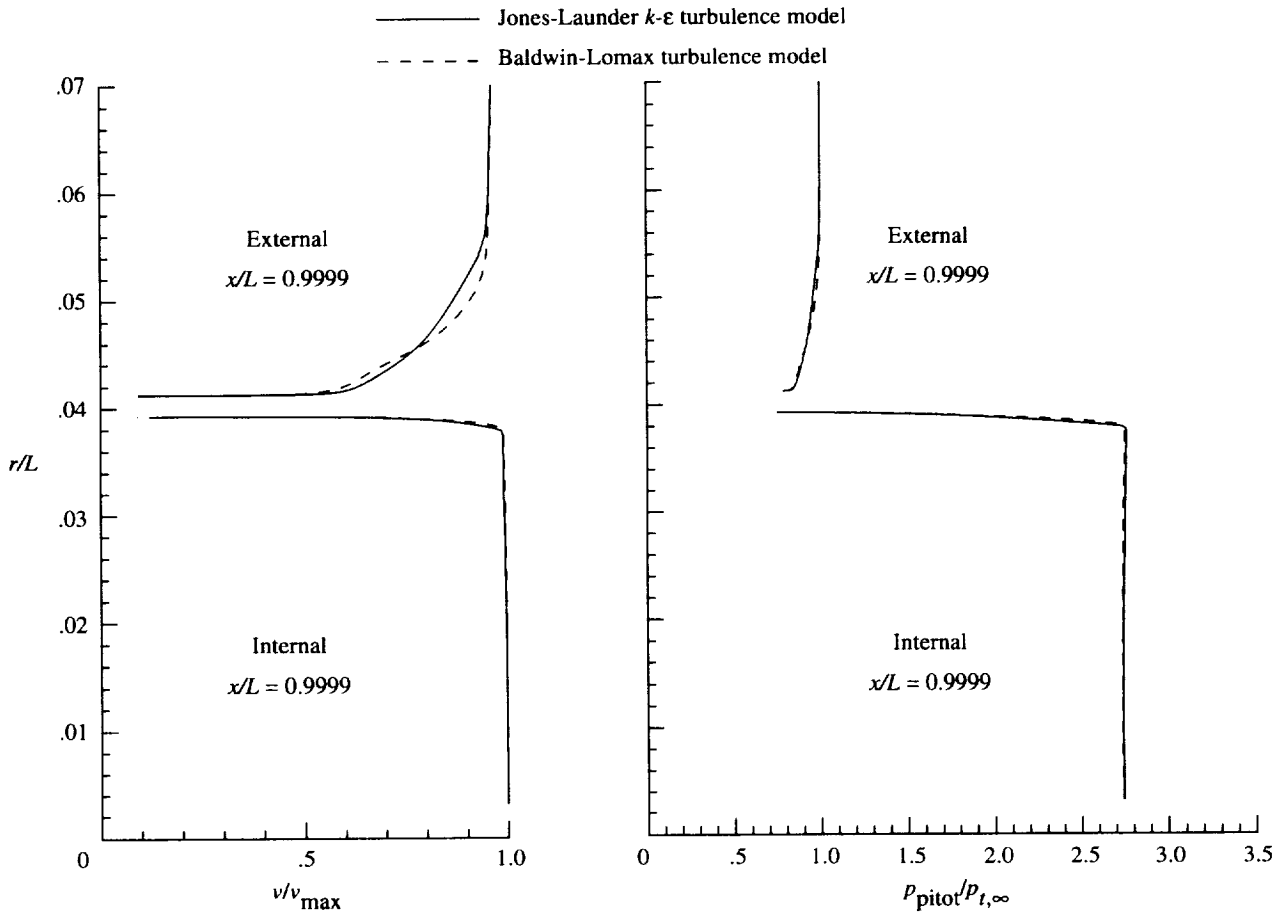

(f) $\phi = 90°$.

Figure 16. Concluded.

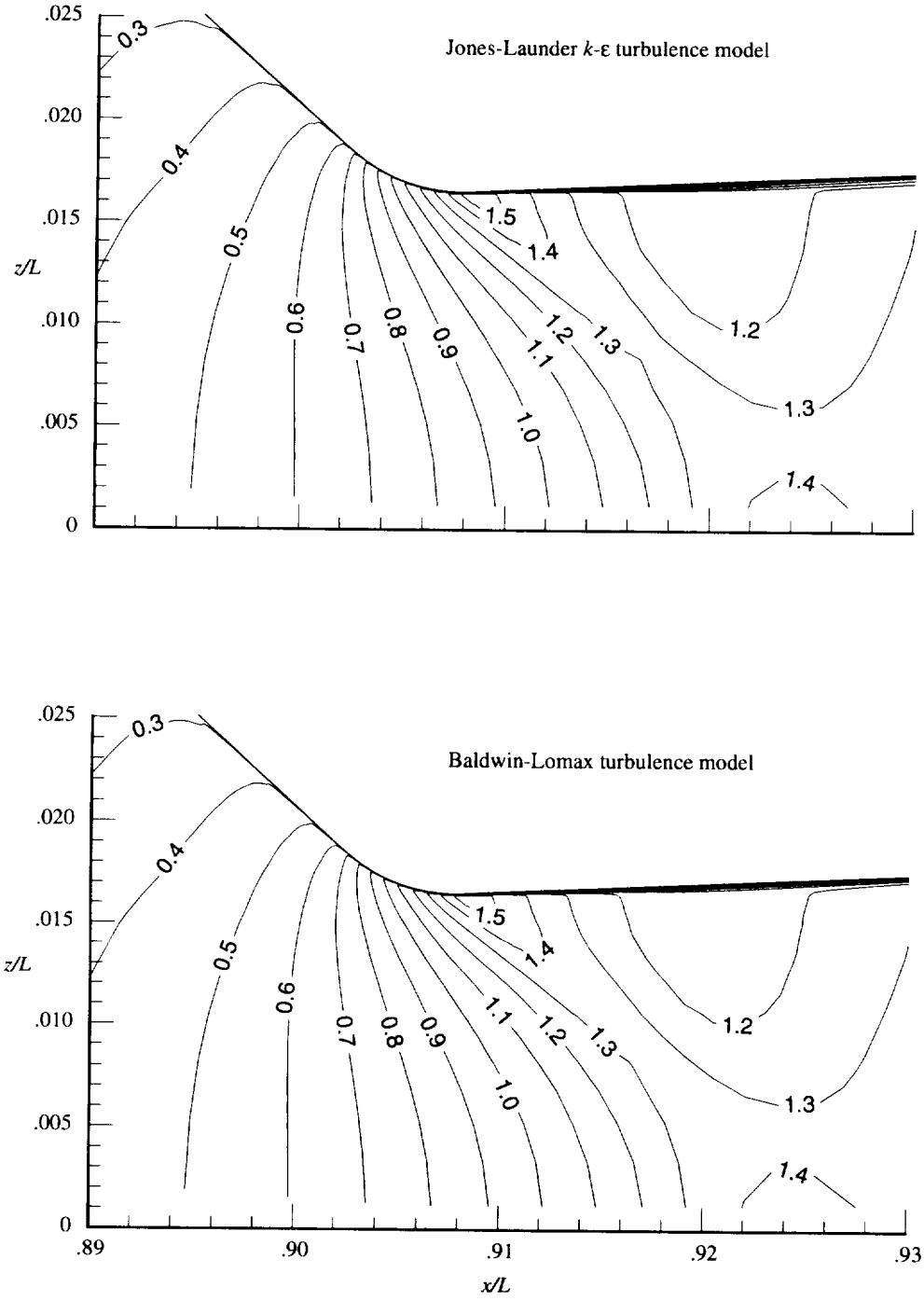

Figure 17. Mach number contours in vicinity of nozzle throat. Vertical plane of symmetry; NPR = 4.003; and $M_\infty = 0.600$.

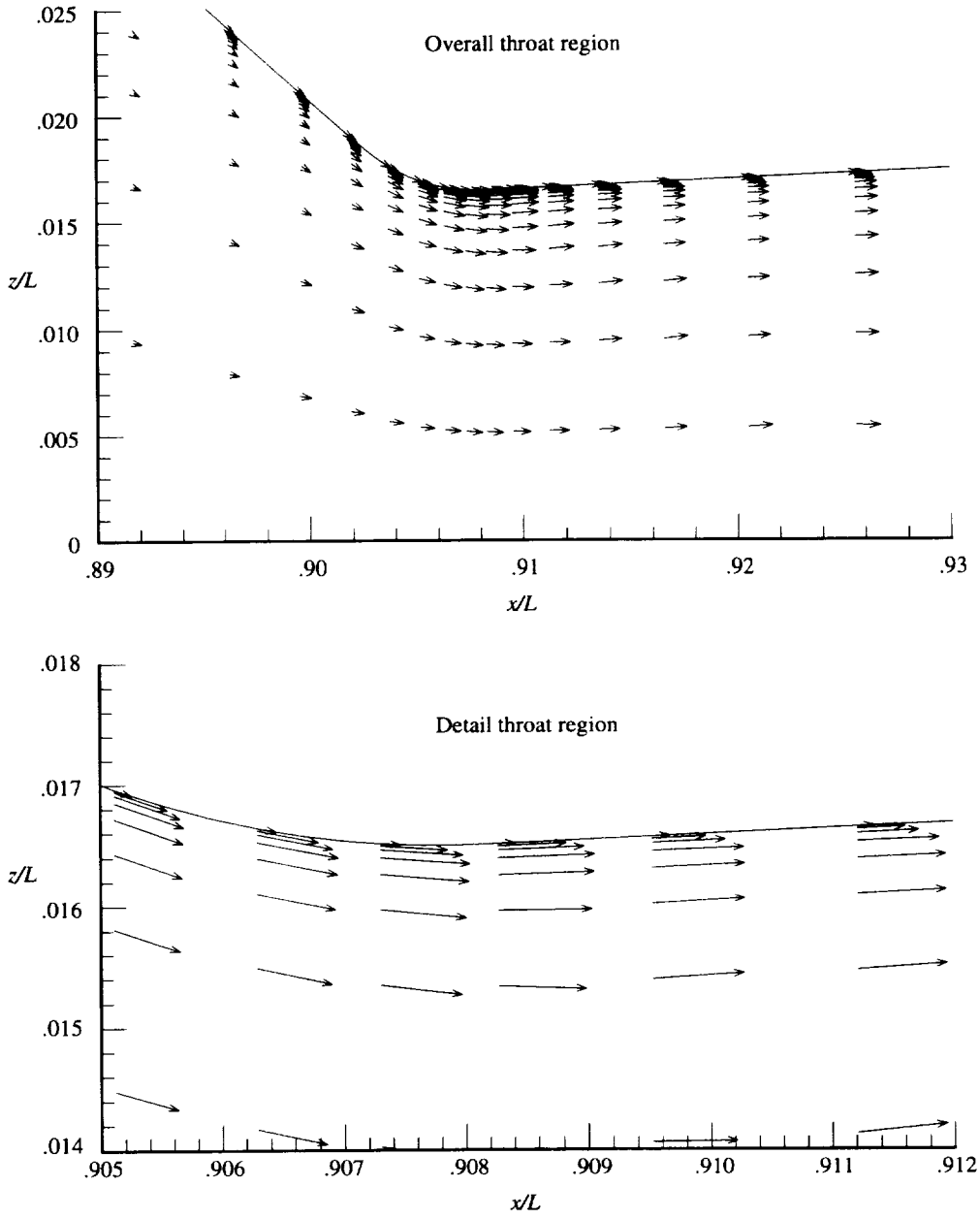

Figure 18. Velocity vectors in vicinity of nozzle throat (most vectors not shown for clarity). Vertical plane of symmetry; Jones-Launder k-ε turbulence model; $M_\infty = 0.600$; and NPR = 4.003.

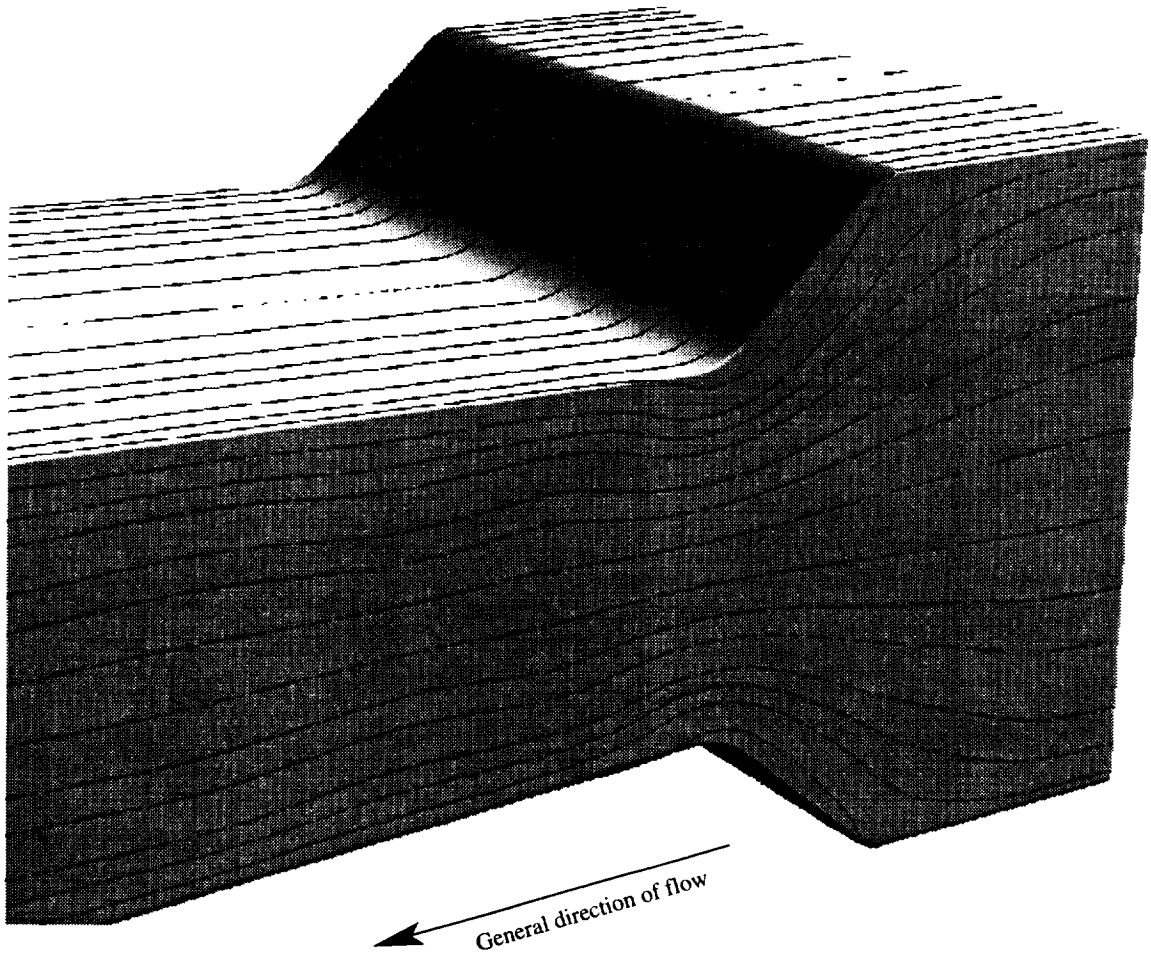

Figure 19. Details of computed oil flow (particle traces) in vicinity of nozzle throat. $M_\infty = 0.600$; NPR = 4.003; and Jones-Launder k-ε turbulence model.

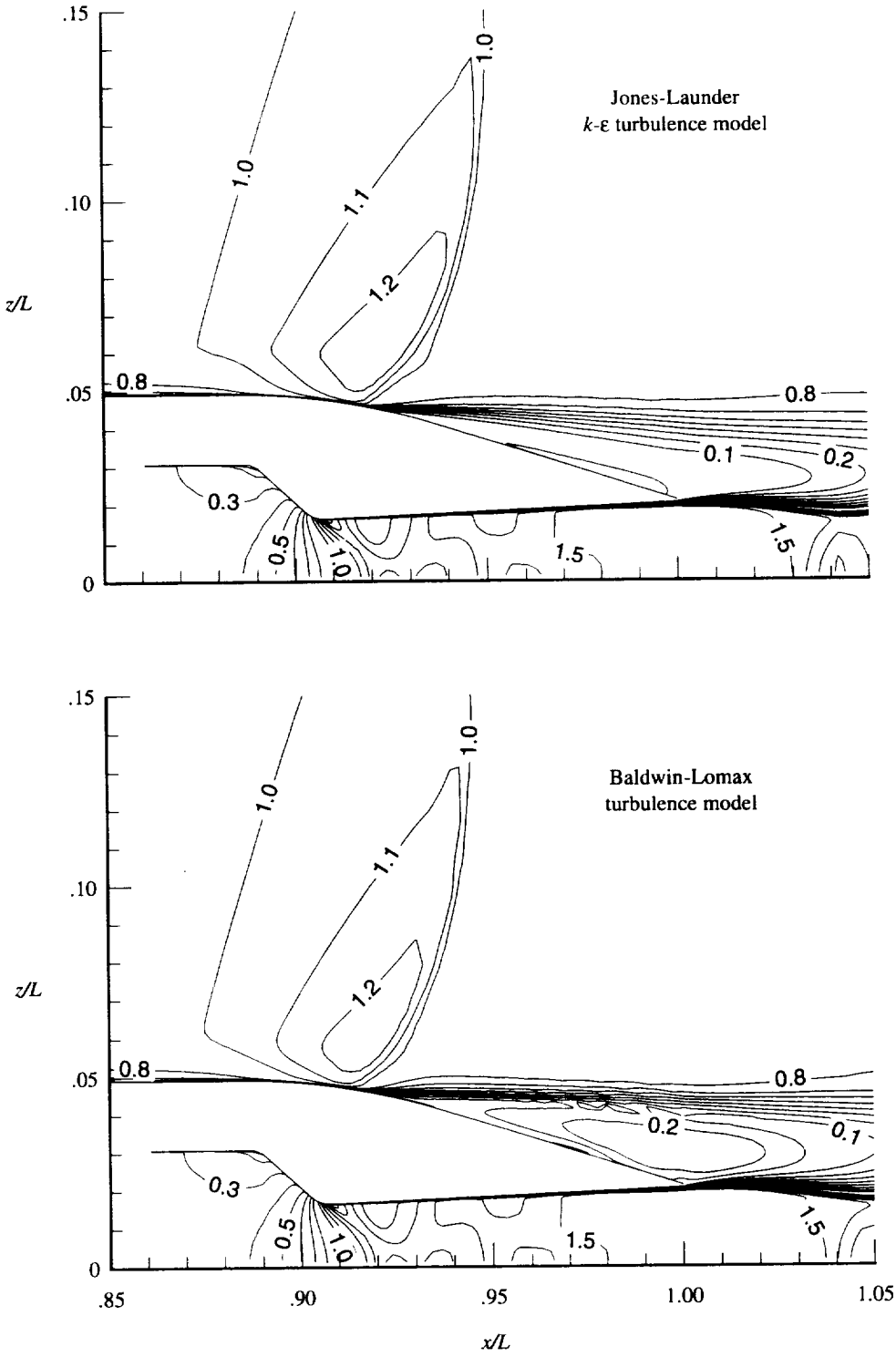

(a) Vertical plane of symmetry.

Figure 20. Mach number contours. M_∞ = 0.938; NPR = 4.107; and contour increment = 0.1.

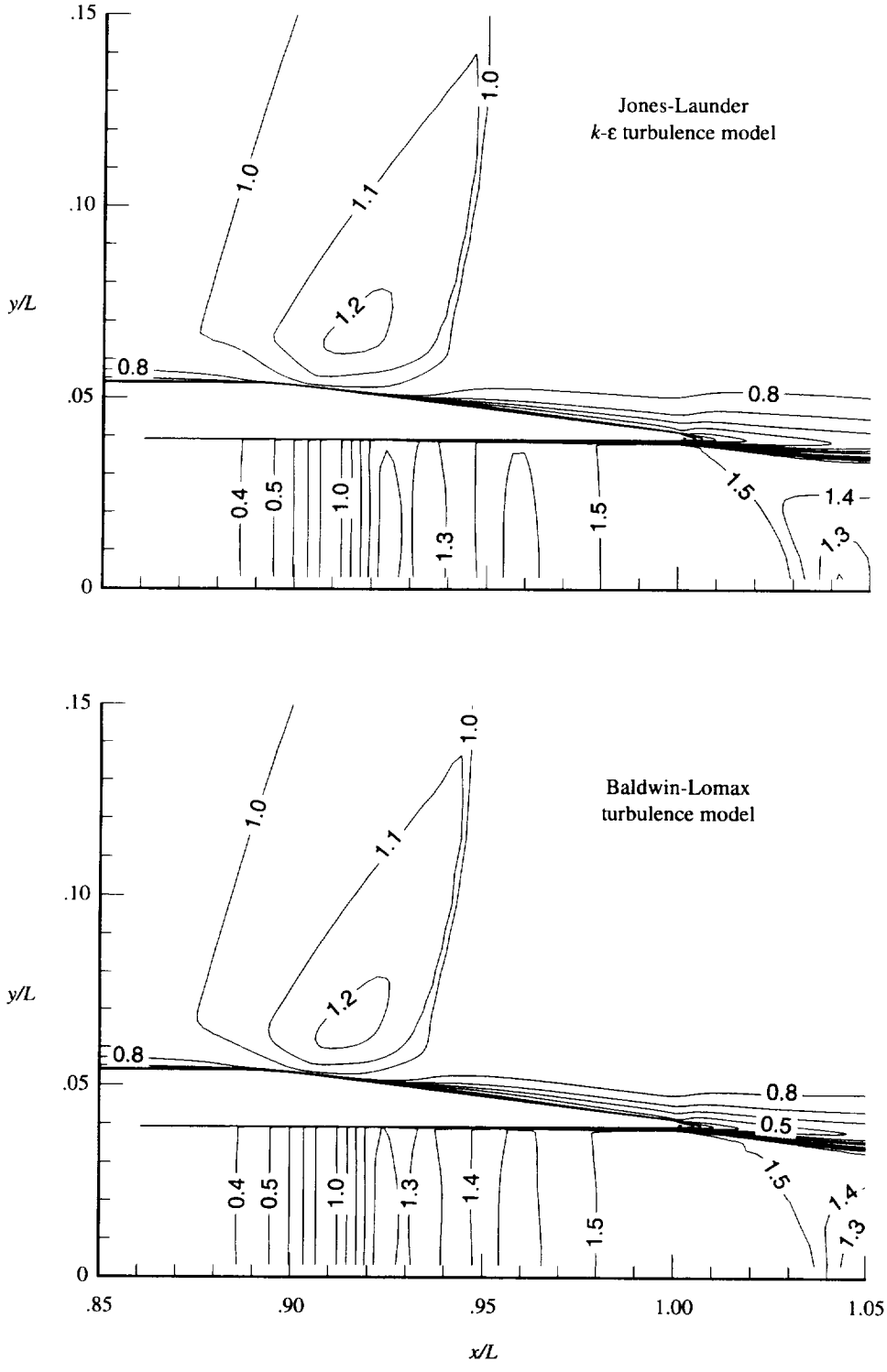

(b) Horizontal plane of symmetry.

Figure 20. Concluded.

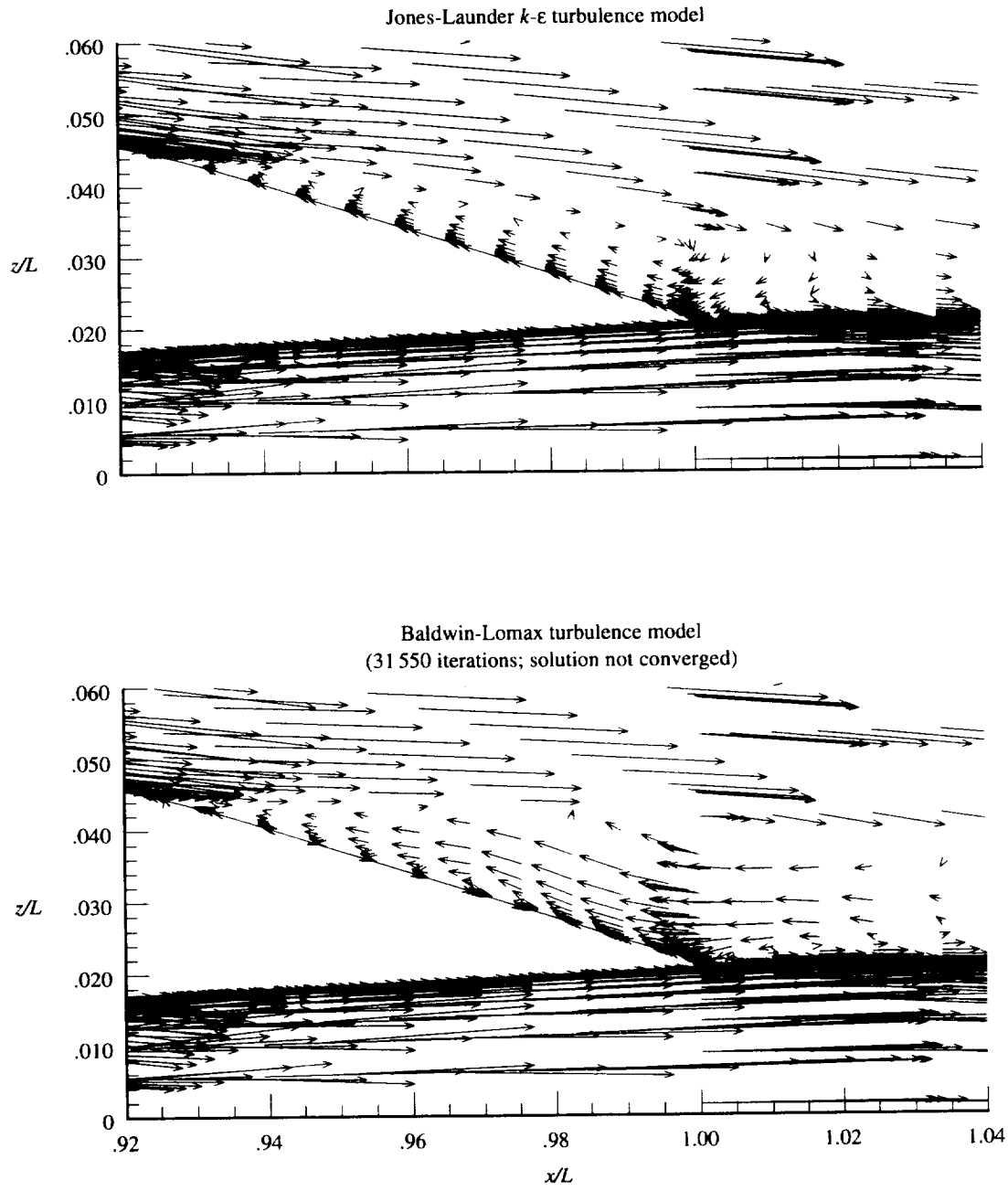

(a) Vertical plane of symmetry.

Figure 21. Velocity vectors (most vectors not shown for clarity) $M_\infty = 0.938$ and NPR = 4.017.

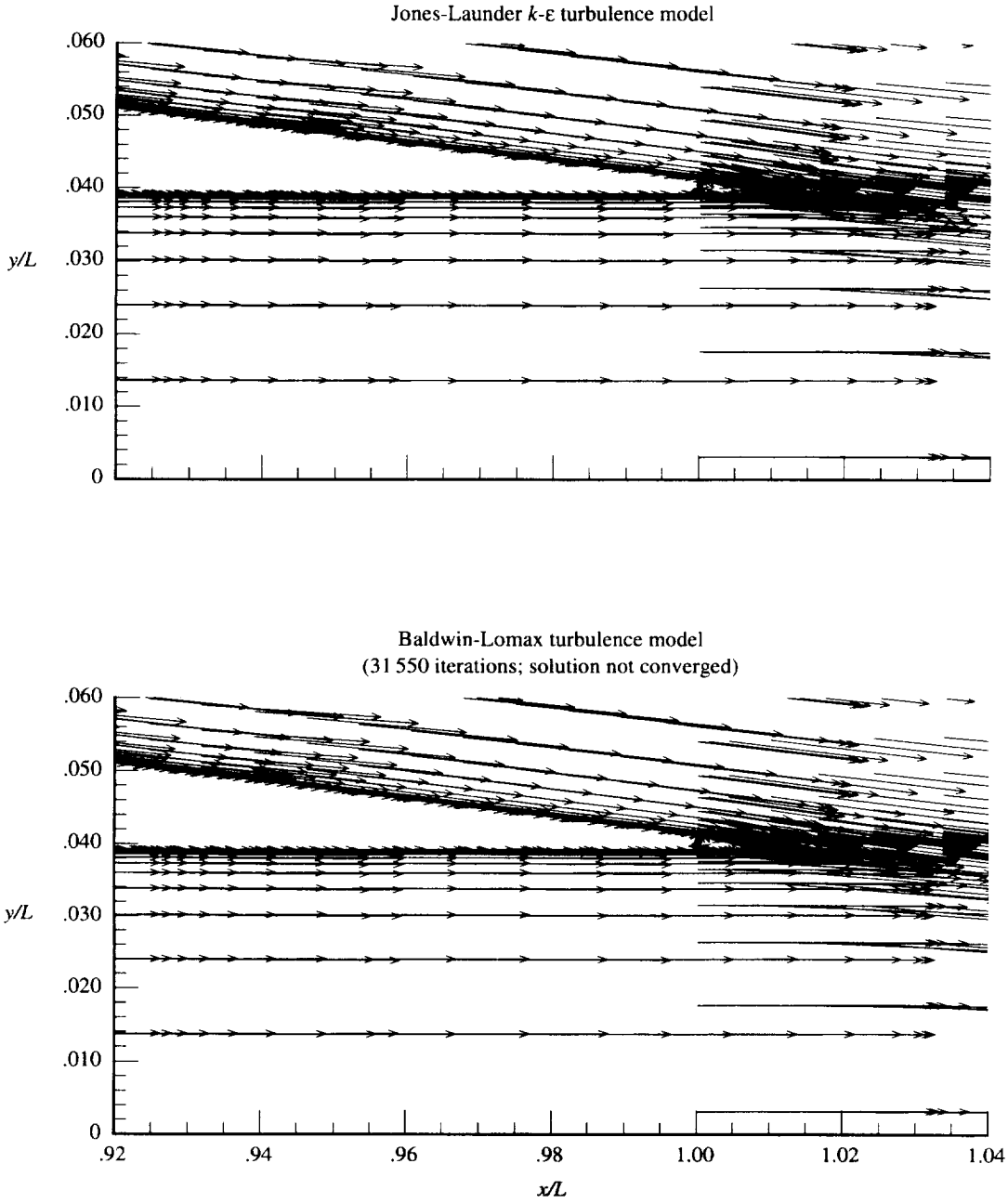

(b) Horizontal plane of symmetry.

Figure 21. Concluded.

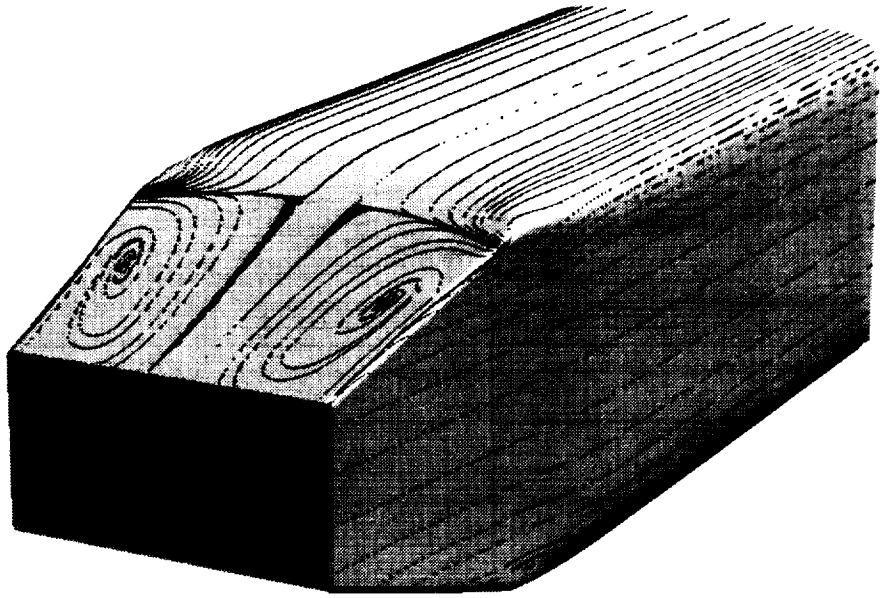

Jones-Launder k-ε turbulence model

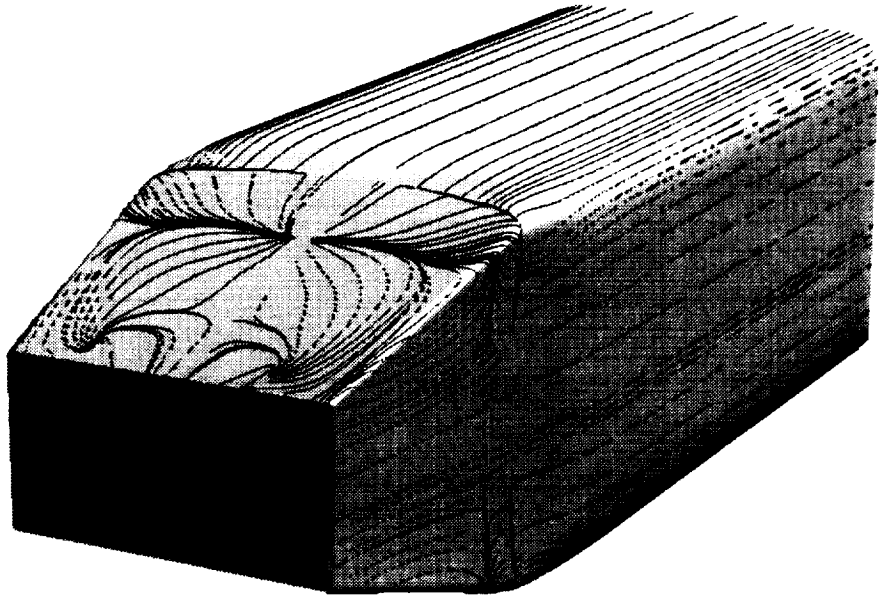

Baldwin-Lomax turbulence model
(31 550 iterations; solution not converged)

(a) External surface.

Figure 22. Computed oil flows (particle traces) on nozzle-afterbody surface $M_\infty = 0.938$ and NPR = 4.017.

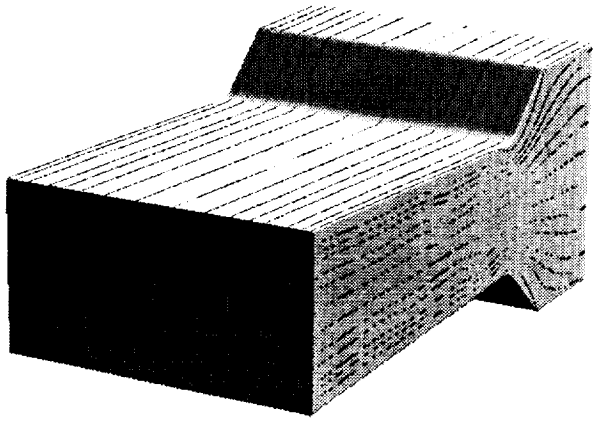

Jones-Launder k-ε turbulence model

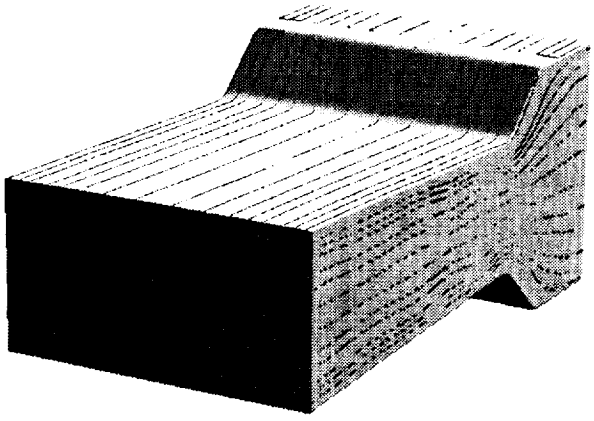

Baldwin-Lomax turbulence model

(b) Internal nozzle surface.

Figure 22. Concluded.

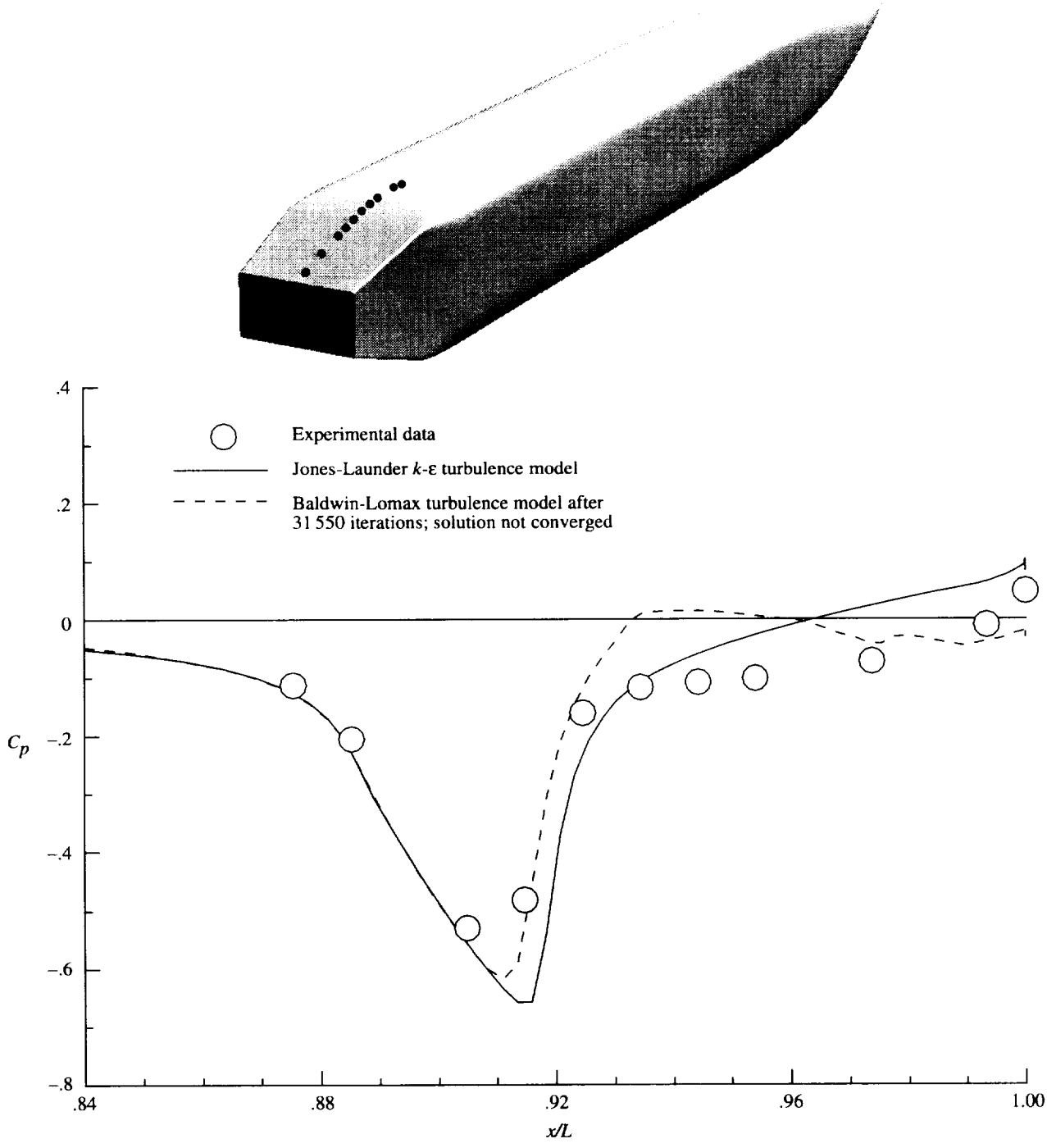

(a) $M_\infty = 0.938$; NPR = 4.017; and row 1.

Figure 23. External pressure coefficient distributions.

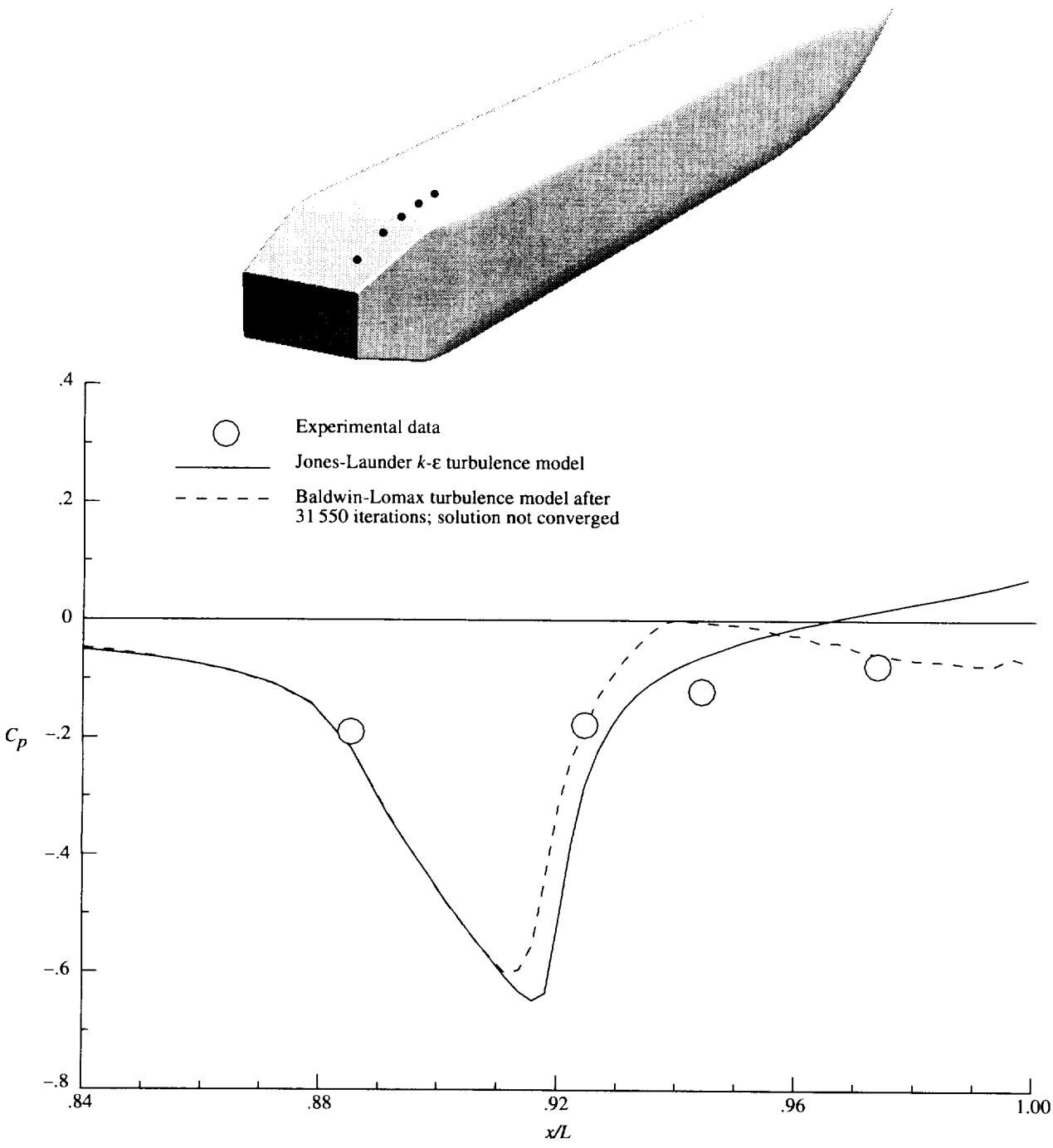

(b) $M_\infty = 0.938$; NPR = 4.017; and row 2.

Figure 23. Continued.

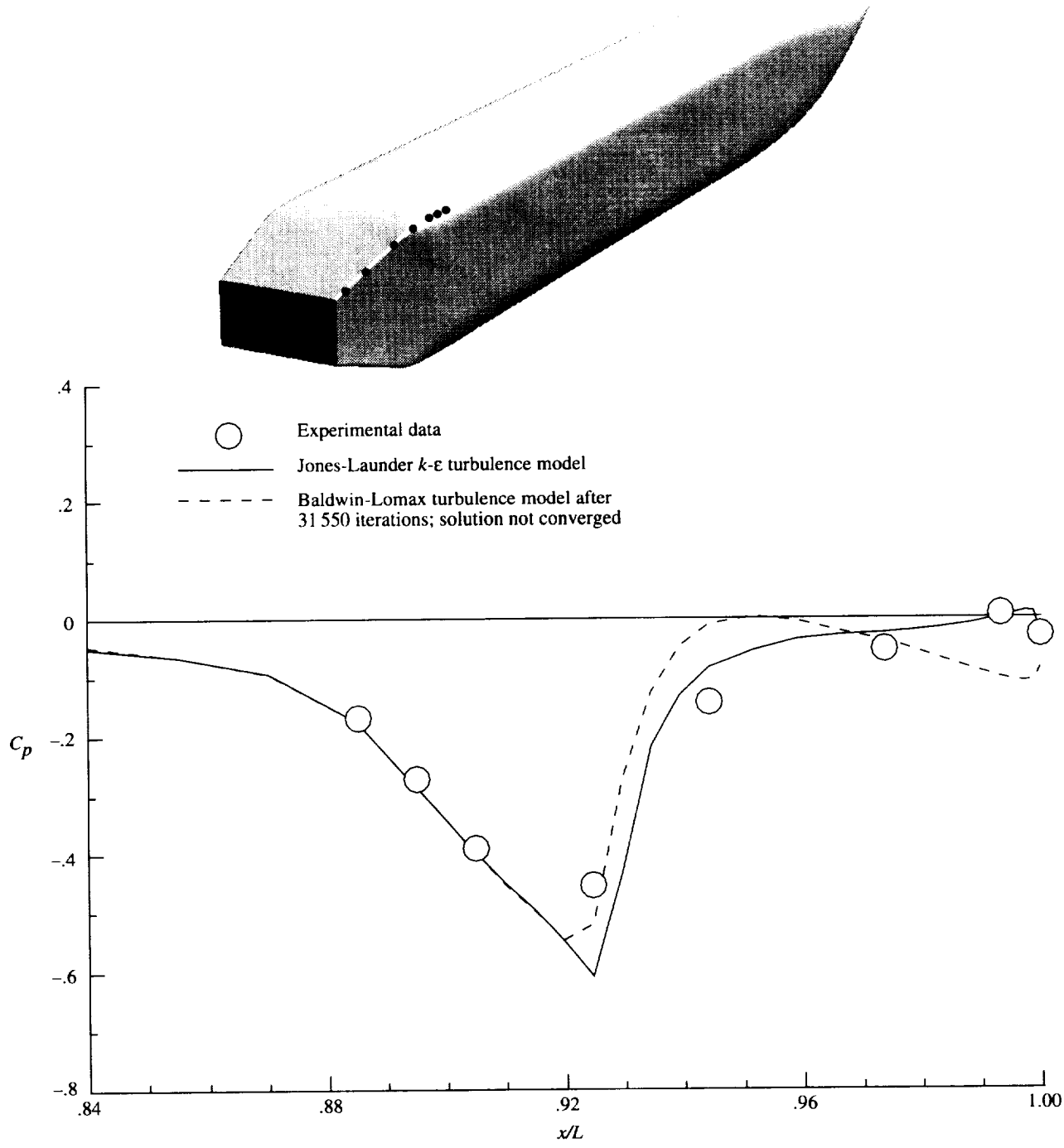

(c) $M_\infty = 0.938$; NPR = 4.017; and row 3.

Figure 23. Continued.

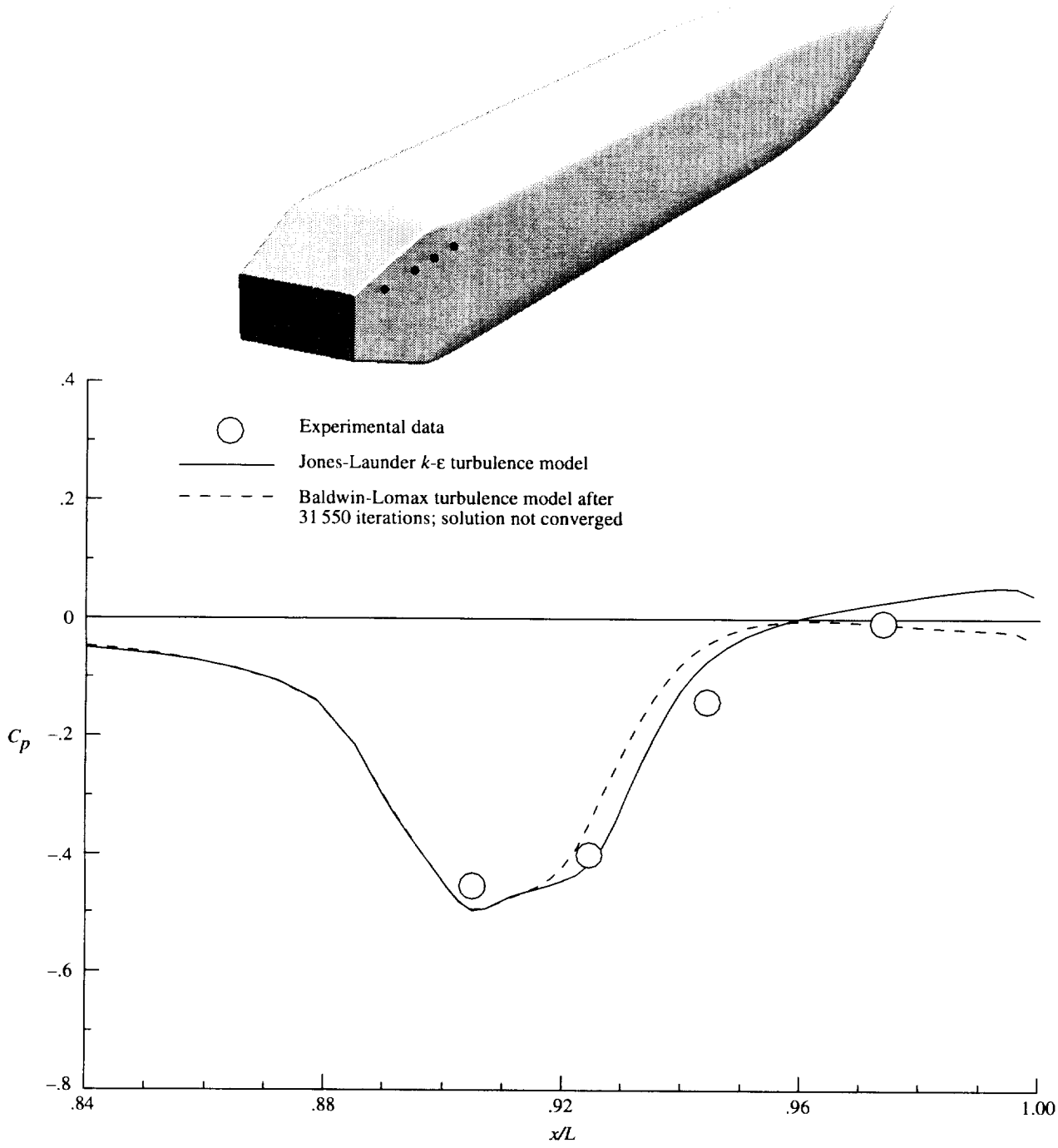

(d) $M_\infty = 0.938$; NPR = 4.017; and row 4.

Figure 23. Continued.

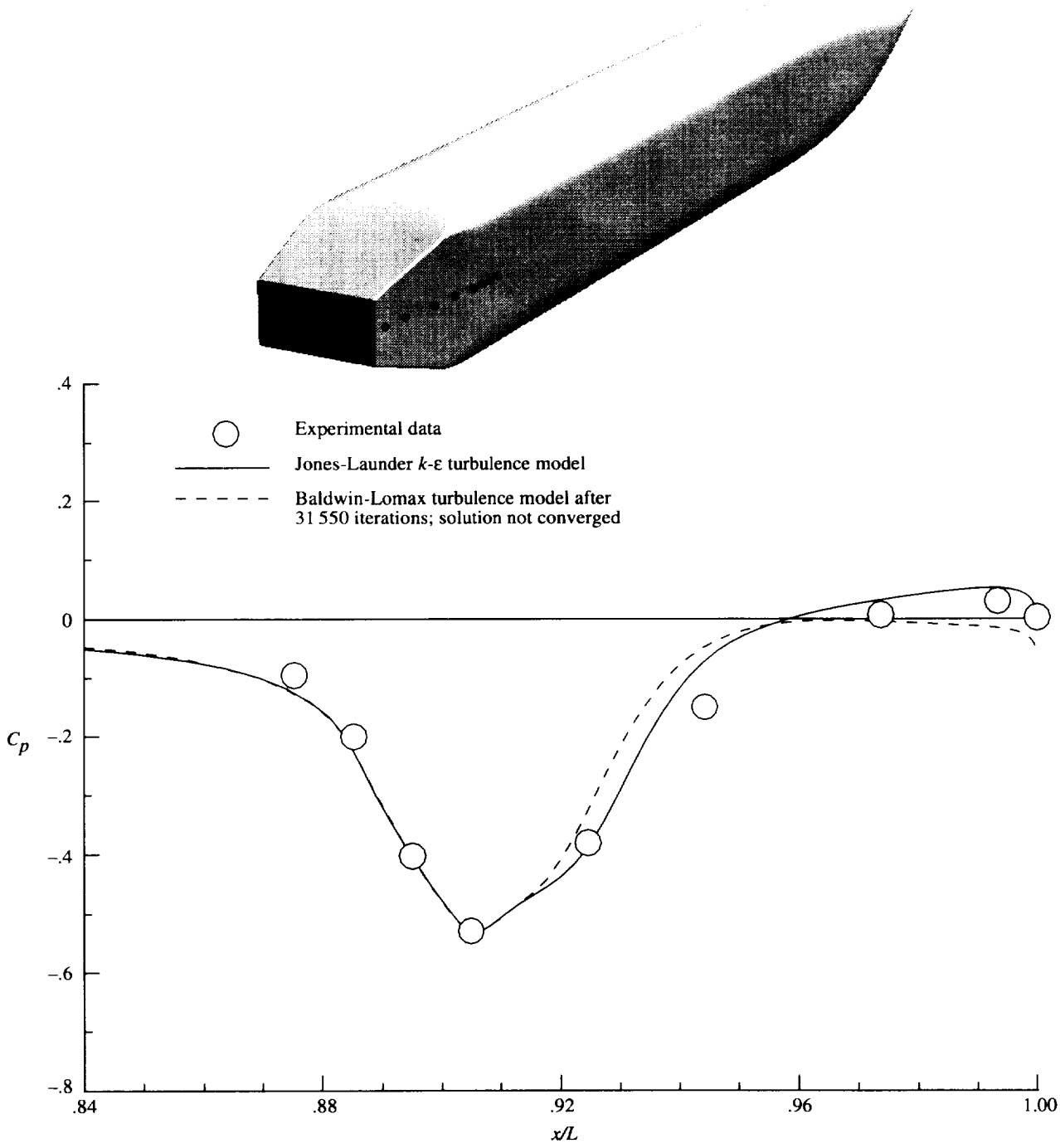

(e) $M_\infty = 0.938$; NPR = 4.017; and row 5.

Figure 23. Concluded.

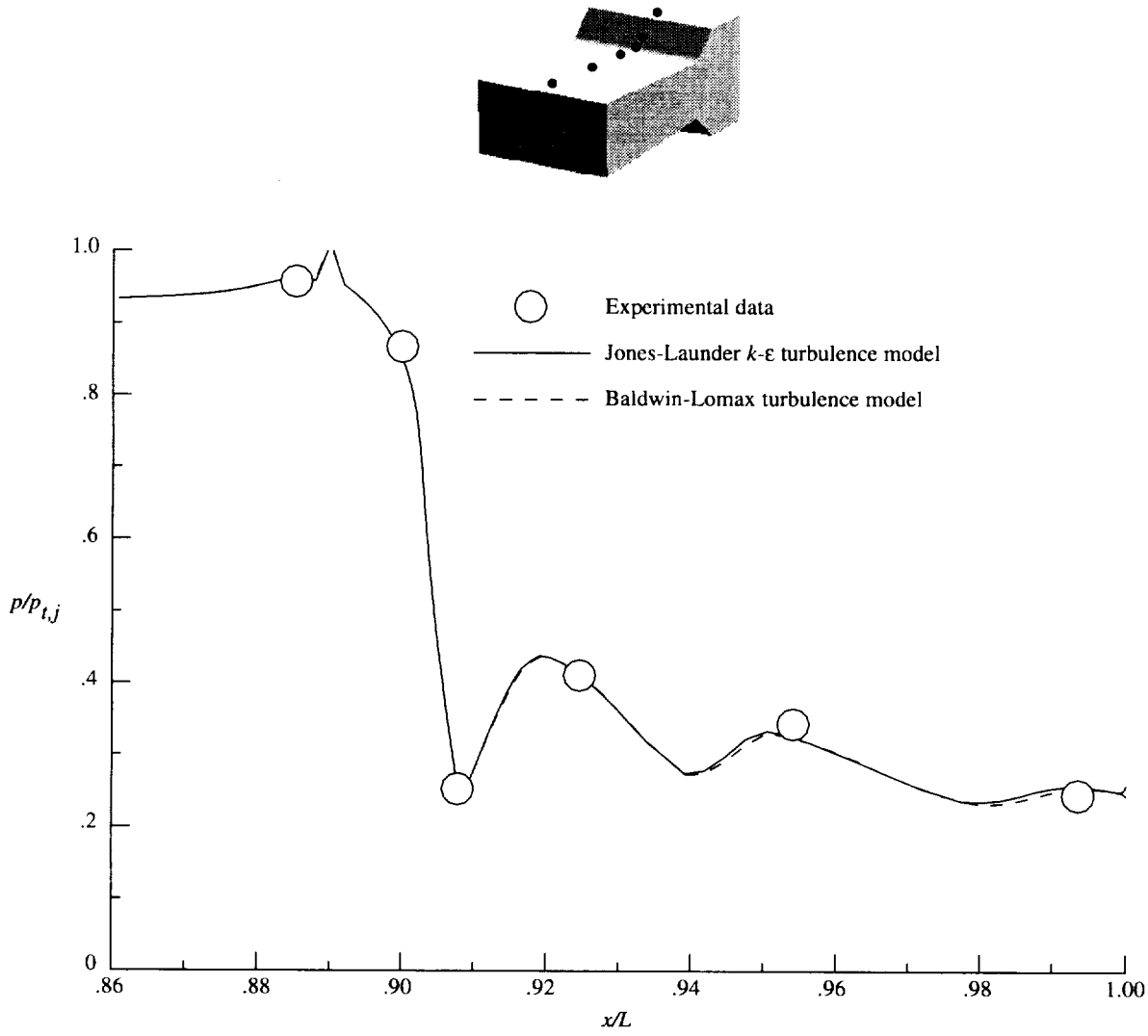

(a) $M_\infty = 0.938$; NPR = 4.017; and row 6.

Figure 24. Internal static pressure ratio distributions.

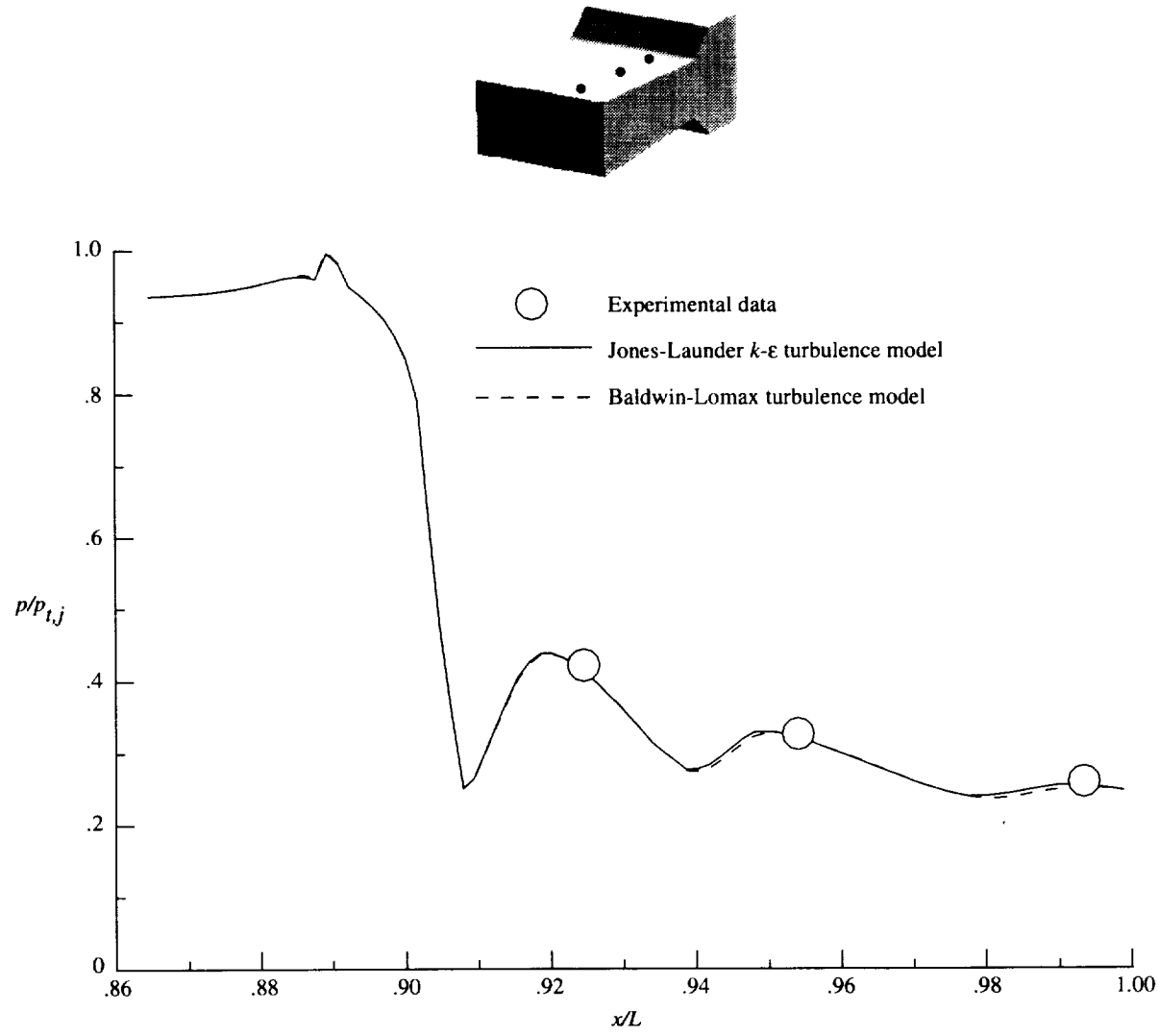

(b) $M_\infty = 0.938$; NPR = 4.017; and row 7.

Figure 24. Continued.

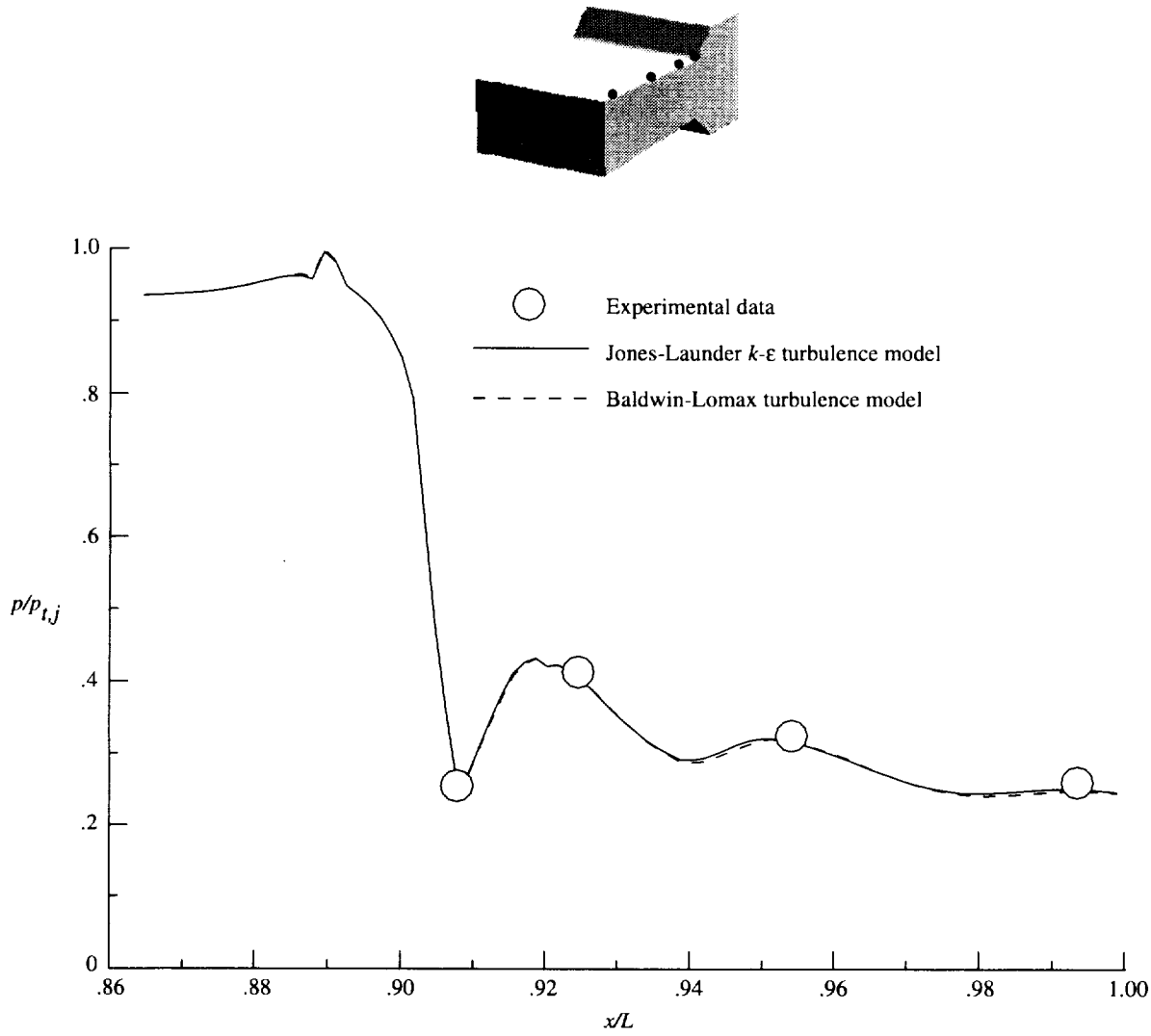

(c) $M_\infty = 0.938$; NPR = 4.017; and row 8.

Figure 24. Continued.

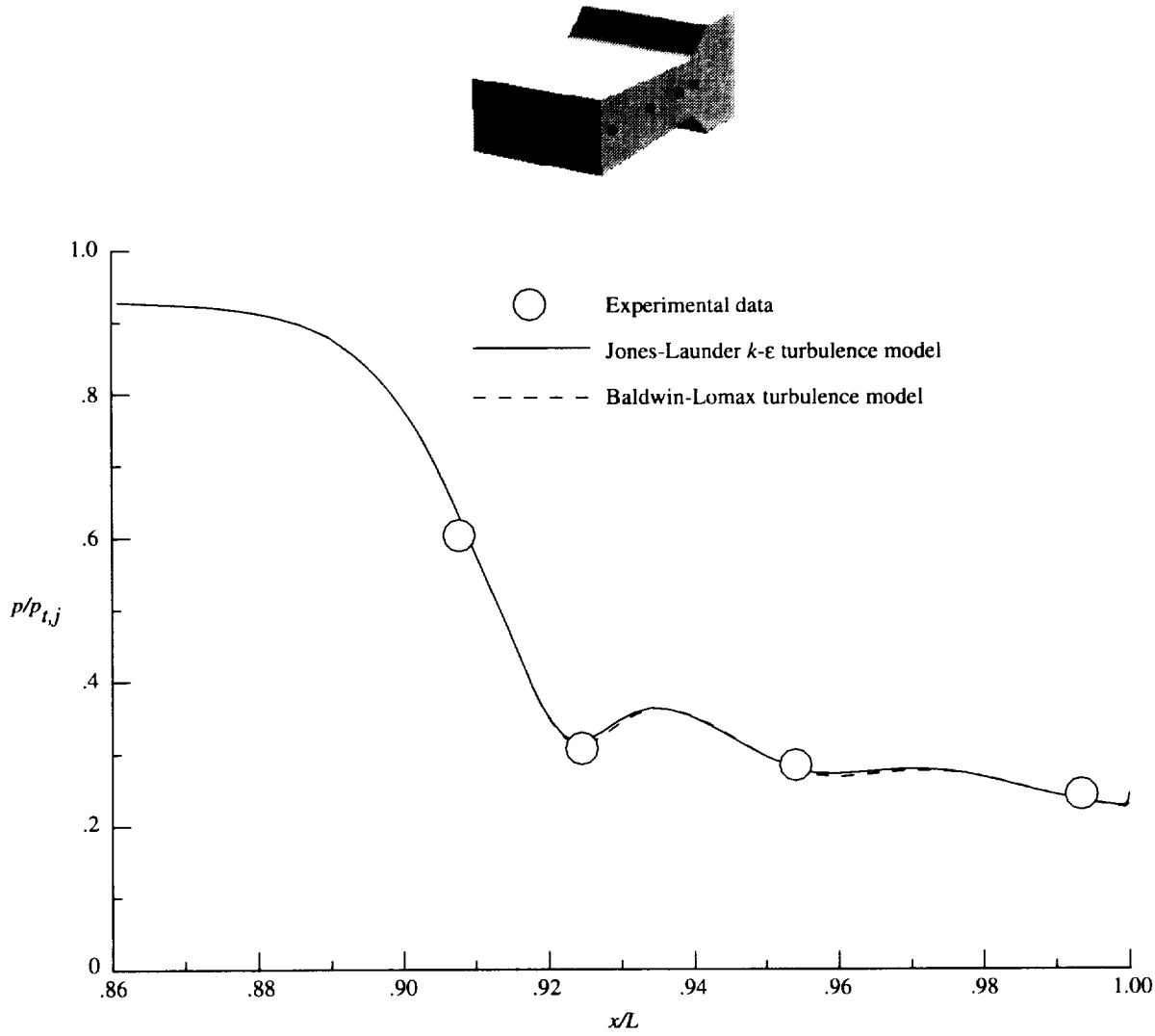

(d) $M_\infty = 0.938$; NPR = 4.017; and row 9.

Figure 24. Concluded.

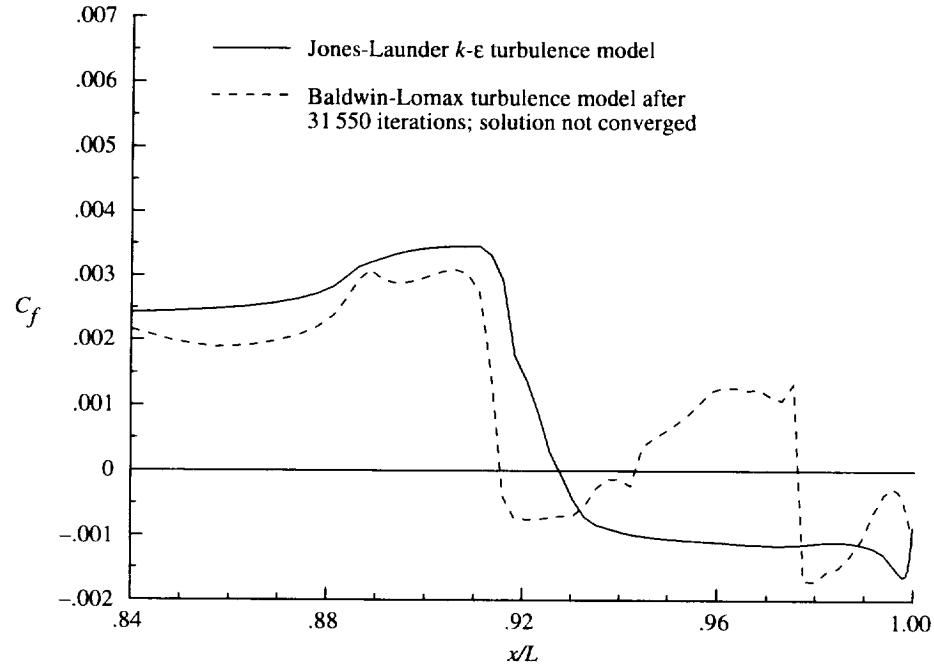

(a) $M_\infty = 0.938$; NPR = 4.017; and row 1 (external surface).

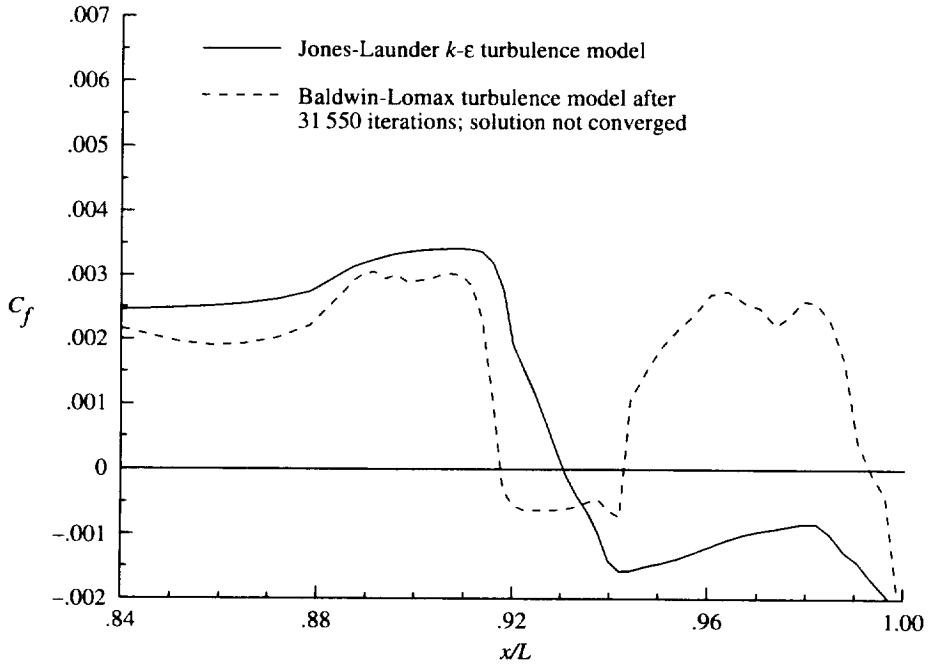

(b) $M_\infty = 0.938$; NPR = 4.017; and row 2 (external surface).

Figure 25. Skin-friction coefficient distributions.

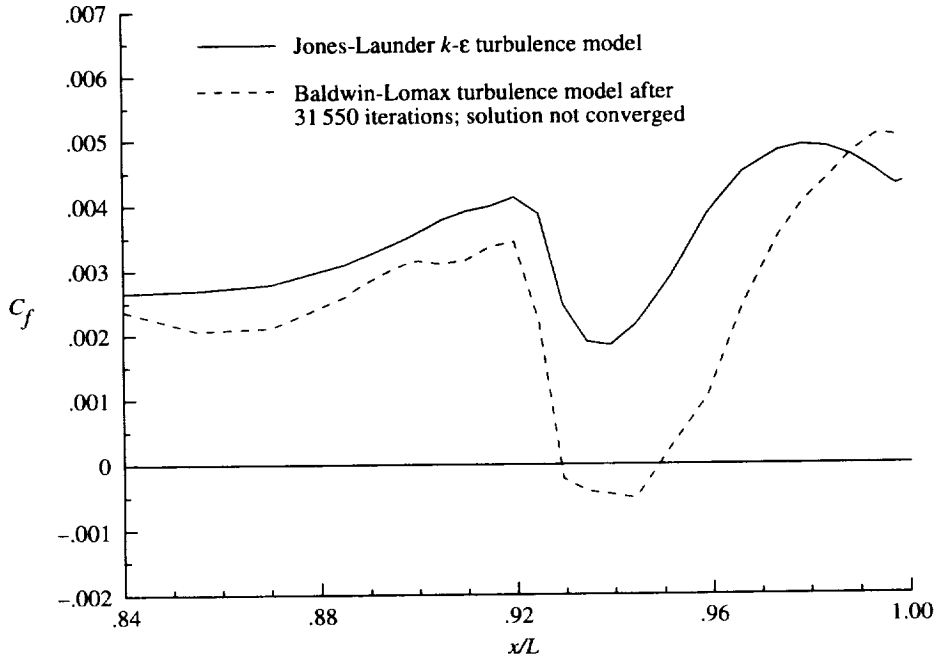

(c) $M_\infty = 0.938$; NPR = 4.017; and row 3 (external surface).

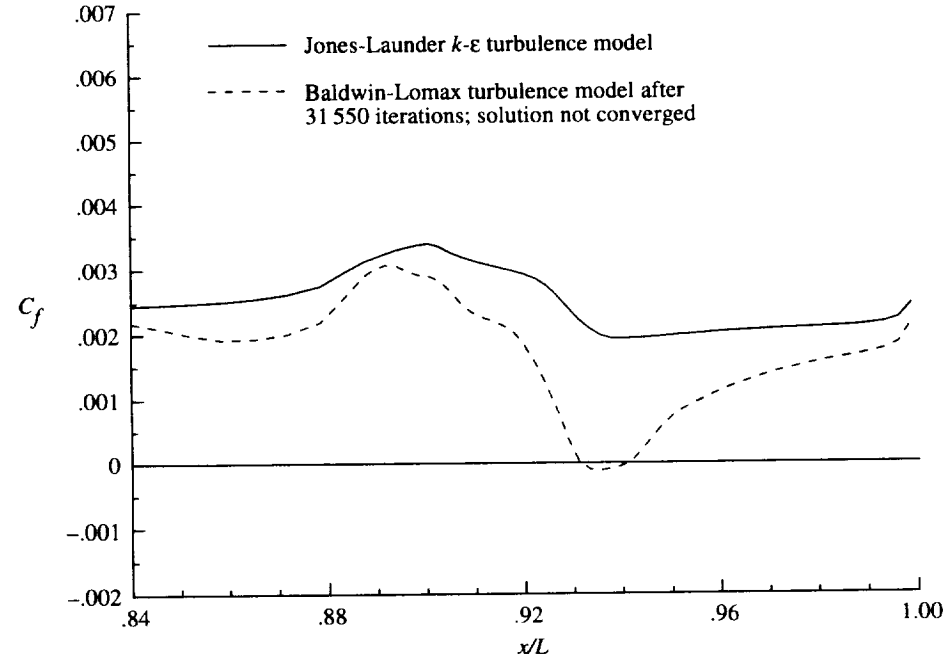

(d) $M_\infty = 0.938$; NPR = 4.017; and row 4 (external surface).

Figure 25. Continued.

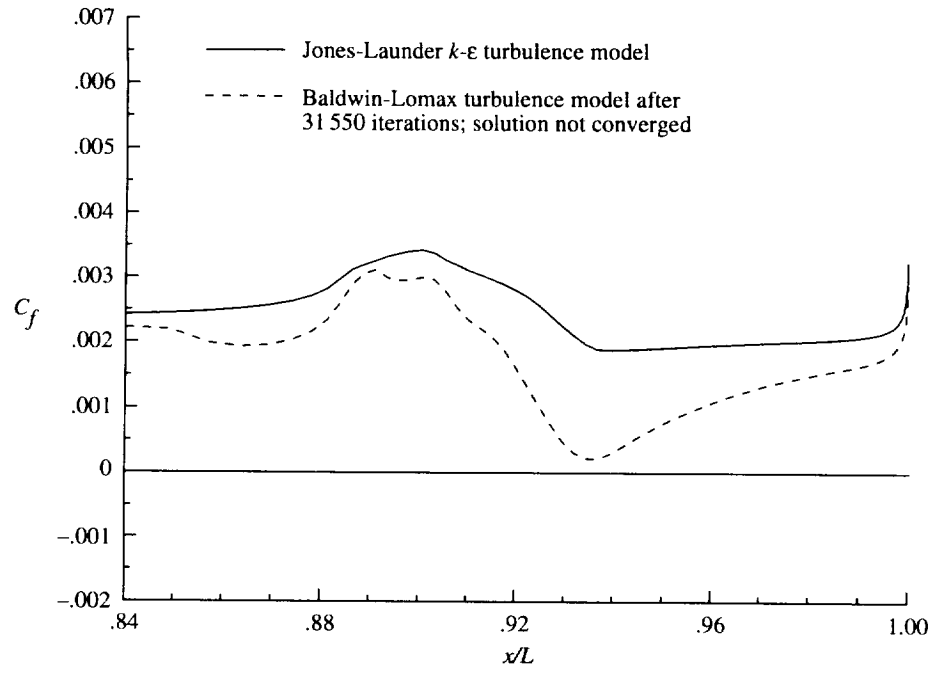

(e) $M_\infty = 0.938$; NPR = 4.017; and row 5 (external surface).

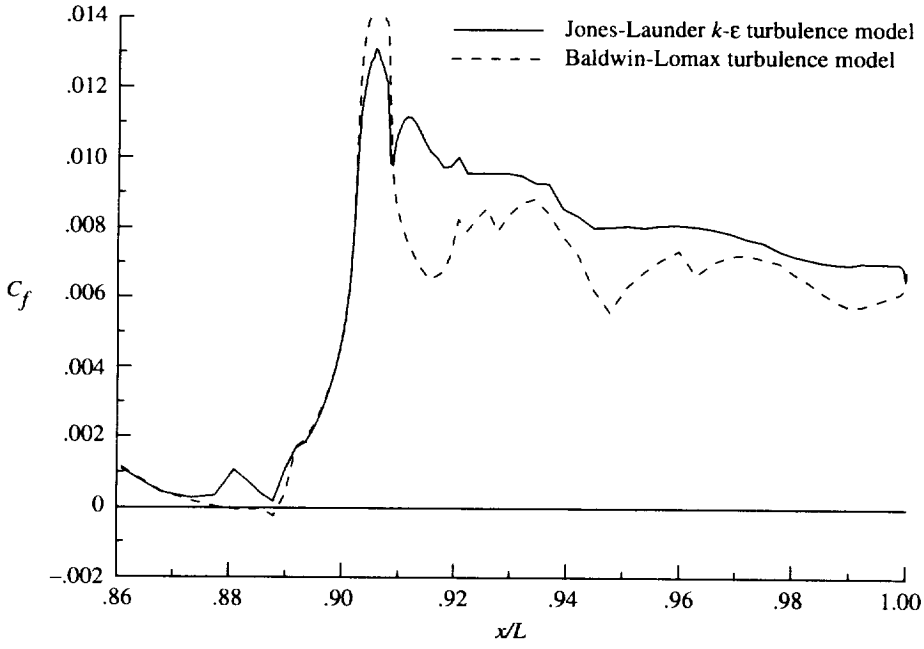

(f) $M_\infty = 0.938$; NPR = 4.017; and row 6 (internal surface).

Figure 25. Continued.

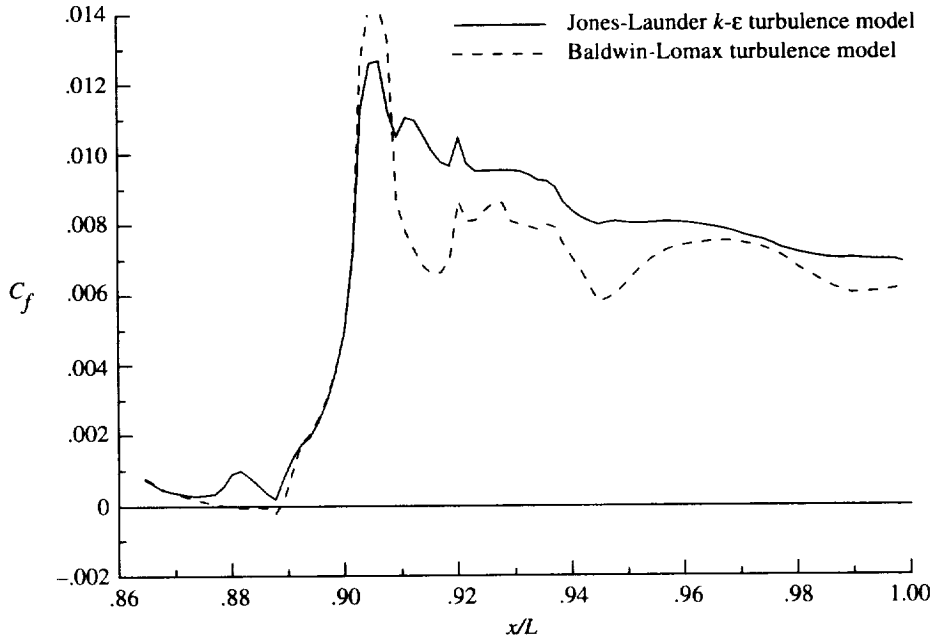

(g) $M_\infty = 0.938$; NPR = 4.017; and row 7 (internal surface).

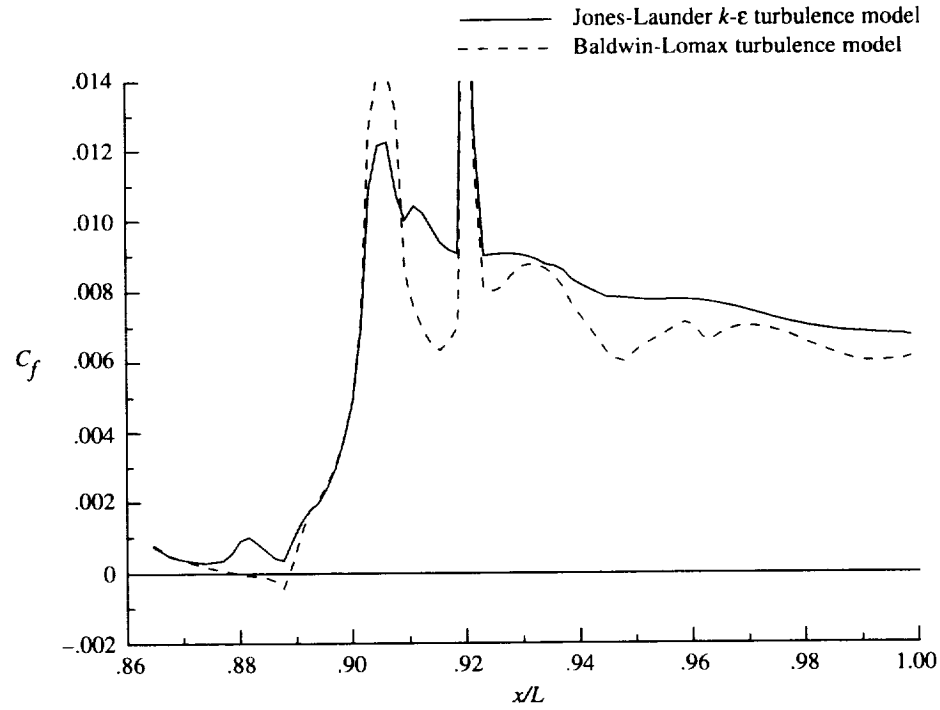

(h) $M_\infty = 0.938$; NPR = 4.017; and row 8 (internal surface).

Figure 25. Continued.

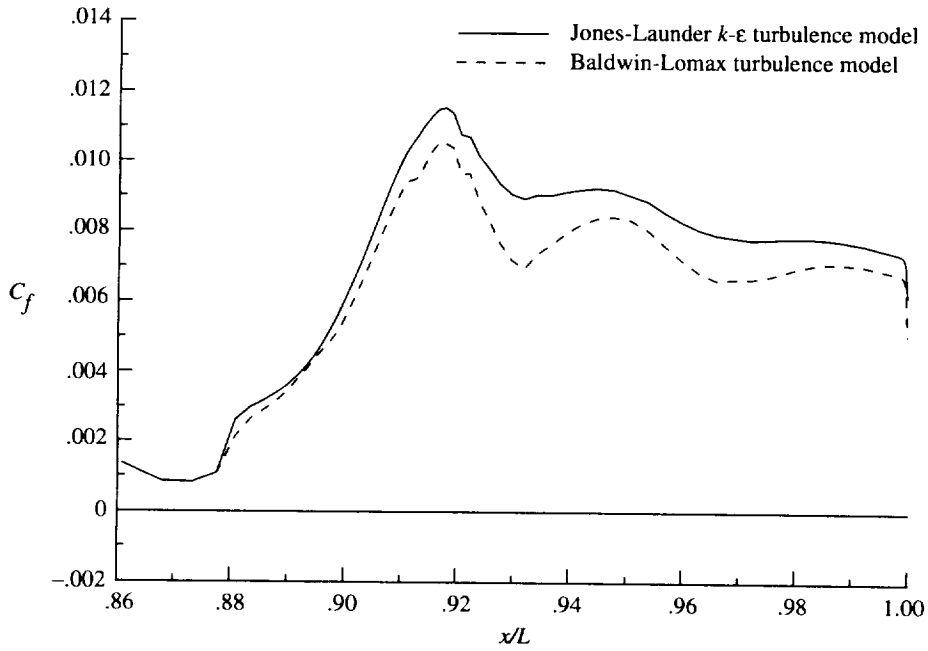

(i) $M_\infty = 0.938$; NPR = 4.017; and row 9 (internal surface).

Figure 25. Concluded.

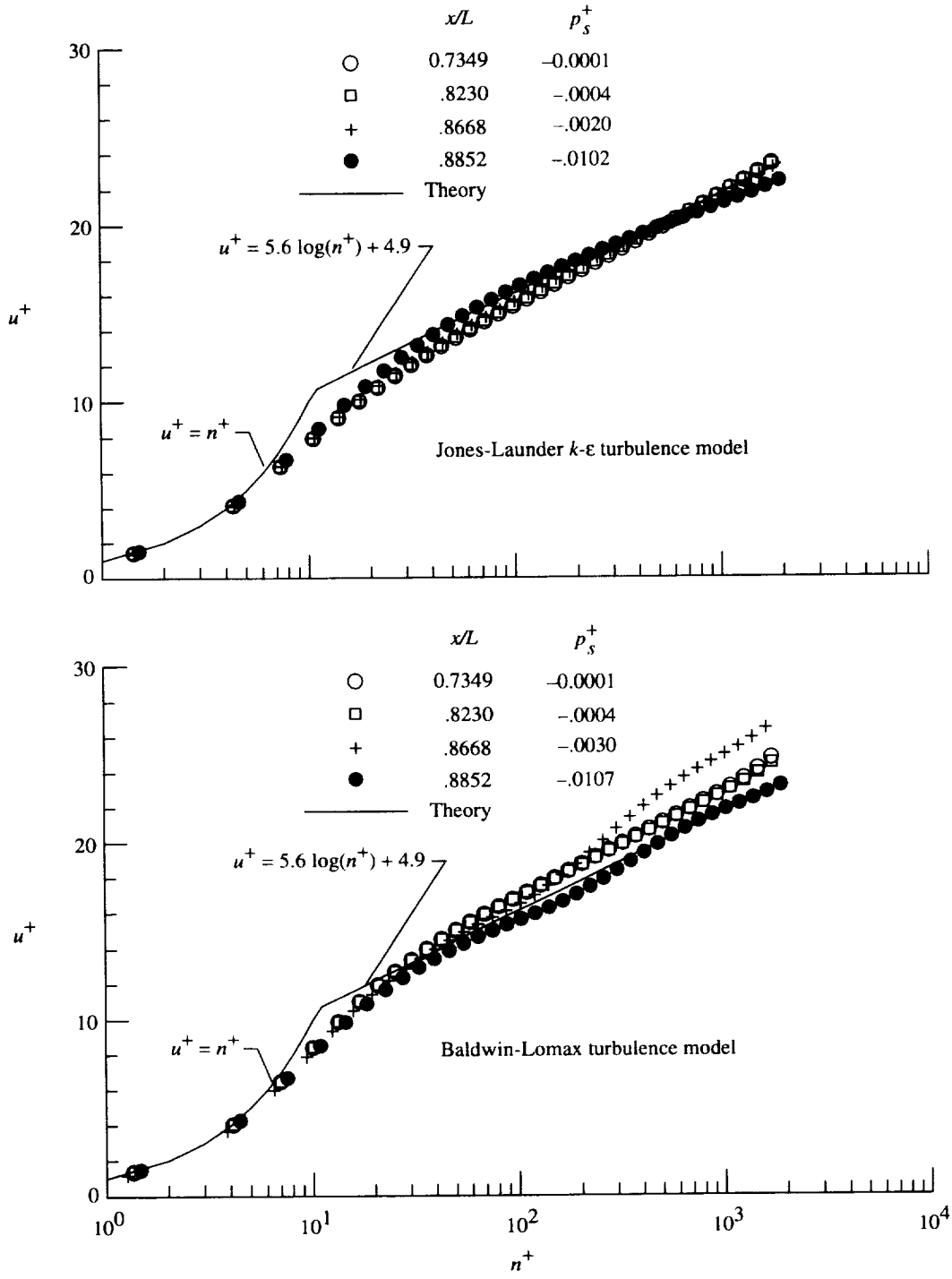

(a) $\phi = 0°$ (top row).

Figure 26. Universal law-of-the-wall boundary layer profiles at $M_\infty = 0.938$.

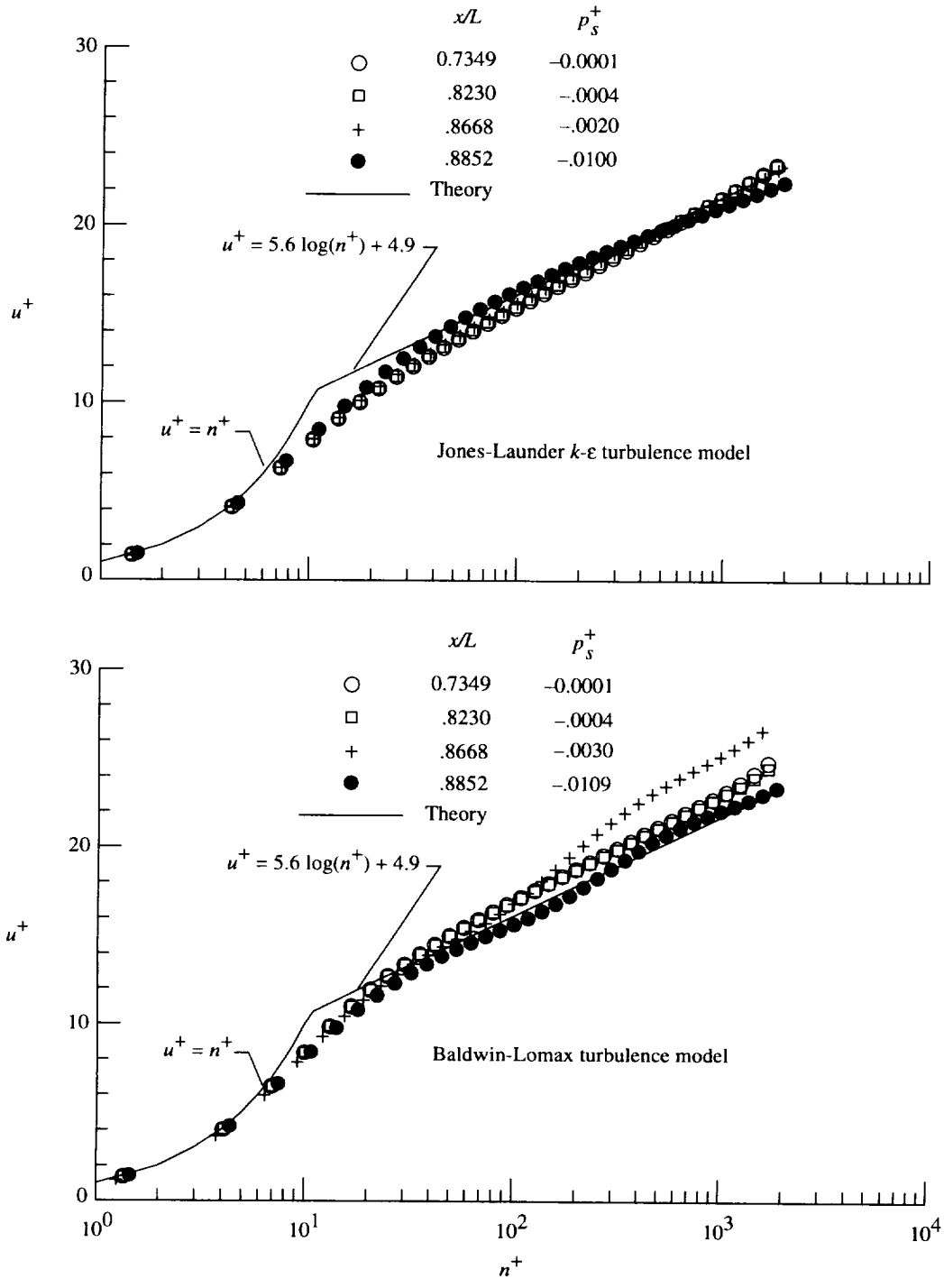

(b) $\phi = 90°$ (side row).

Figure 26. Concluded.

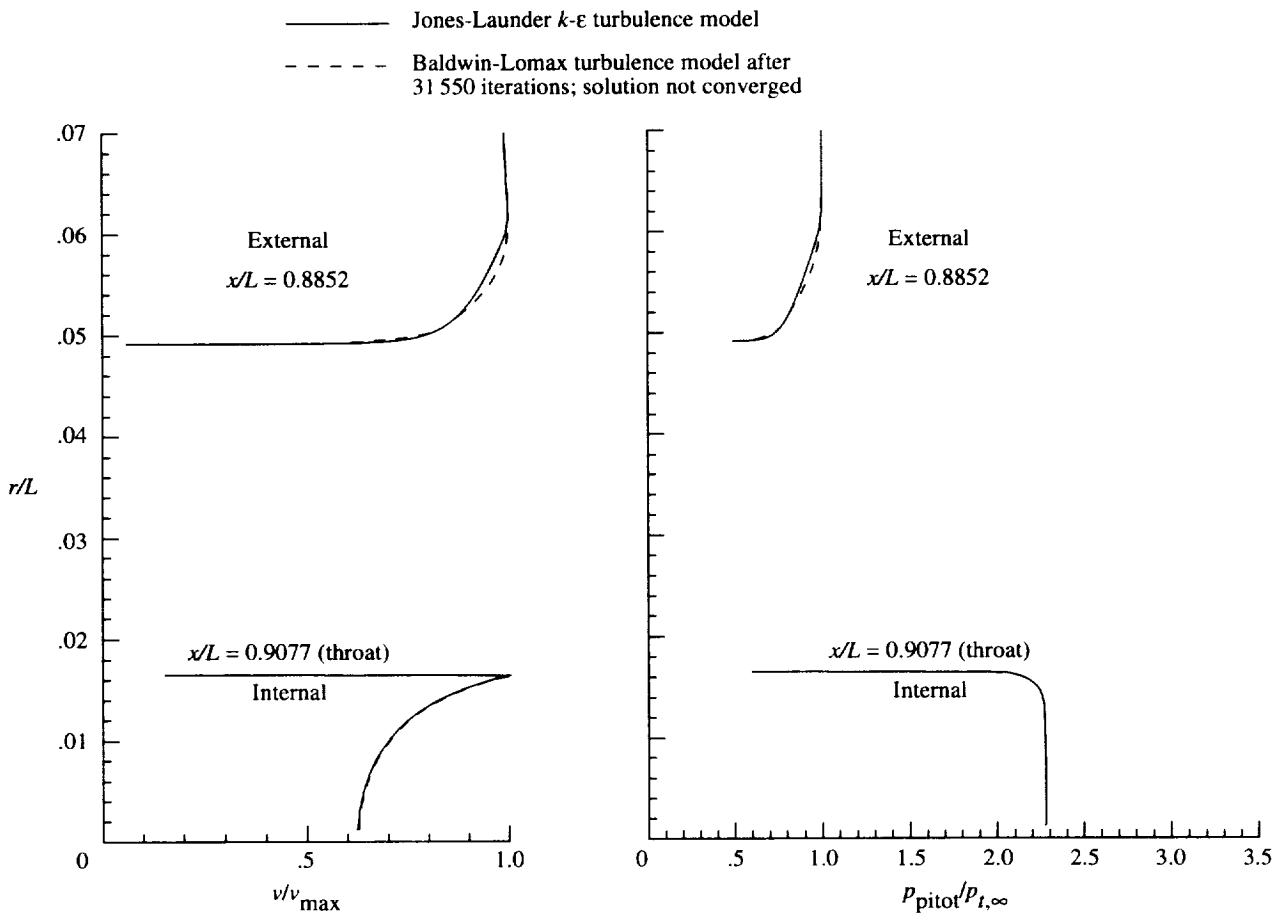

(a) $\phi = 0°$.

Figure 27. Boundary layer profiles at $M_\infty = 0.938$.

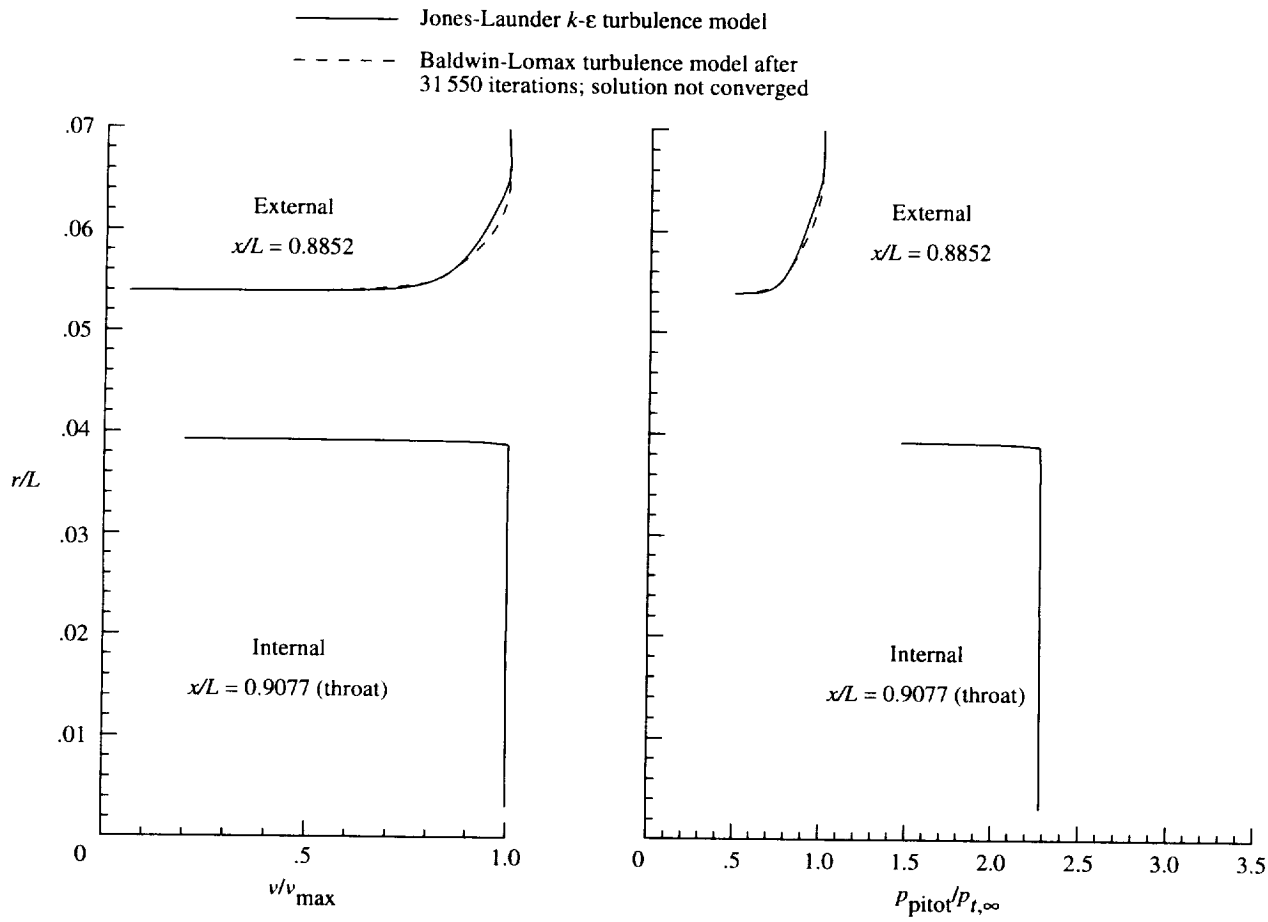

(b) $\phi = 90°$.

Figure 27. Continued.

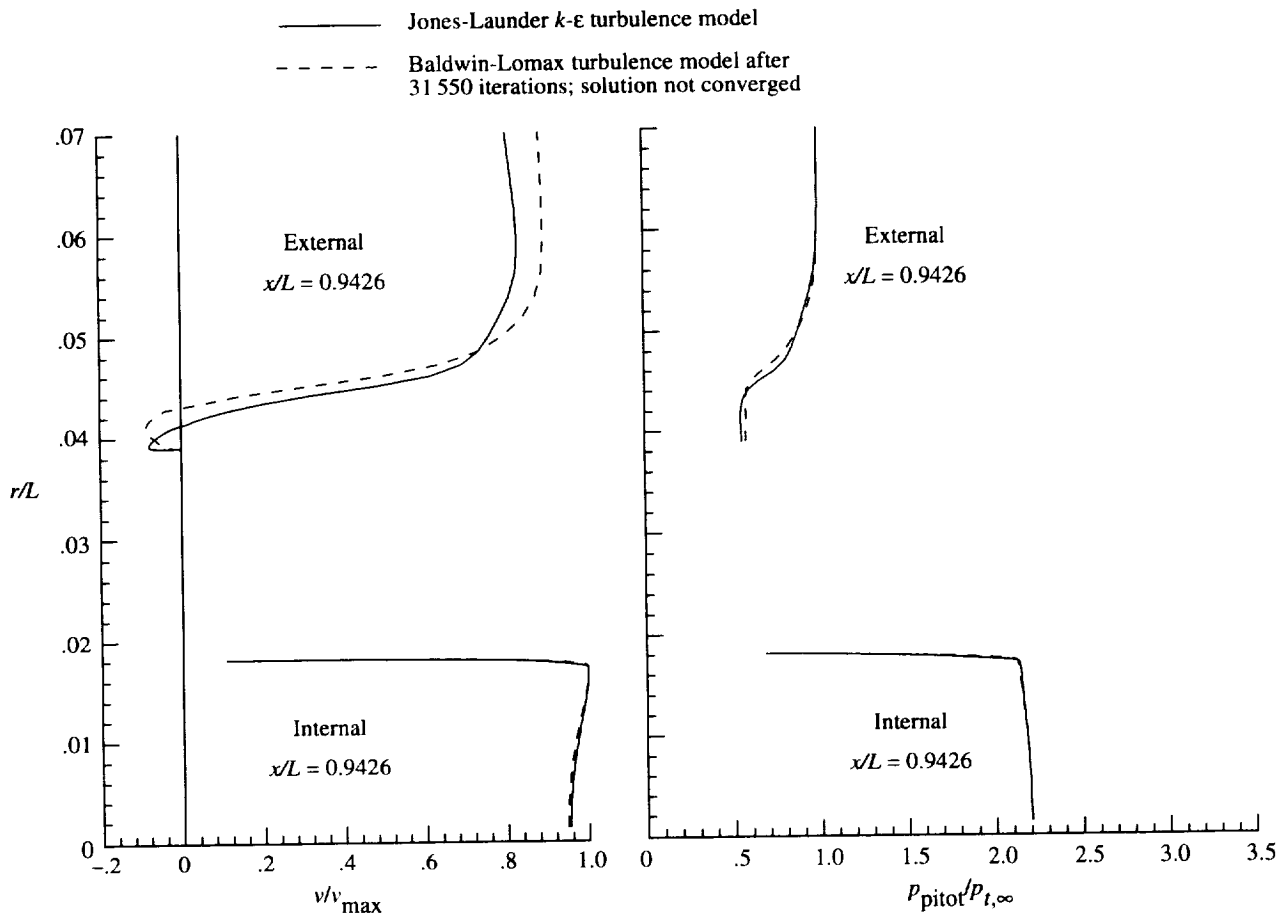

(c) $\phi = 0°$.

Figure 27. Continued.

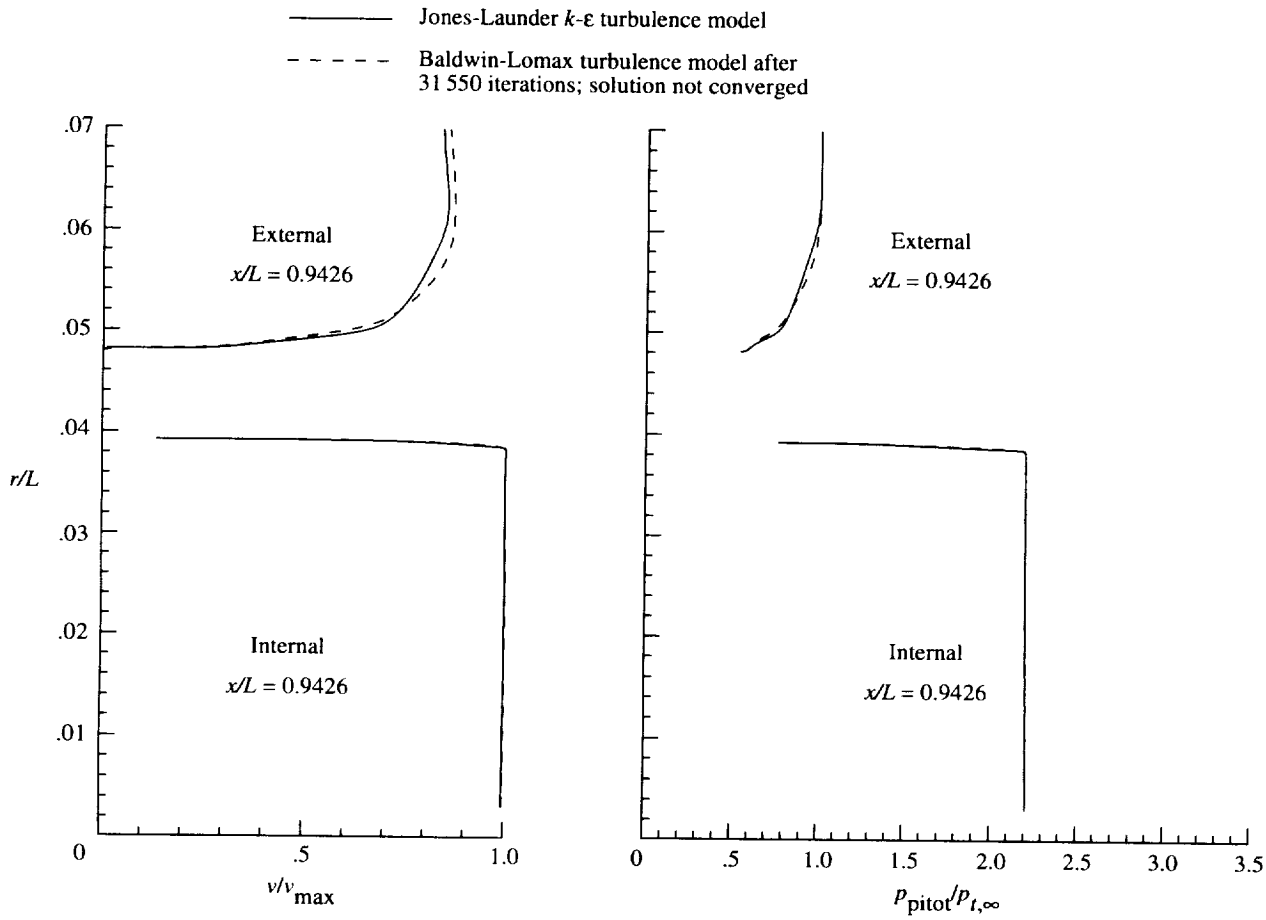

(d) $\phi = 90°$.

Figure 27. Continued.

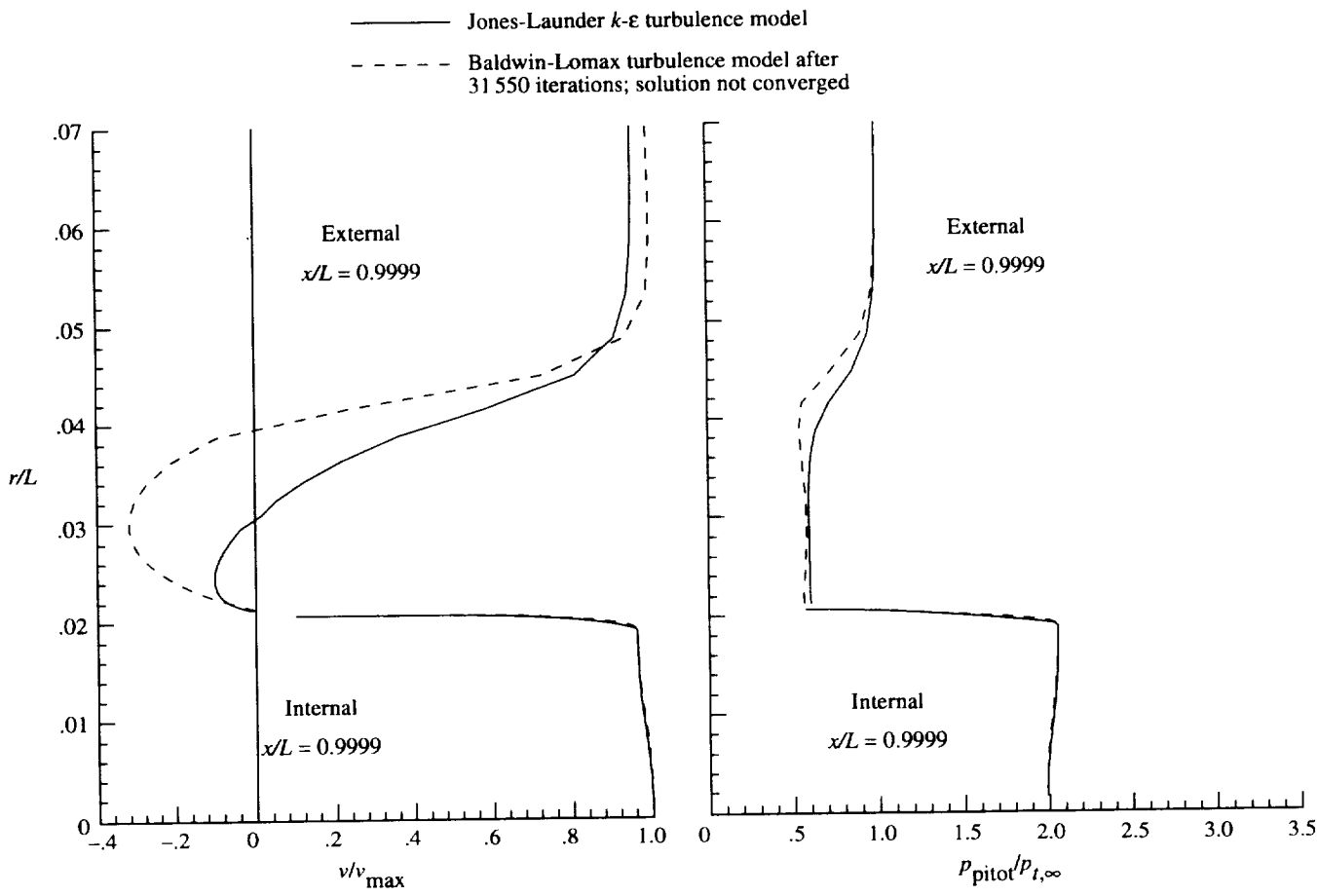

(e) $\phi = 0°$.

Figure 27. Continued.

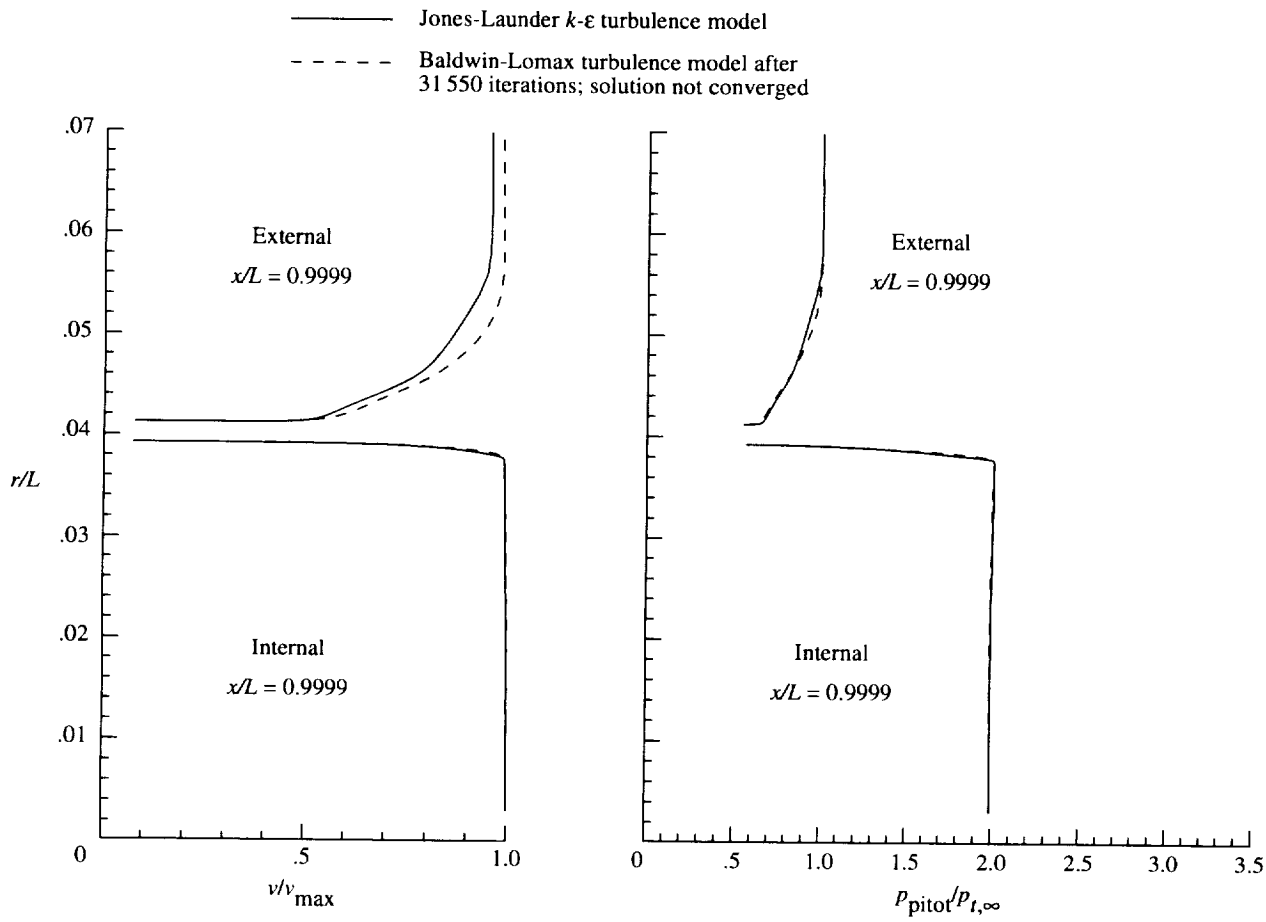

(f) $\phi = 90°$.

Figure 27. Concluded.

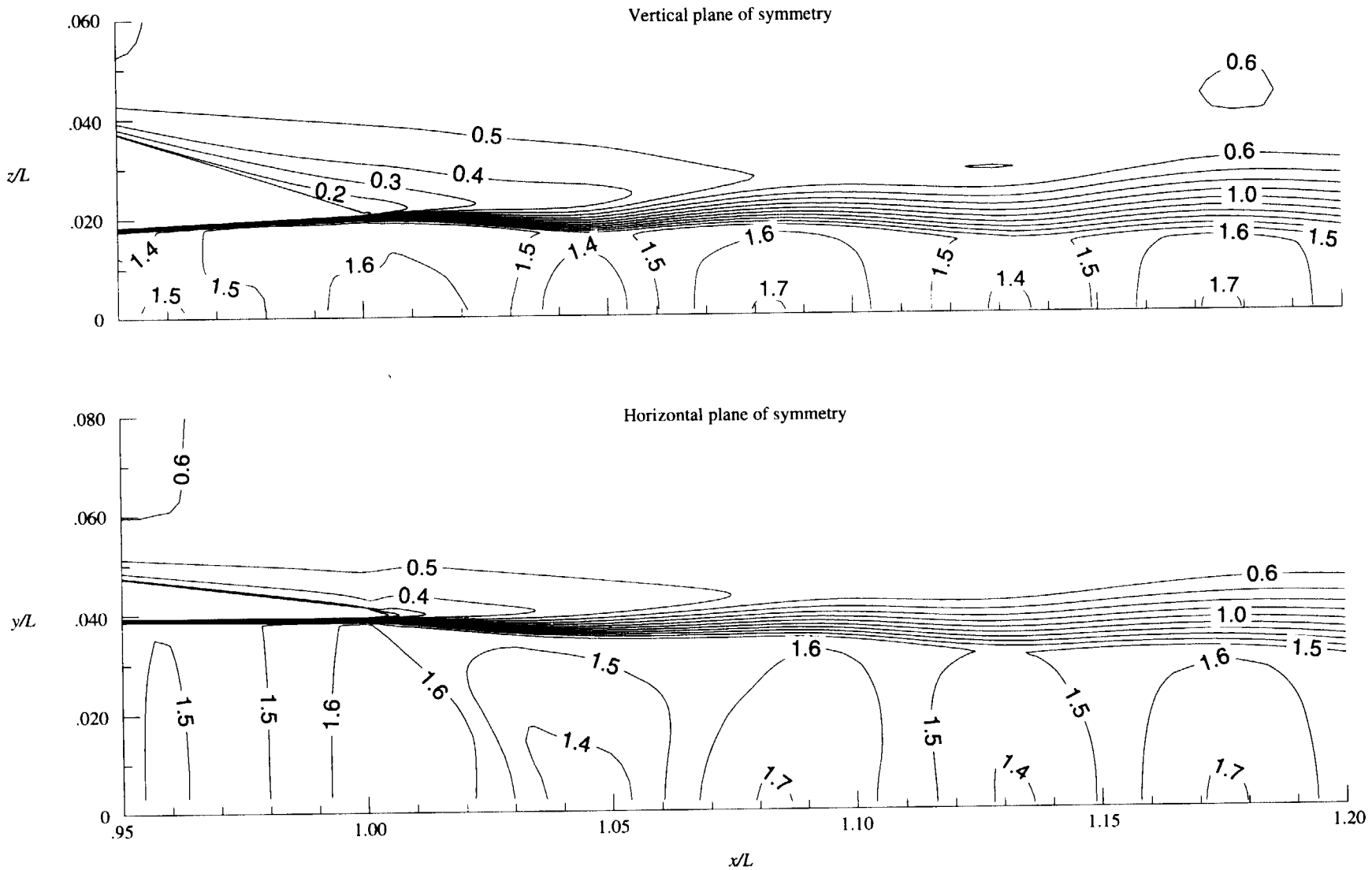

Figure 28. Mach number contours in jet plume. M_∞ = 0.600; NPR = 4.003; Jones-Launder k-ε turbulence model; and contour increment = 0.1.

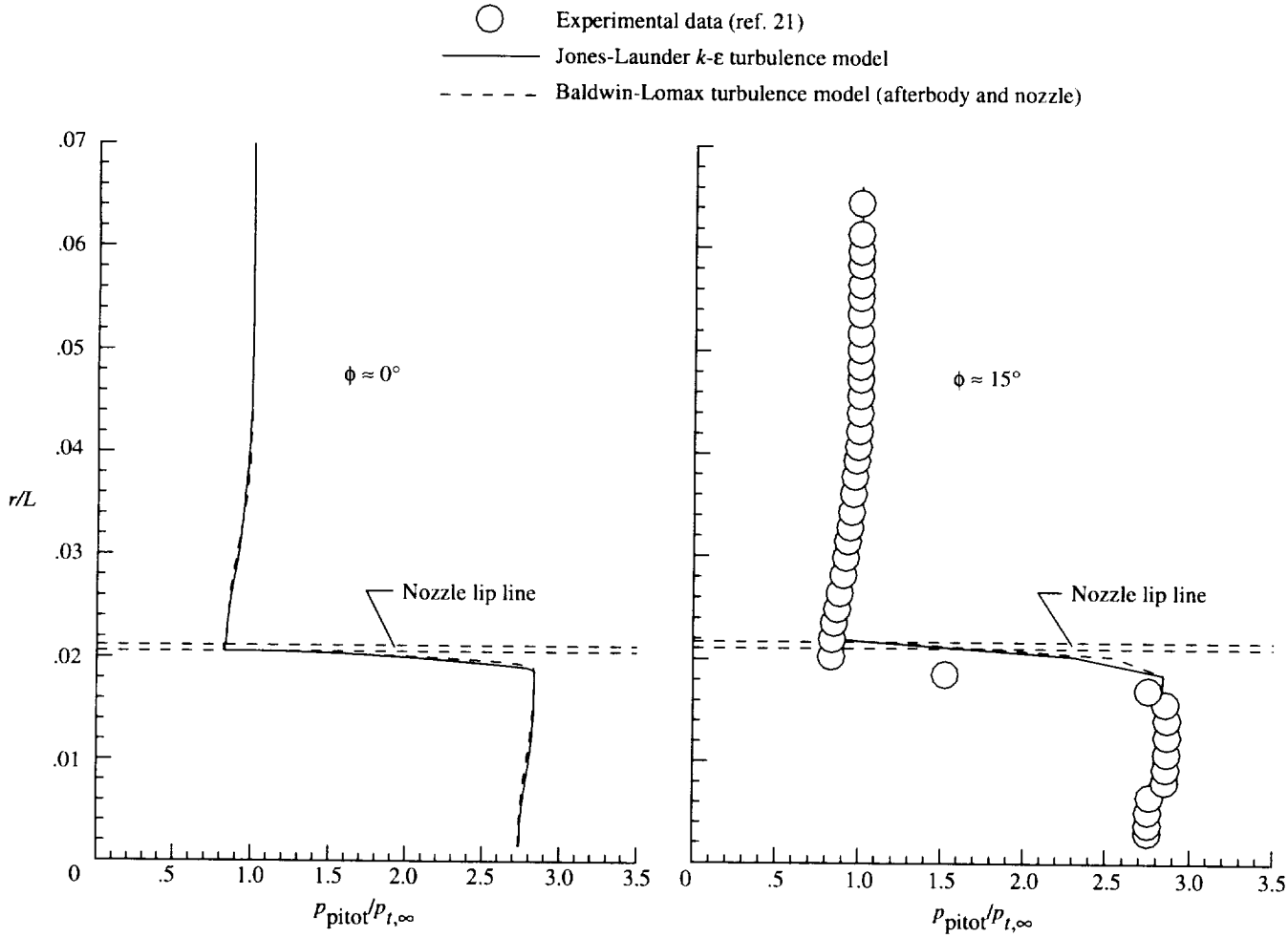

(a) $x/L = 1.000$.

Figure 29. Pitot pressure ratio distributions in jet plume at $M_\infty = 0.600$.

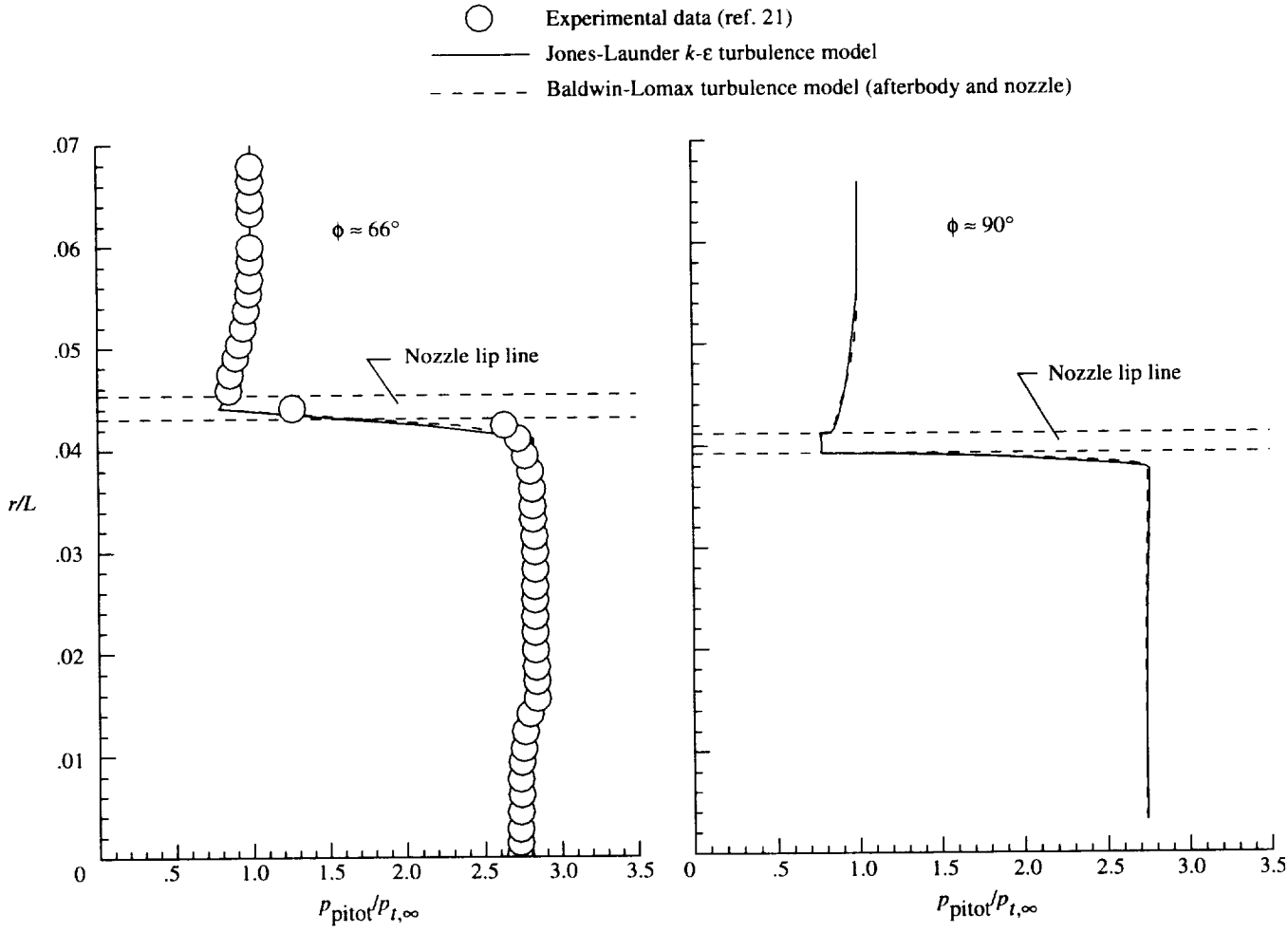

(b) $x/L = 1.000$.

Figure 29. Continued.

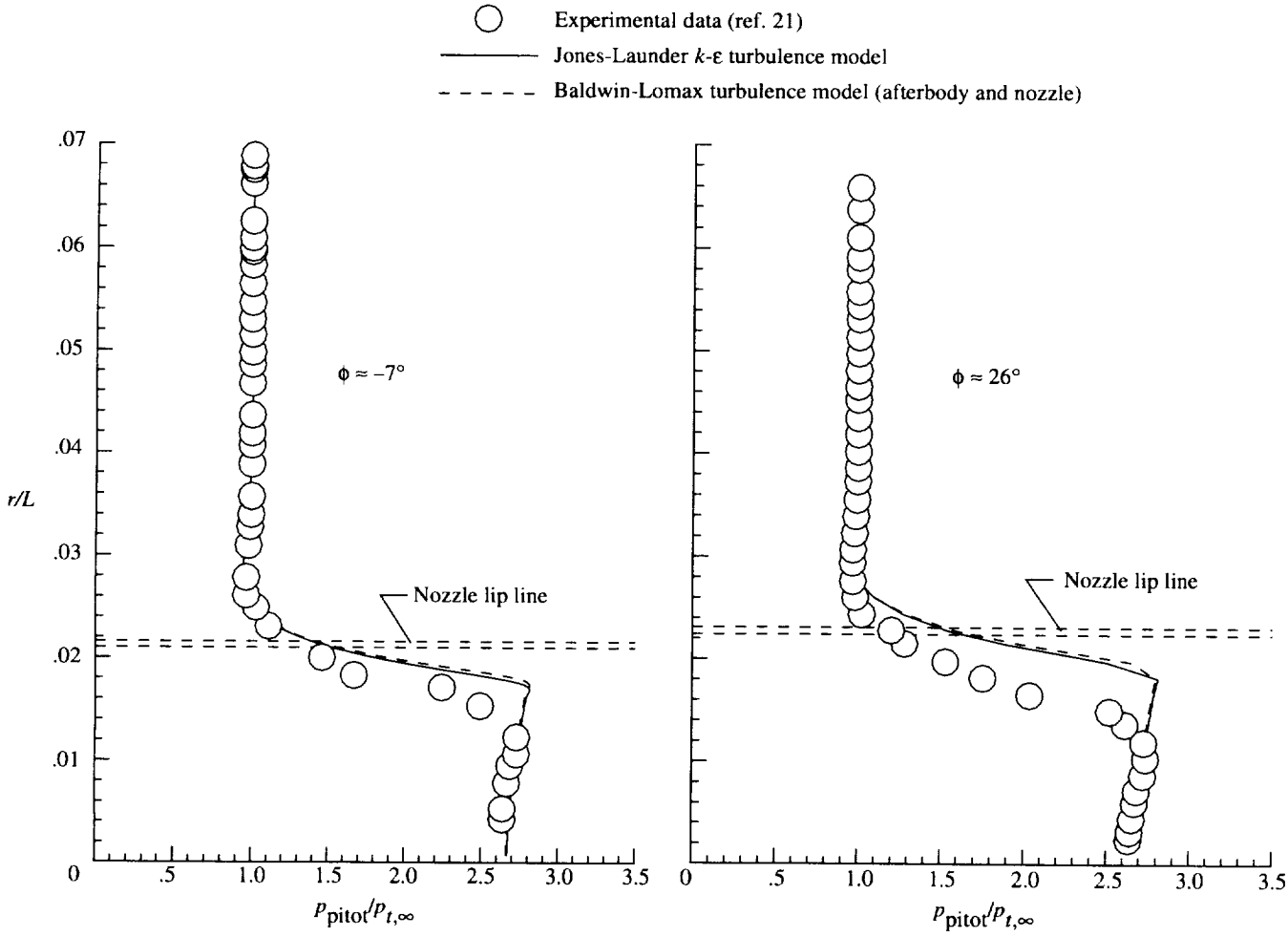

(c) $x/L = 1.081$.

Figure 29. Continued.

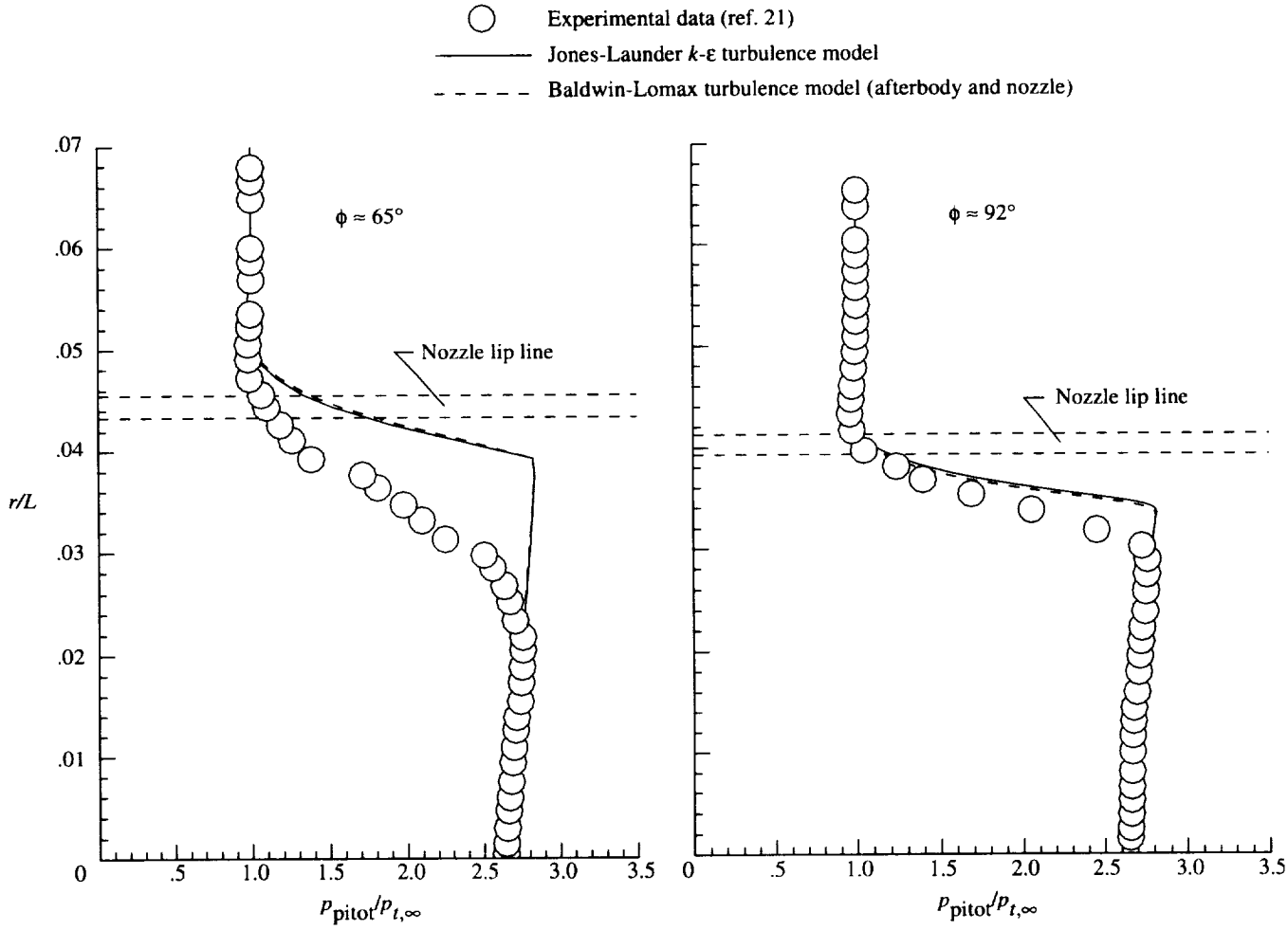

(d) $x/L = 1.081$.

Figure 29. Continued.

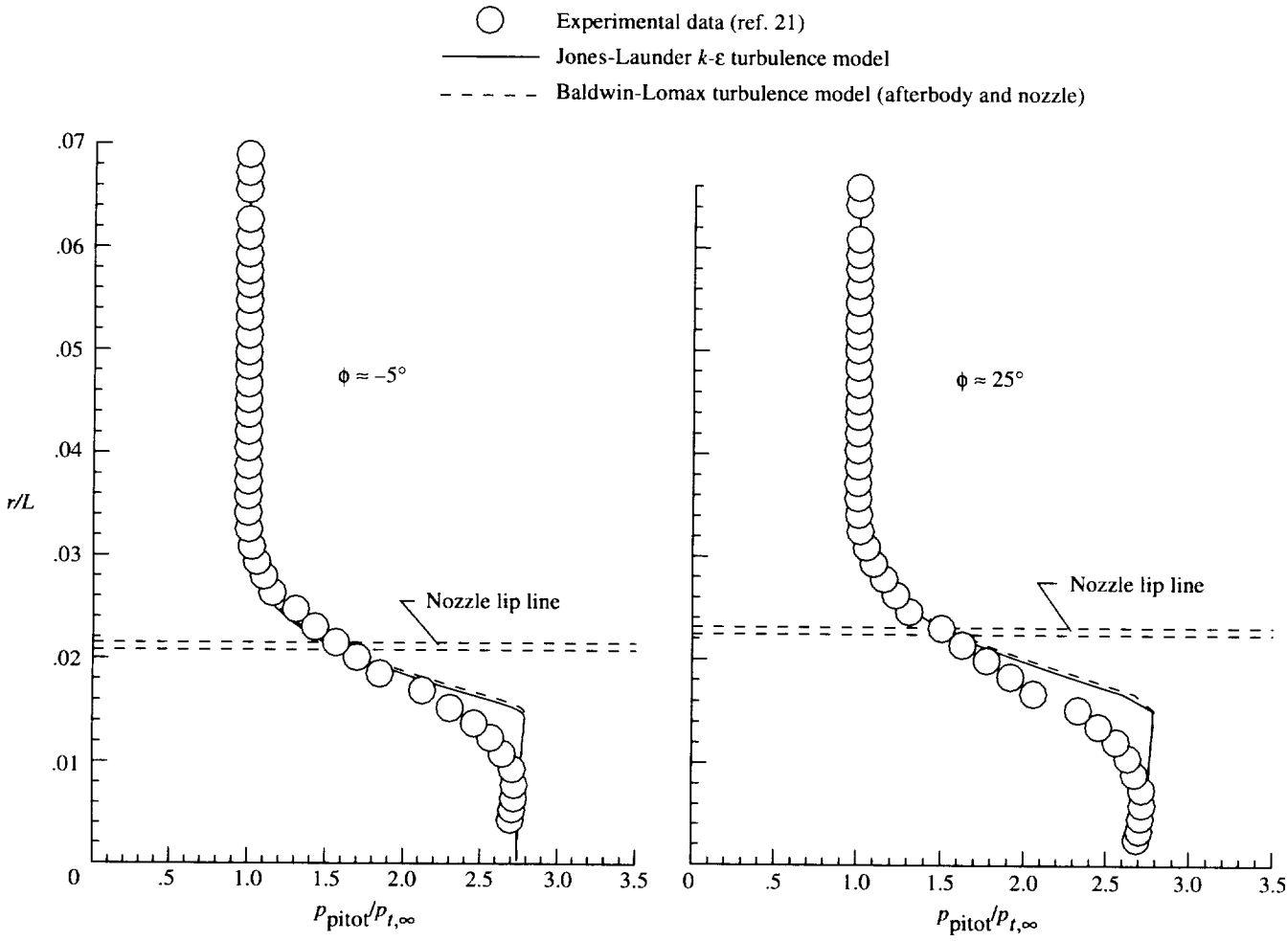

(e) $x/L = 1.162$.

Figure 29. Continued.

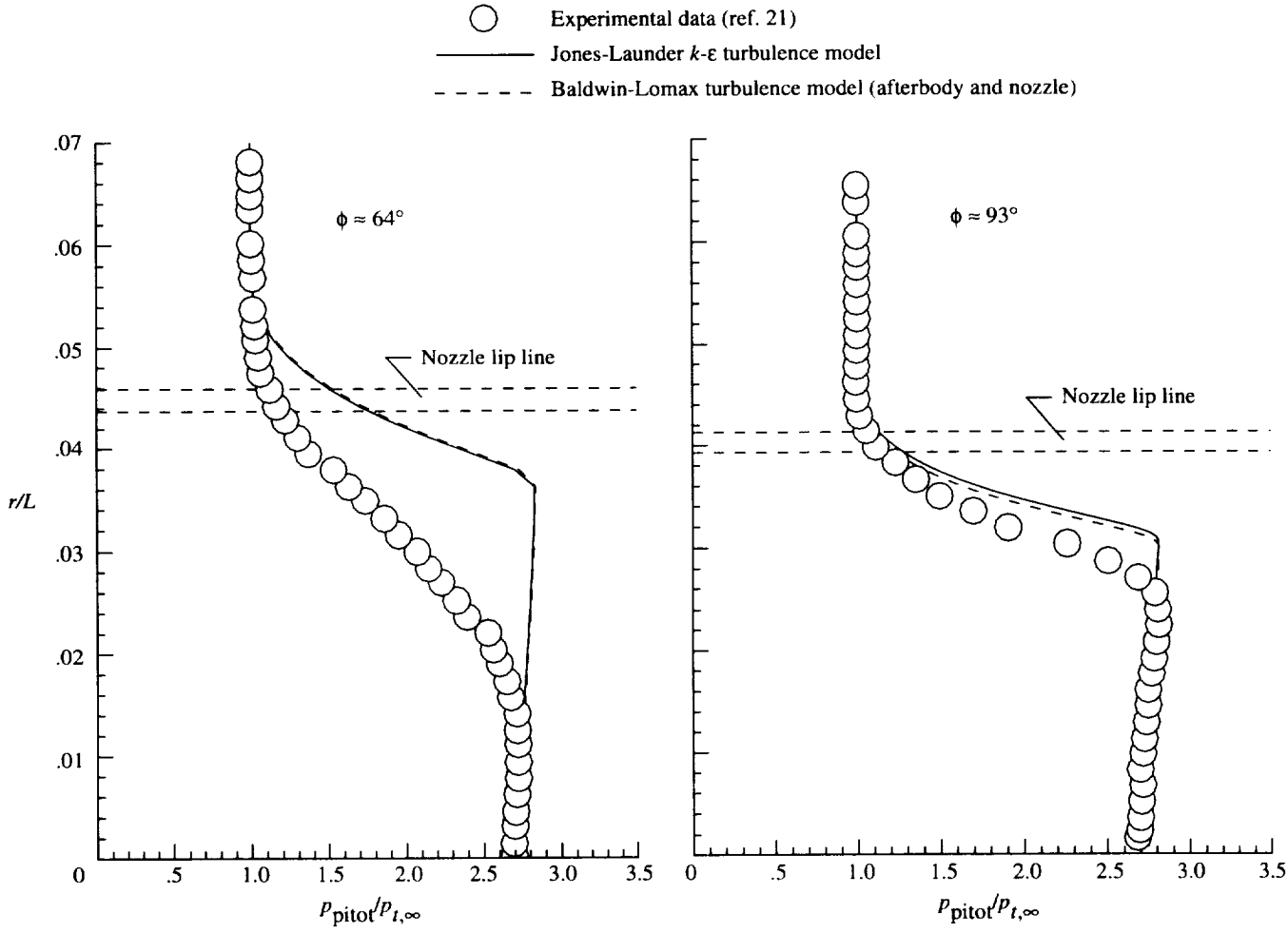

(f) $x/L = 1.162$.

Figure 29. Concluded.

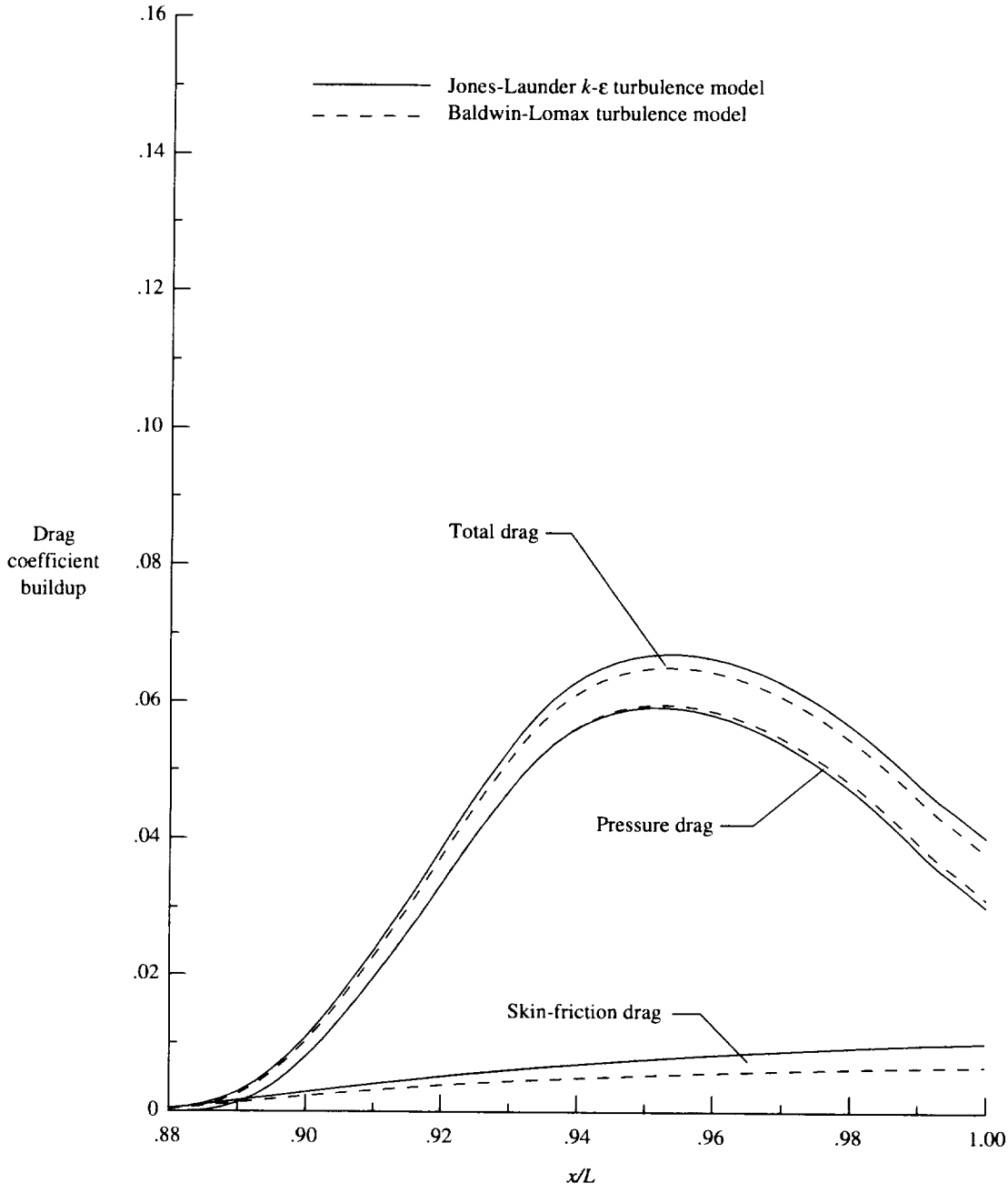

(a) $M_\infty = 0.600$.

Figure 30. Afterbody-drag coefficient buildup.

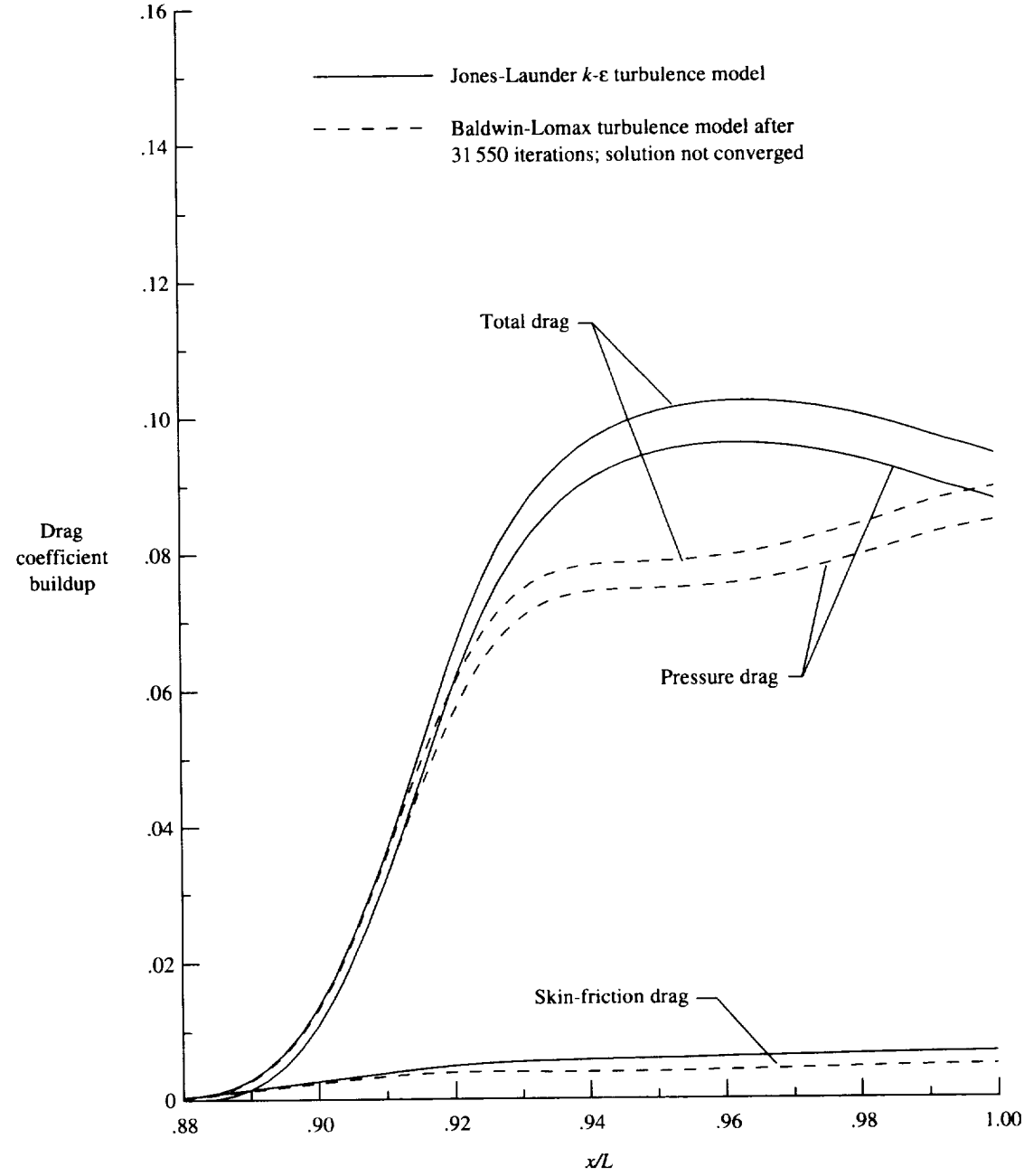

(b) $M_\infty = 0.938$.

Figure 30. Concluded.

REPORT DOCUMENTATION PAGE

Form Approved
OMB No. 0704-0188

1. AGENCY USE ONLY *(Leave blank)*	2. REPORT DATE	3. REPORT TYPE AND DATES COVERED
	September 1996	Technical Paper

4. TITLE AND SUBTITLE
Comparison of Turbulence Models for Nozzle-Afterbody Flows With Propulsive Jets

5. FUNDING NUMBERS
WU 505-59-70-04

6. AUTHOR(S)
William B. Compton III

7. PERFORMING ORGANIZATION NAME(S) AND ADDRESS(ES)
NASA Langley Research Center
Hampton, VA 23681-0001

8. PERFORMING ORGANIZATION REPORT NUMBER
L-17506

9. SPONSORING/MONITORING AGENCY NAME(S) AND ADDRESS(ES)
National Aeronautics and Space Administration
Washington, DC 20546-0001

10. SPONSORING/MONITORING AGENCY REPORT NUMBER
NASA TP-3592

11. SUPPLEMENTARY NOTES

12a. DISTRIBUTION/AVAILABILITY STATEMENT
Unclassified–Unlimited
Subject Category 02
Availability: NASA CASI (301) 621-0390

12b. DISTRIBUTION CODE

13. ABSTRACT *(Maximum 200 words)*
A numerical investigation was conducted to assess the accuracy of two turbulence models when computing nonaxisymmetric nozzle-afterbody flows with propulsive jets. Navier-Stokes solutions were obtained for a convergent-divergent nonaxisymmetric nozzle-afterbody and its associated jet exhaust plume at free-stream Mach numbers of 0.600 and 0.938 at an angle of attack of 0°. The Reynolds number based on model length was approximately 20×10^6. Turbulent dissipation was modeled by the algebraic Baldwin-Lomax turbulence model with the Degani-Schiff modification and by the standard Jones-Launder k-ε turbulence model. At flow conditions without strong shocks and with little or no separation, both turbulence models predicted the pressures on the surfaces of the nozzle very well. When strong shocks and massive separation existed, both turbulence models were unable to predict the flow accurately. Mixing of the jet exhaust plume and the external flow was underpredicted. The differences in drag coefficients for the two turbulence models illustrate that substantial development is still required for computing very complex flows before nozzle performance can be predicted accurately for all external flow conditions.

14. SUBJECT TERMS
Computational fluid dynamics; Navier-Stokes; Turbulence models; Two-equation k-ε; Transonic; Separated flow; Boundary layer; Afterbody; Nozzle; Convergent-divergent; Jet plume; Mixing; Drag; Skin friction

15. NUMBER OF PAGES
117

16. PRICE CODE
A06

17. SECURITY CLASSIFICATION OF REPORT	18. SECURITY CLASSIFICATION OF THIS PAGE	19. SECURITY CLASSIFICATION OF ABSTRACT	20. LIMITATION OF ABSTRACT
Unclassified	Unclassified	Unclassified	